Smart methodologies for efficient separation of liquid mixtures

by

Gibum Kwon

A dissertation submitted in partial fulfillment
of the requirements for the degree of
Doctor of Philosophy
(Materials Science and Engineering)
in the University of Michigan
2014

Doctoral Committee:

Assistant Professor Anish Tuteja, Chair
Associate Professor Jinsang Kim
Associate Professor Pramod Sangi Reddy
Professor Steven Skerlos

ACKNOWLEDGEMENTS

First of all, I would like to thank my research advisor, Professor Anish Tuteja. Not only has he been a great research mentor, but also a considerate educator during my graduate studies. He has encouraged me to develop innovative research ideas, while always guiding me in the right direction with timely leadership. Thanks to his guidance and enthusiasm, I have grown as a researcher and I really enjoyed working with him during my time at the University of Michigan. His thoroughness in research and personality made research life both rewarding and fun at the same time. I also would like to thank my thesis committee: Professor Jinsang Kim, Professor Pramod Reddy and Professor Steven Skerlos. They have suggested valuable research ideas and guided me to have a balanced perspective toward research. I was honored by the opportunity to conduct my graduate studies under their guidance.

I would also like to express my great thanks to my past and current fellow lab members. I would like to especially thank Dr. Arun Kota, who has started his new research career as an assistant professor at Colorado State University. I would not have been able to complete my graduate study without his support and help. I will never forget the variety of non-research topics we discussed. I also appreciate the support from Dr. Duck Hyun Lee. I have learned a great deal of nanofabrication skills in the cleanroom

from him. I wish him every success in his career. I would like to thank our group members: Sai Kobaku and Kevin Golovin for the discussions we had on a variety of research topics and for the pleasant journey to the conference, Dr. Raghuraman Karunakaran for helpful advice and encouragement, Dr. Chao Li for his advice on many topics, Mathew Boban for taking initiative as a safety manager in the lab and Ethan Post for being a successor to the separation projects and his hard work.

I would like to thank my friends and colleagues that shared many good times: Jonglo, Jaemyung, Jingu, Seongbaek, Kyungwoon, Dongwook, Dowon, Yoonseob, Myungkoo, Jongdoo, Jaehwan, Peter, Soonyeol, Seongjoo and many others.

I would not have been able to complete my graduate study without the support and love of my family. My parents, Hyukil Kwon and Imsun Park, and my sister, Yookyung Kwon, have always been there for me and believed in me. My niece, Seohyun, I always miss you.

Finally and most importantly, I would especially like to thank my fiancée, Hyo Jeong, for her never-ending love and support. I could not have made it this far without her. I will keep my promise, as I said before, one third of my entire life is set aside only for you. I love you more than you know.

TABLE OF CONTENTS

ACKNOWLEDGEMENTS..... ii
LIST OF FIGURES..... viii
LIST OF TABLES..... xvi
ABSTRACT..... xvii
CHAPTER 1. Introduction..... 1
1.1. Basic separation technologies..... 1
1.2. Separation of immiscible liquids..... 2
1.2.1. Oil-water mixtures..... 2
1.2.2. Conventional methodologies to separate oil-water mixtures..... 4
1.3. Fundamentals of interfacial science..... 5
1.3.1. Wettabilities of liquids..... 5
1.3.2. Effect of surface texture on the wettability..... 7
1.3.2.1. Two regimes of wettability..... 7
1.3.2.2. Critical role of re-entrant texture..... 9
1.3.3. Robustness of the composite interface..... 11
1.4. Membranes..... 12
1.4.1. Membrane-based separation..... 12
1.4.2. Membranes for oil-water separation..... 13
1.5. Design parameters of membranes..... 17
1.6. Separation of miscible liquids..... 19
1.7. References..... 22
CHAPTER 2. Hygro-responsive membranes for effective oil-water separation..... 29
2.1. Introduction..... 29
2.2. Experimental procedure..... 32
2.2.1. Materials..... 32
2.2.2. Substrate preparation..... 32
2.2.3. Oil-water emulsions..... 33
2.2.4. Characterization techniques..... 33
2.2.4.1. Contact angle measurements..... 33

2.2.4.2. Microscopy 34
2.2.4.3. Separation efficiency and droplet size distribution 34
2.3. Results and discussion 35
2.3.1. Wetting behavior of water and oil 35
2.3.2. Estimation of the solid surface energy 37
2.3.3. Surface reconfiguration 41
2.3.4. Time of wetting 43
2.3.5. Batch separation of oil-water mixtures 45
2.3.5.1. Separation of free oil and water 46
2.3.5.2. Separation of oil-in-water emulsions 47
2.3.5.3. Separation of water-in-oil emulsions 52
2.3.5.4. Separation of four-component mixtures 55
2.3.6. Estimation of hexadecane-water interfacial tension in the presence of surfactant 56
2.3.7. Breakthrough height 58
2.3.8. Continuous separation of oil-water emulsion 59
2.3.9. Location and concentration of surfactant after separation 62
2.3.10. Prediction of permeates fluxes during continuous separation of water-in-hexadecane emulsions 63
2.4. Conclusions 68
2.5. References 70
CHAPTER 3. Self-cleaning membranes for efficient oil-water separation 73
3.1. Introduction 73
3.2. Experimental procedure 75
3.2.1. Materials 75
3.2.2. Substrate preparation 76
3.2.2.1. Substrates with hygro-responsive surfaces 76
3.2.2.2. Conventional substrate with $\theta_{water} > \theta_{oil}$ 76
3.2.2.3. Conventional omniphilic substrate 76
3.2.3. Oil-water emulsion 76
3.2.4. Characterization techniques 77
3.2.4.1. Contact angle measurements 77
3.2.4.2. Microscopy 77
3.2.4.3. Separation efficiency and droplet size distributions 77
3.3. Results and discussion 78
3.3.1. Self-cleaning surfaces in air 78
3.3.2. Self-cleaning surfaces under oil 81
3.3.3. Recovery of oleophobicity 84
3.3.4. Separation of dodecane-in-water emulsions 88
3.4. Conclusions 92

3.5. References..... 94
CHAPTER 4. On-demand separation of oil-water mixtures..... 98
4.1. Introduction..... 98
4.2. Experimental Procedure..... 100
4.2.1. Materials..... 100
4.2.2. Non-textured substrate fabrication..... 101
4.2.3. Textured substrate fabrication..... 101
4.2.4. Oil-water emulsions..... 102
4.2.5. Characterization techniques..... 102
4.2.5.1. Contact angle and surface tension measurements..... 102
4.2.5.2. Thermogravimetric analysis and Karl Fischer analysis..... 103
4.2.5.3. Transmittance, dynamic light scattering and optical microscopy.... 103
4.3. Results and discussion..... 103
4.3.1. EWOD of water and oil on non-textured substrates..... 103
4.3.2. Transition from the Cassie-Baxter state to the Wenzel state..... 105
4.3.2.1. Derivation of the critical pressure $P_{critical}$ and the estimated values for $P_{critical}$..... 105
4.3.2.2. Electric field driven Cassie-Baxter to Wenzel transition..... 109
4.3.3. Estimation of hexadecane-water interfacial tension in the presence of surfactants..... 111
4.3.4. Batch separation of oil-water mixtures..... 112
4.3.4.1. Separation of free oil and water..... 112
4.3.4.2. Separation of oil-in-water emulsion..... 114
4.3.4.3. Separation of water-in-oil emulsion..... 119
4.3.5. Continuous separation of water-in-oil emulsions..... 123
4.3.6. Location and concentration of the surfactant after oil-water emulsion separation..... 125
4.4. Conclusion..... 127
4.5. References..... 129
CHAPTER 5. Energy-efficient separation of miscible components using hygro-responsive membranes..... 132
5.1. Introduction..... 132
5.2. Experimental Procedure..... 134
5.2.1. Materials..... 134
5.2.2. Hygro-responsive membrane preparation..... 134
5.2.3. Conventional hydrophobic and oleophilic membrane preparation..... 135
5.2.3.1. Membranes used for the separation of dye (or sulfur compounds) and for the separation of methanol..... 135
5.2.3.2. Membranes used for the separation of ethanol from ethanol-heptane azeotrope..... 135

5.2.4. Characterization techniques..... 135
5.2.4.1. Contact angle measurements..... 135
5.2.4.2. Microscopy..... 136
5.2.4.3. Refractive index measurements..... 136
5.2.4.4. UV-Vis spectroscopy..... 136
5.2.4.5. Separation efficiency..... 136
5.3. Results and discussion..... 137
5.3.1. Wetting behavior of polar and non-polar liquids..... 137
5.3.2. Time of wetting as a function of Hansen solubility parameters..... 138
5.3.3. Batch separations of liquid mixtures..... 140
5.3.3.1. Batch separation of methanol-hexadecane mixture..... 140
5.3.3.2. Batch separation of oil-soluble dye from dodecane..... 141
5.3.4. Continuous separation methodology..... 143
5.3.4.1. Separation of oil-soluble dye (Disperse Red 1) from dodecane..... 144
5.3.4.2. Separation of methanol from methyl oleate..... 146
5.3.4.3. Separation of ethanol-heptane azeotrope..... 150
5.3.4.4. Separation of sulfur compounds from dodecane..... 155
5.4. Conclusions..... 159
5.5. References..... 160
CHAPTER 6. Summary and Future Outlook..... 163
6.1. Thesis Summary..... 163
6.2. Future Outlook..... 165
6.3. References..... 168

LIST OF FIGURES

Figure

1.1. Surface classification based on water contact angles. (a) superhydrophilic, (b) hydrophilic, (c) hydrophobic and (d) superhydrophobic surfaces. Reproduced with permission from Kota *et al*.[43] © 2014 NPG Asia 5

1.2. A liquid droplet on a smooth solid surface. 6

1.3. Liquid droplets on textured surfaces. (a) A schematic illustration of a liquid droplet in the Cassie-Baxter state forming a composite solid-liquid-air interface. (b) A schematic illustration of a liquid droplet in the Wenzel state. In this state, the liquid droplet completely wets the surface, forming so-called 'fully-wetted' interface. Reproduced with permission from Kota *et al*.[43] © 2014 NPG Asia 7

1.4. The critical role of re-entrant texture. (a) A schematic illustration of a concave texture ($\psi > 90^{\circ}$) showing a liquid droplet with $\theta > 90^{\circ}$ in the Cassie-Baxter state. (b) A schematic illustration of a convex texture (re-entrant texture, $\psi < 90^{\circ}$) showing a liquid droplet with $\theta < 90°$ in the Cassie-Baxter state. Reproduced with permission from Kota *et al*.[43] © 2014 NPG Asia 10

2.1. Conventional hydrophilic and oleophilic membranes. (a) and (b) Neat x-PEGDA dip-coated mesh 100 and polyester fabric membranes, respectively (see section 2.2.). Both water (dyed blue) and rapeseed oil (dyed red) readily permeate through these membranes. (c) A mesh 100 coated with neat x-PEGDA sandwiched between two vertical glass tubes. Both water and rapeseed oil readily permeate through the membrane. 31

2.2. Wetting behavior of water and oil. (a) and (b) Droplets of water (dyed blue) and rapeseed oil (dyed red) on stainless steel mesh 100 (a) and polyester fabric (b). Both surfaces have been dip-coated with a 20 wt% fluorodecyl POSS + x-PEGDA blend. Insets, morphologies of the respective dip-coated mesh and fabric surfaces. Scale bars, 500 μm. 36

2.3. AFM phase images of surfaces coated with x-PEGDA (a), a 10 wt% fluorodecyl POSS + x-PEGDA blend (b) and a 20 wt% fluorodecyl POSS + x-PEGDA blend (c). The phase angle ranges are 0°-115° (a), 0°-25° (b) and 0°-21° (c). 36

2.4. Solid surface energy. The polar component (γ_{sv}^{p}), the dispersive component (γ_{sv}^{d}), and the total surface energy (γ_{sv})values for the as-prepared fluorodecyl POSS + x-PEGDA blends. 38

2.5. Surface reconfiguration. (a) and (b) Optical microscopy images of a surface coated with a 20 wt% fluorodecyl POSS + x-PEGDA blend in air (a) and under water (b). (c) In situ, underwater AFM phase image of a surface coated with a 20 wt% fluorodecyl POSS + x-PEGDA blend. The phase angle range is 0º-112º. 41

2.6. Reversible surface reconfiguration. (a) rapeseed oil (i) at a dry location, (ii) at a location previously wet by water, (iii) at a location that was wet by water and subsequently dried. (b) Contact angle of rapeseed oil as a function of water wetting-drying cycles. 42

2.7. Time of wetting (ToW). (a) and (b) ToW of water for spin-coated (a) and porous (b) substrates. Insets in (a) sho the time-dependent decrease in contact angle for a water droplet. Inset in (b) is a schematic illustrating the two scales of texture (bundles and individual fibers) for the fabric. The ToW predictions for mesh 100 and fabric membranes closely match experimental measurements, as shown in (b). 44

2.8. Batch separation of free oil and water. (a) Separation apparatus with water above the membrane. (b) Rapeseed oil is added above water. (c) Water permeates through the membrane whereas rapeseed oil is retained. Inset, water droplet on a surface spin-coated with a 20 wt% fluorodecyl POSS + x-PEGDA blend, rapeseed oil droplet on top of the water droplet, rapeseed oil droplet on the reconfigured surface. 46

2.9. Size distribution of hexadecane droplets in the hexadecane-in-water feed emulsion. (a) A representative optical microscopy image of 50:50 v:v hexadecane-in-water feed emulsion. Scale bar, 500 μm. (b) and (c) The number size distributions for the hexadecane-in-water feed emulsion from droplets > 1 μm and < 1 μm, respectively. 48

2.10. Batch separation of oil-in-water emulsion. (a) Separation apparatus with a 50:50 v:v hexadecane-in-water emulsion above the membrane. Inset, hexadecane droplet on a surface spin-coated with a 20 wt% fluorodecyl POSS + x-PEGDA blend, submerged in water containing dissolved SDS (1 mg/ml). (b) Water-rich permeate passes through the membrane whereas hexadecane-rich retentate is retained. Water is dyed blue and hexadecane is dyed red. Scale bar, 2 cm. 49

2.11. Size distribution of dispersed phase in permeates. (a) and (b) The number size distributions of the permeate from the separation of 50:50 v:v hexadecane-in-water emulsion using mesh 400 and mesh 500, respectively, obtained with optical image analysis. (c) and (d) The number size distributions of the permeate from the separation of 50:50 v:v hexadecane-in-water emulsion using mesh 400 and mesh 500, respectively, obtained with DLS. 50

2.12. TGA, Transmittance and density measurements. (a) TGA data for the permeate and retentate. HD, hexadecane. (b) Transmittance of 50:50 v:v hexadecane-in-water feed emulsion and the permeate. (c) Density of hexadecane-in-water mixtures as a function of hexadecane (HD) composition. 52

2.13. Size distribution of water droplets in the water-in-hexadecane feed emulsion. (a) A representative optical microscopy image of 30:70 v:v water-in-hexadecane feed emulsion. Scale bar, 200 μm. (b) and (c) The number size distributions for the water-in-hexadecane feed emulsion fro droplets > 1 μm and < 1 μm, respectively. 53

2.14. Batch separation of water-in-oil emulsion. (a) Apparatus with a 30:70 v:v water-in-hexadecane emulsion above the membrane. Inset, hexadecane droplet on a surface spin-coated with a 20 wt% fluorodecyl POSS + x-PEGDA blend, submerged in water containing dissolved PS80 (1 mg/ml). (b) Water-rich permeate passes through the membrane whereas hexadecane-rich retentate is retained. Water is dyed blue and hexadecane is dyed red. Scale bar, 2 cm. 54

2.15. TGA and transmittance measurements. (a) TGA data for the permeate and retentate. HD, hexadecane. (b) Transmittance of 30:70 v:v water-in-hexadecane feed emulsion and the permeate. 55

2.16. Batch separation of four component mixtures. (a) Apparatus with four-component mixture above the membrane. Inset, larger quantity of feed in a glass vial, depicting the presence of different phases. (b) Water-rich permeate passes through the membrane whereas hexadecane-rich retentate is retained. Water is dyed blue and hexadecane is dyed red. Scale bar, 2cm. (c) TGA data for the permeate and retentate. HD, hexadecane. 55

2.17. Continuous separation of water-in-oil emulsion. (a) A scaled-up apparatus used for the continuous separation of 30:70 v:v water-in-hexadecane emulsions stabilized by PS80. During continuous separation, water-rich permeate continuously passes through the superhydrophilic and oleophobic membrane at the bottom, whereas hexadecane-rich permeate continuously passes through the hydrophobic and oleophilic membrane on the side-wall. Water is dyed blue and hexadecane is dyed red. Scale bar, 5 cm. (b) TGA

data for both the permeates. HD, hexadecane. 60
2.18. Volume size distribution. Volume size distribution of water droplets for the 30:70 v:v water-in-hexadecane feed emulsion. The dashed region represents droplets below 20 μm (emulsified droplets). 61
2.19. Location and concentration of surfactant after emulsion separation. (a) and (b) Advancing and receding contact angles of water as a function of SDS concentration and PS80 concentration, respectively. (c) Advancing and receding contact angles of hexadecane as a function of PS80 concentration.. 62
2.20. Measured fluxes for both the permeates as a function of time. 64
3.1. Self-cleaning surfaces. (a) and (b) Droplets of water (dyed blue) and dodecane (dyed red) on a cellulose film (a) and cellulose-based filter paper with pore size ≈ 200 nm (b). Both surfaces have been treated with Heptadecafluoro-1,1,2,2-tetrahydrodecyl triethoxy silane. (c) and (d) Water displaces dodecane droplet from the surface. The displaced dodecane droplet floats on top of the water. 78
3.2. Surfaces with $\theta_{water} > \theta_{oil}$. (a) and (b) Droplets of water (dyed blue) and dodecane (dyed red) on a cellulose film (a) and cellulose-based filter paper with pore size ≈ 200 nm (b). Both surfaces have been coated with PMMA. (c) and (d) Water spreads on top of dodecane, preventing the surface from being cleaned. 80
3.3. Omniphilic surfaces. (a) and (b) Droplets of water (dyed blue) and dodecane (dyed red) on a cellulose film (a) and cellulose-based filter paper with pore size ≈ 200 nm (b). Both surfaces have been treated with 2-[methoxy (polyethyleneoxy)-propyl] trimethoxy silane. (c) and (d) Water spreads on top of dodecane although the density of water is higher than that of dodecane. 81
3.4. SEM images of cellulose-based filter papers. (a), (b) and (c) SEM images of filter papers with nominal pore sizes of 450 nm, 200 nm and 10 nm, respectively, before silanization. (d), (e) and (f) SEM images of filter papers with nominal pore sizes of 450 nm, 200 nm and 10 nm, respectively, after surface treatment. 83
3.5. Self-cleaning surface under oil. A series of snapshots showing a droplet of water on a cellulose-based filter paper with pore size 200 nm, submerged in dodecane. The water droplet displaces dodecane and penetrate into the membrane as a function of time. 84
3.6. Recovery of oleophobicity. (a) Separation apparatus with water and dodecane above the membrane. The membrane sandwiched between the two glass tube is prefouled by dodecane. Inset, the membrane saturated with dodecane. Water is dyed blue and dodecane is dyed red. (b) The water-rich permeate passes through the membrane while the dodecane-rich retentate is

retained above the membrane. (c) DSC data for the water-rich permeate. DSC data for as-obtained dodecane and water are also shown for comparison. 86
3.7. Recovery of oleophobicity. (a) Separation apparatus with a 20:80 v:v dodecane-in-water emulsion above the membrane. The membrane sandwiched between the two glass tube is prefouled by dodecane. Water is dyed blue and dodecane is dyed red. (b) The water-rich permeate passes through the membrane while the dodecane-rich retentate is retained above the membrane. (c) DSC data for the water-rich permeate. DSC data for as-obtained dodecane and water are also shown for comparison. 88
3.8. Size distributions of dodecane droplets (a) The number size distribution for the dodecane-in-water feed emulsion. (b), (c) and (d) The number size distributions for the permeates obtained from the separation of dodecane-in-water feed emulsion using filter papers with pore size = 450 nm, 200nm and 10 nm, respectively. 89
3.9. Measured fluxes for the permeates obtained from separations of dodecane-in-water emulsion using a membrane with different pore size. 90
4.1. A schematic illustration of Electrowetting on a dielectric (EWOD) configuration. 99
4.2. EWOD behavior of water and oil. (a) Macroscopic contact angles for water and hexadecane (HD) as a function of applied voltage on the non-texutred substrate. (b) and (c) The macroscopic contact angle for hexadecane remain unchanged with increasing voltage. (d) and (e) The macroscopic contact angle for water decreases with increasing voltage. 104
4.3. A schematic illustrating the pressure-induced sagging of the liquid-air interface. 106
4.4. A schematic showing the pressure-induced sagging of the liquid-air interface on a stack of three membranes with cylindrical texture. 110
4.5. Batch separation of free oil and water. (a) An apparatus with a liquid column of free oil (dyed red) and water (dyed blue) above the membrane before applying an electric field. The inset shows a schematic of the membrane module. (b) Water permeates through while hexadecane is retained when a voltage V ~ 2.0 kV is applied. 113
4.6. Size distribution of hexadecane droplets in the feed hexadecane-in-water emulsion. (a) A representative optical microscopy image of the feed hexadecane-in-water emulsion. (b) and (c) The number size distributions for the hexadecane-in-water feed emulsion for droplets > 1 μm and < 1 μm, respectively. 114
4.7. EWOD behavior of water and oil in the presence of PS80. (a) Macroscopic contact angles for water and hexadecane (HD) in the presence of PS80 as a

function of applied voltage on the non-textured substrate. (b) Competitive wetting of water and hexadecane containing PS80. Insets (i) and (ii) show the macroscopic contact angle for hexadecane before and after applying voltage, respectively. (c) A schematic showing the competitive wetting of water and oil. 115

4.8. Separation of oil-in-water emulsion. (a) An apparatus with a liquid column of hexadecane-in-water emulsion above the membrane before applying an electric field. (b) Water-rich permeate passes through while hexadecane-rich retentate is retained when a voltage V ~ 1.1 kV is applied. (c) Separation of the hexadecane-in-water emulsion using a scaled-up apparatus. Water is dyed blue and hexadecane is dyed red. 117

4.9. TGA and transmittance data. (a) TGA data for the permeate and the retentate obtained from the batch separation of hexadecane-in-water emulsion. (b) Transmittance data for hexadecane-in-water feed emulsion and the permeate after separation. 118

4.10. Number size distributions of the permeate. (a) and (b) The number size distributions of the permeate from the separation of the hexadecane-in-water emulsion obtained with optical image analysis and DLS, respectively. 119

4.11. Size distribution of water droplets in the feed water-in-hexadecane emulsion. (a) A representative optical microscopy image of the feed water-in-hexadecane emulsion. (b) and (c) The number size distributions for the feed water-in-hexadecane emulsion for droplets > 1 μm and < 1 μm, respectively. 120

4.12. Separation of water-in-oil emulsion. (a) An apparatus with a liquid column of water-in-hexadecane emulsion above the membrane before applying an electric field. (b) The water-in-hexadecane emulsion is demulsified into the water-rich and the hexadecane-rich phases upon applying an electric field. (c) After the onset of demulsification, water-rich permeate passes through while hexadecane-rich retentate is retained when a voltage V ~ 2.0 kV is applied. Water is dyed blue and hexadecane is dyed red. 121

4.13. TGA and transmittance data. (a) TGA data for the permeate and the retentate obtained from the batch separation of water-in-hexadecane emulsion. (b) Transmittance data for water-in-hexadecane feed emulsion and the permeate after separation. 122

4.14. Continuous separation of water-in-hexadecane emulsion. (a) An apparatus used for continuous separation of water-in-hexadecane emulsion. Water-rich permeate passes through the membrane module at the bottom, while hexadecane-rich permeate passes through the hydrophobic and oleophilic membrane on the side-wall. (b) TGA data for the water-rich and the hexadecane-rich permeates. Water is dyed blue and hexadecane is dyed red. 124

4.15. Volume size distribution of water droplets for the water-in-hexadecane feed emulsion. The dashed region represents droplets below 20 μm (emulsified droplets). 125
4.16. Location and concentration of surfactant after emulsion separation. (a) and (b) Advancing and receding contact angles for water and hexadecane, respectively, as a function of PS80 concentration. 127
5.1. Wetting behavior of polar and non-polar liquids. (a) and (b) Droplets of ethanol (dyed blue), DMF (dyed green), hexadecane (dyed red) and dodecane (dyed yellow) on the hygro-responsive membranes fabricated using a cellulose-based filter paper (nominal pore size = 2.5 μm) and a wipe, respectively. Insets, morphologies of the respective filter paper and wipe surfaces. 138
5.2. Time of wetting. Time of wetting for a series of alcohols on the hygro-responsive membranes shown figure 5.1a. Insets show sequential wetting of four alcohol droplets in the order of decreasing the sum of polar and hydrogen bonding components of Hansen solubility parameters. 139
5.3. Batch separation of methanol and hexadecane mixture. (a) A batch separation apparatus with 50:50 v:v methanol-hexadecane mixture above the membrane. (b) Methanol-rich permeate passes through the membrane while hexadecane-rich phase is retained. Methanol is dyed blue and hexadecane is dyed red. (c) TGA data for the methanol-rich permeate and hexadecane-rich retentate. TGA data for as obtained methanol and hexadecane are also shown for comparison. Inset shows methanol-rich permeate contains ≈ 2 wt% hexadecane. 140
5.4. Size distribution of dodecane droplets in the dodecane-in-DMF emulsion. (a) A representative optical microscopy image of 50:50 v:v dodecane-in-DMF emulsion. (b) and (c) The number size distributions of the dodecane-in-DMF feed emulsion for droplets > 1 μm and < 1 μm, respectively. 141
5.5. Batch separation of the dye (Disperse Red 1). (a) A batch separation apparatus with 50:50 v:v dodecane-in-DMF emulsion above the membrane. (b) Dye-enriched DMF phase permeates through the membrane while dye-depleted dodecane phase is retained. 143
5.6. Continuous separation of dye (Disperse Red 1). (a) An apparatus used for continuous separation of dye using SDS-stabilized dodecane-in-DMF emulsion. (b) UV-Vis absorbance data for the dodecane phases obtained from continuous separations with and without emulsification, using a 90:10 feed:extractant volumetric flow rates. (c) The % dye unextracted from dodecane after separations using different feed:extractant volumetric flow rates. Inset shows the dodecane phase after separations. 145
5.7. Continuous separation of methanol from methyl oleate. (a) Refractive index

data for methyl oleate as a function of methanol concentration (0 – 10 vol%). (b) Refractive index data for water as a function of methanol concentration (0 – 50 vol%). Insets show calibration curves of refractive index for methyl oleate and water as a function of methanol concentrations (0 – 100 vol%). (c) The % methanol unextracted from methyl oleate as a function of feed:extractant volumetric flow rates. 147

5.8. Continuous separation of ethanol from the ethanol-heptane azeotrope. (a) Refractive index data for heptane as a function of ethanol concentration (0 – 16 vol%). Inset shows calibration curves of refractive index for heptane as a function of ethanol concentration (0 – 100 vol%). (b) Refractive index data for water as a function of ethanol concentration (0 – 100 vol%). (c) The % ethanol unextracted from ethanol-heptane azeotrope as a function of feed:extractant volumetric flow rates. 151

5.9. Continuous separation of benzothiophene. (a) UV-Vis absorbance data for the benzothiophene-depleted dodecane phases obtained from continuous separations with and without emulsification, using a 50:50 feed:extractant volumetric flow rates. UV-Vis absorbance data for dodecane with different benzothiophene concentration are also shown for comparison. (b) A plot of calculated area under the UV-Vis absorbance curves as a function of benzothiophene concentration. (c) The % benzothiophene unextracted from dodecane as a function of feed:extractant volumetric flow rates. 156

LIST OF TABLES

Table

2.1. Contact angles and surface energies for the materials used. 40

2.2. Measured fluxes for the water-rich permeate and the hexadecane-rich permeate during the continuous separation of 30:70 v:v water-in-hexadecane emulsions as a function of time. 68

3.1. Measured fluxes for the permeates obtained from separations of 20:80 v:v dodecane-in-water emulsion using a membrane with different pore size. 92

4.1. Calculated values of $P_{critical}$ for water and hexadecane on the dip-coated nylon membranes (R = 20.3 μm, 2D = 28 μm), with and without surfactants. 108

5.1. Measured refractive indices for the methanol-depleted dodecane phases and the methanol-enriched aqueous phases during continuous separations using different feed:extractant volumetric flow rates. 150

5.2 Measured refractive indices for the ethanol-depleted heptane phase and the ethanol-enriched aqueous phase during continuous separations using different feed:extractant volumetric flow rates. 154

5.3. Calculated the area under the UV-Vis absorbance curves for benzothiphene-depleted dodecane phases obtained from continuous separations with and without emulsification using different feed:extractant volumetric flow rates. .. 158

5.4. The concentrations of t-butyl thiol in the dodecane phases obtained from continuous separations with and without emulsification using different feed:extractant volumetric flow rates. 158

ABSTRACT

There is a critical need for new energy-efficient solutions for separating liquid mixtures. Among the variety of current separation technologies, membrane-based operations are attractive because they are relatively energy-efficient, and are applicable to a wide range of industrial effluents. However, traditional membrane-based technologies have disadvantages of fouling or poor separation efficiency. This research explores the systematic design of membranes, as well as, the development of smart methodologies that enable separation of a wide variety of both immiscible and miscible liquid mixtures.

The first part of my thesis describes membranes that can separate oil-water mixtures, solely under gravity. Guided by design parameters, we have developed novel membranes with hygro-responsive surfaces, which are both superhydrophilic and superoleophobic. These membranes are oleophobic both in air and when submerged under water. Utilizing these membranes, we have developed capillary force-based separation (CFS) methodology that can separate a range of different oil-water mixtures, with > 99% efficiency. We have also engineered an apparatus that uses two CFS-based operations in parallel, to achieve continuous, solely gravity-driven separation of oil-water emulsions, with a separation efficiency > 99.9%.

In the second part, we describe that controlled silanization of cellulose-based filter papers can create a robust and homogeneous, hygro-responsive, coating on the filter surface. This hygro-responsive coating can be applied to filters having pore sizes as small as 10 nm. The developed membranes were found to have unique self-cleaning abilities as water can displace oil from the membrane surface. This allows the membranes to be extremely fouling resistant. We have also demonstrated that our membranes can separate surfactant-stabilized oil-in-water emulsions with oil droplets diameter as small as 10 nm.

The third part of my thesis investigates a separation methodology where the separation is triggered on-demand. In the CFS methodology utilizing hygro-responsive membranes described previously, the separation takes place instantaneously as soon as water contacts the membrane. By contrast, we have also developed a new separation methodology where the separation can be triggered by applying an electric field. For an effective on-demand separation of oil-water mixtures, both water and oil must be retained above the membrane before the application of the electric field. Such membranes have been fabricated based on the understanding of the roles of surface texture along with surface chemistry. We have also successfully estimated the voltage required to trigger the separation using a breakthrough pressure model that incorporates the Maxwell stress and the hydrostatic pressure. Finally, we have engineered a continuous oil-water emulsion separation apparatus that removes > 99% of the emulsified drops.

In the final part of this thesis, a new methodology to separate miscible components from a liquid mixture is discussed. In order to separate miscible components including azeotropes, we have developed a new energy-efficient methodology that combines liquid-liquid extraction using surfactant-stabilized emulsions, and solely

gravity-driven separation of these emulsions into a single unit operation. We have demonstrated that our methodology is useful for a wide range of separations, including the separation of miscible dyes, alcohols and sulfur compounds from oils, as well as, separation of alcohol-hydrocarbon azeotropes.

CHAPTER 1

Introduction

1.1. Basic separation technologies

Separation operations span across numerous manufacturing industries and account for about a quarter of all in-plant energy consumptions in the United States[1]. The most common liquid-liquid separation technique is distillation, which involves the transfer of components between vapor and liquid phases[2]. Distillation utilizes the differences in vapor pressure or boiling points among the different mixture components. Similarly, crystallization is a technique which exploits the differences in melting points[3]. Another common separation operation is liquid-liquid extraction, where the feed mixture is liquid and a second, immiscible liquid phase is added to extract out a component of the feed mixture[4]. Absorption is also widely used for separation if the feed is vapor and a liquid of low volatility is added[3]. In both cases, components in the feed mixture have significantly different solubilities within the added phase. Membrane-based separation operation which utilizes the differences in permeabilities of components is a relatively new technique and of growing importance[5]. Finally, external fields including centrifugal,

thermal, electrical have also been applied in specialized cases to separate mixtures by exploiting differences in density, diffusivity and electric charge[3].

For all the different techniques described above, the driving force for separation is governed by a change in the thermodynamic equilibrium[3]. For example, distillation and crystallization are thermally driven processes that utilize heat of vaporization or fusion as their driving forces. On the other hand, liquid-liquid extraction and membrane-based separations are accomplished based on the differences in chemical make-up and physical properties of the components to be separated. Their driving forces are typically lower (by one or more orders of magnitude) than those for thermally driven processes[1]. Innovations to improve separation technologies are critical for the productivity of different industries, in particular for achieving their energy and waste reduction goals. The greatest opportunities for energy savings in separation technologies lie in replacing energy-intensive operations (e.g., distillation) with energy-efficient alternatives (e.g., liquid-liquid extraction and membrane-based separations). Overall there is a great need and a significant opportunity to develop new energy-efficient separation methodologies.

1.2. Separation of immiscible liquids

1.2.1. Oil-water mixtures

Separation of immiscible liquid mixtures is crucial not only for scientific research but also for numerous environmental, economic and health requirements[6-11]. One of the most ubiquitous, immiscible, liquid mixtures is oil and water. A large amount of oily wastewater is produced everyday during industrial processing, such as petrochemical, food, textile, leather and metal finishing[6]. The effect of this wastewater on the

environment can be severe, unless it is adequately treated before discharge, as can be observed from the many recent oil-spill disasters[12-14]. In addition, shortage of freshwater has become a severe problem in the world, especially in certain underdeveloped regions[11,15,16]. Purification of oily wastewater can enhance the amount of water available for use[17]. Furthermore, expulsion of water from fuel oil is of great concern in petroleum and automobile industries because even a small amount of water in the fuel oil may damage engines, threatening the safety of the automobile[18].

Mixtures of oil and water from a wide range of industries are classified[19], in terms the diameter (d) of the dispersed phase, as free oil and water if $d > 150$ μm, a dispersion if 20 μm $\leq d \leq$ 150 μm, or an emulsion if $d < 20$ μm. Stable oil-water emulsions are typically prepared in the presence of a surfactant (or dispersant). The functions of surfactants are to facilitate emulsification and prevent flocculation and coalescence by forming a thin film around the dispersed droplets. Surfactant-stabilized oil-water emulsions can exist in several forms. If the oil is dispersed in water, the emulsion is termed an oil-in-water (O/W) emulsion. On the other hand, if the water is dispersed in oil, the emulsion is termed a water-in-oil (W/O) emulsion. In contrast to simple emulsions, multiple emulsions such as oil-in-water-in-oil (O/W/O) or water-in-oil-in-water (W/O/W) emulsions can also exist[20,21]. The type of emulsion which tends to form is governed by the balance between the hydrophilic and lipophilic (or oleophilic) properties of the surfactants. The amphiphilic nature of surfactants can be expressed in terms of HLB (hydrophilic-lipophilic balance) values[22]. In addition, depending on the concentration of the dispersed phase and / or the temperature, an oil-in-water emulsion may invert to a water-in-oil emulsion or vice-versa[23].

1.2.2. Conventional methodologies to separate oil-water mixtures

Various methodologies including gravity separation, air flotation, oil-absorbing materials, coagulation and flocculation have been used to separate oil-water mixtures[7,19,24,25]. Conventional gravity separator and skimming is effective in removing free oil. However, it is unsuitable to separate smaller oil droplets and emulsions[19]. Although air flotation method increases the buoyancy of smaller oil droplets and enhances separation, it is typically followed by demulsification process with chemicals and/or heat[25,26]. In addition, porous materials are widely used to absorb oils from water in case of oil-spills in the ocean. However, these materials not only absorb oil, but also water, due to lack of selectivity, resulting in low efficiency[27,28]. Electrocoagulation or adding chemicals can be effective for demulsifying emulsions, but these methods usually involve significant energy consumption and secondary pollution[29,30]. Efficient and broadly applicable methodologies to separate various oil-water mixtures, especially those stabilized by surfactants remain highly desired.

Recently, membrane-based technologies have become very attractive for oil-water separation because they are relatively energy-efficient, cost-effective, and are applicable across a wide range of industrial effluents[19,31]. In spite of these advantages, the broad application of membrane-based technologies in various fields remains limited. The major problems are membrane fouling and degradation during use due to surfactant adsorption or plugging of membrane pores by oil droplets, resulting in a decline of the flux[32,33]. Thus, there is still a critical need to develop novel materials and methodologies with high selectivity, high separation capacity, stability, and fouling-resistant performance.

1.3. Fundamentals of interfacial science

1.3.1. Wettabilities of liquids

When a droplet of liquid contacts a solid surface, either wetting or non-wetting phenomena is observed. Wettability of a liquid droplet depends on the relation of the interfacial energies between the solid, liquid, and air. The simplest measure of wetting on a solid surface is the contact angles between a liquid droplet and a solid surface. Based on previous literature[34-36], the whole range of wettability of the solid surface can be classified into four regimes using water contact angles (see figure 1.1): superhydrophobic, hydrophobic, hydrophilic and superhydrophilic if water contact angles > 150°, > 90°, < 90° and 0°. In this case, the medium surrounding the water droplet may be either oil or air. Similarly, surfaces with oil contact angles > 150°, > 90°, < 90° and 0° are considered superoleophobic, oleophobic, oleophilic and superoleophilic respectively. In this case, the medium surrounding oil may be either water or air. Typically superhydrophobic or superoleophobic surfaces are referred as super-repellent surfaces.

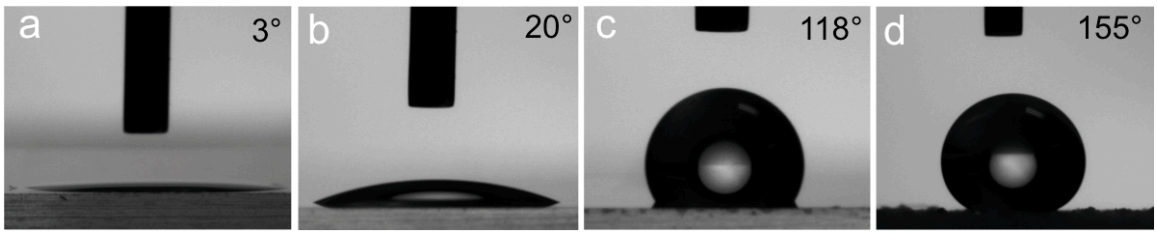

Figure 1.1 Surface classification based on water contact angles. (a) superhydrophilic, (b) hydrophilic, (c) hydrophobic and (d) superhydrophobic surfaces. Reproduced with permission from Kota *et al*.[36] © 2014 NPG Asia Materials.

Figure 1.2 shows an ideal contact between a liquid droplet and a smooth solid surface. If a liquid droplet is small enough to neglect the effect from gravity, the free energy of the whole system becomes minimum when interfacial energies balance to a minimum. This is obtained when a liquid droplet makes an equilibrium contact angle θ with the solid surface and air. The equilibrium contact angle or Young's contact angle θ is described by Young's equation as[37]:

(Equation 1.1) $\gamma_{lv}\cos\theta = \gamma_{sv} - \gamma_{sl}$

where γ refers to the interfacial tension and *s*, *v* and *l* refers to solid, vapor (or air) and liquid phase respectively. The Young's relation implies that as the solid-air interfacial energy decreases relative to the solid-liquid interfacial energy, the contact angle for a given liquid increases[38]. Although the Young's contact angle provides the easiest way to quantify the degree of wetting, it is difficult to obtain experimentally. This is because the solid surface must be ideally smooth and flat in order to measure the Young's contact angle. Instead, experimentally measurable contact angles are often reported. When a liquid-air interface is advancing the contact angle takes on a large value than when the interface is receding. These contact angles are referred to as the advancing contact angles θ_{adv} and receding contact angles θ_{rec}. The difference between advancing and receding contact angles is known as contact angle hysteresis.

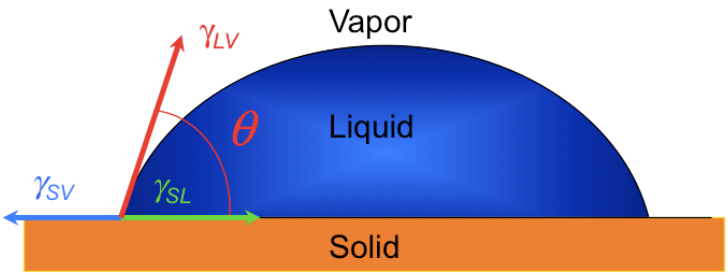

Figure 1.2 A liquid droplet on a smooth solid surface.

1.3.2. Effect of surface texture on the wettability

1.3.2.1. Two regimes of wettability

When a droplet of liquid is placed on a textured (rough) surface, the apparent contact angle θ^* on the surface can be significantly different from the Young's contact angle. The addition of a liquid droplet on a textured surface may lead to either the Cassie-Baxter state[39] forming a composite solid-liquid-air interface or the 'fully-wetted' Wenzel state[40]. In the Cassie-Baxter state (see Figure 1.3a), the liquid droplet attains its equilibrium contact angle locally with the surface texture.

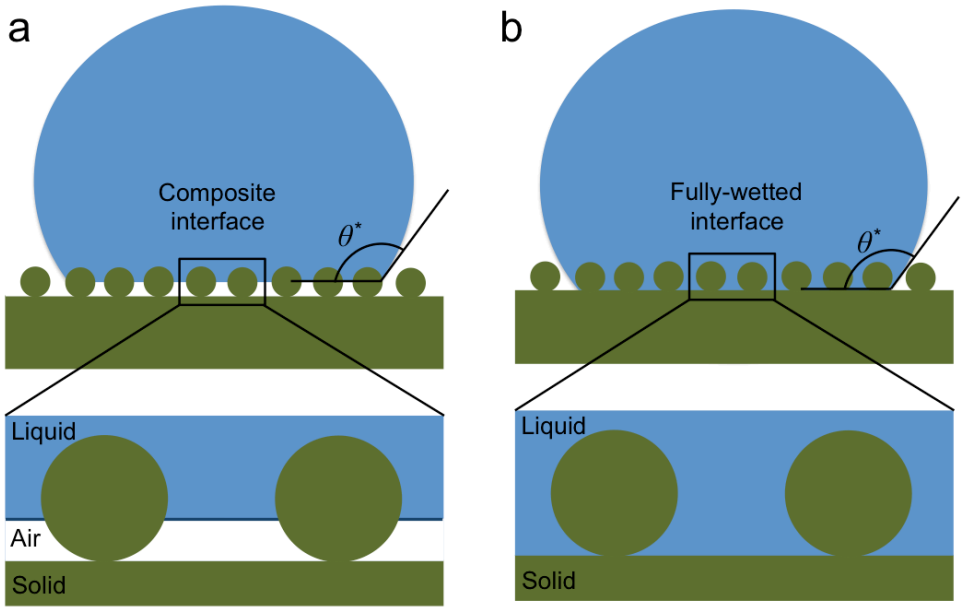

Figure 1.3 Liquid droplets on textured surfaces. (a) A schematic illustration of a liquid droplet in the Cassie-Baxter state forming a composite solid-liquid-air interface. (b) A schematic illustration of a liquid droplet in the Wenzel state. In this state, the liquid droplet completely wets the surface, forming so-called 'fully-wetted' interface. Reproduced with permission from Kota *et al*.[36] © 2014 NPG Asia Materials.

However, it does not completely penetrate all of surface asperities. Consequently, pockets of air remain trapped underneath the liquid droplet and thus a composite solid-liquid-air

interface forms. Cassie and Baxter[39] suggested that the overall free energy becomes minimum when the apparent contact angle reaches a value θ^*, which is a weighted average between the values of the equilibrium contact angle of the liquid on the solid (i.e., θ) and on the air pocket (i.e., π). The apparent contact angle in this state is often calculated using the Cassie-Baxter relation, given as:

(Equation 1.2) $\cos\theta^* = f_s \cos\theta + f_v \cos\pi = f_s \cos\theta - f_v$

where f_s and f_v are the fractions of solid and air in contact with the liquid per unit projected area of the composite interface. The Cassie-Baxter relation can be simplified[41,42] using r_ϕ and ϕ_s, where r_ϕ is the roughness of the wetted area, which is ratio of the actual wetted area to the occluded area, and ϕ_s is the fraction of the projected area wet by the liquid. If $f_s = r_\phi \phi_s$ and $f_v = 1 - \phi_s$, then equation 1.2 can be rewritten as:

(Equation 1.3) $\cos\theta^* = r_\phi \phi_s \cos\theta + (1 - \phi_s)\cos\pi = r_\phi \phi_s \cos\theta - (1 - \phi_s)$

On the other hand, if the contacting liquid droplet cannot make an equilibrium contact angle locally with surface texture, the liquid droplet completely penetrates into the bottom of pores forming so-called 'fully-wetted' interface (see Figure 1.3b). In this state, the overall free energy reaches its minimum value when the apparent contact angle of the liquid droplet becomes θ^* given by the Wenzel relation[40] shown as:

(Equation 1.4) $\cos\theta^* = r\cos\theta$

where r is the surface roughness defined as the ratio of the actual surface area to the projected surface area. The Wenzel relation is a special case of the Cassie-Baxter relation[41]. When $\phi_s = 1$ or $f_v = 1$ (fully wetted surface), $r_\phi = r$ the Cassie-Baxter relation reduces to the Wenzel relation.

Both the Cassie-Baxter and the Wenzel relations predict the apparent contact angles on a textured surface utilizing free energy analysis. Also they provide a correlation between the apparent contact angle and equilibrium contact angle. Based on their relations, very high apparent contact angles can be achieved either in the Wenzel state if $\theta > 90^{\circ}$ and $r >> 1$ or in the Cassie-Baxter state if $\phi_s << 1$. However, the contact angle hysteresis of the two states is markedly different. Typically the contact angle hysteresis in the Wenzel state is larger than that in the Cassie-Baxter state. This is because fully-wetted solid-liquid interface is heavily pinned on numerous asperities present on the textured surface[43]. Liquid droplets, thus, cannot readily recede or roll-off of the textured surface. On the other hand, a composite interface in the Cassie-Baxter state typically leads to low contact angle hysteresis or low roll-off angle and high apparent contact angles when total contact area between the liquid droplet and the solid surface is very small[43,44]. Thus the development of composite interfaces is essential in engineering superhydrophobic or superoleophobic surfaces[34,45,46]. Based on this understanding, there have been a large number of non-wetting surfaces synthesized and utilized in various applications such as self-cleaning[47], anti-fouling[48], spill-resistant protective wear[49] and drag reduction[50].

1.3.2.2. Critical role of re-entrant texture

Although the development of the Cassie-Baxter state is desirable in engineering super-repellent surfaces, not all types of surface textures can lead to the formation of a composite interface, especially with oils. For example, consider two different types of texture shown in Figures 1.4a and 1.4b, both having the same solid surface energy. While

the texture shown in Figure 1.4a is concave (texture angle $\psi > 90^{\circ}$) and the texture shown in Figure 1.4b is convex ($\psi < 90^{\circ}$) facing upwards.

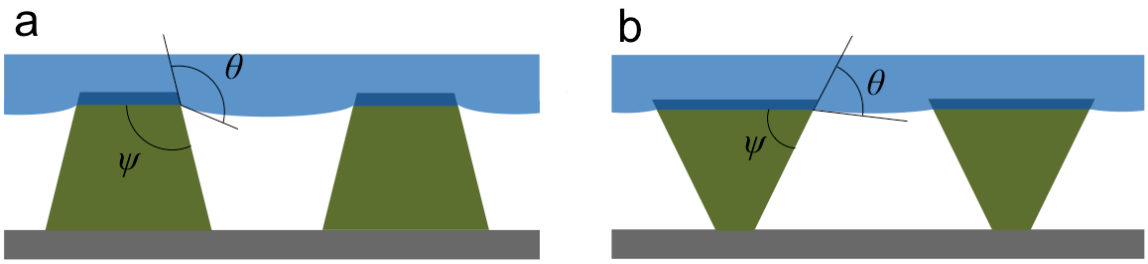

Figure 1.4 The critical role of re-entrant texture. (a) A schematic illustration of a concave texture ($\psi > 90^{\circ}$) showing a liquid droplet with $\theta > 90^{\circ}$ in the Cassie-Baxter state. (b) A schematic illustration of a convex texture (re-entrant texture, $\psi < 90^{\circ}$) showing a liquid droplet with $\theta < 90°$ in the Cassie-Baxter state. Reproduced with permission from Kota *et al.*[36] © 2014 NPG Asia Materials.

Previous literature[41,42,46,51] proved that formation of the Cassie-Baxter state is only possible when $\theta \geq \psi$. This is because if $\theta < \psi$, the net traction of the surface tension points downward due to capillary forces, the liquid instantly proceeds to fully-wet the entire texture. The texture shown in Figure 1.4a can still enable formation of a composite interface when the Young's contact angle $\theta \geq \psi$. In contrast, if the Young's contact angle $\theta < 90°$, which is unavoidable with low surface tension liquids such as oils, surface textures shown in Figure 1.4a cannot maintain the composite interface. However, for the same low surface tension liquid with $\theta < 90°$, it is still possible to support the composite interface as long as ψ is even smaller than θ. Such convex geometry with $\psi < 90^{\circ}$ is called re-entrant texture, i.e., the texture bends back on itself [34,46,52,53] (see Figure 1.4b). On the re-entrant textured surface, the net traction of the surface tension of liquid points upward even for liquids possessing $\theta < 90°$. This allows the possibility of the formation

of a composite interface against low surface tension liquids. However, re-entrant texture that enables the condition $\theta \geq \psi$ for low surface tension liquids, is a necessary, but not a sufficient condition for the formation of the Cassie–Baxter state[41,42,51].

1.3.3. Robustness of the composite interface

In real cases, numerous sources including gravity, mechanical vibration, Laplace pressure, and Maxwell pressure creates a significant pressure differential across the liquid-air interface. This pressure differential may cause disruption of the liquid-air interface to proceed to the bottom of the surface texture resulting in the transition from the Cassie-Baxter state to the fully-wetted Wenzel state[54,55]. This transition is typically irreversible. Hence it is imperative to estimate breakthrough pressure (i.e., $P_{breakthrough}$, the maximum pressure differential across the composite interface that can force a transition from the Cassie-Baxter state to the Wenzel state) for the composite interface in designing liquid-repellent surfaces. In order to parameterize the $P_{breakthrough}$ for a known surface texture, previous works[45,46] have discussed the robustness factor A^*. This is obtained by scaling the breakthrough pressure to the reference pressure defined as $P_{ref} = 2\gamma_{lv} / l_{cap}$, where $l_{cap} = \sqrt{\gamma_{lv} / \rho g}$ is the capillary length of a liquid, ρ is the liquid density and g is the acceleration due to gravity. P_{ref} is close to the minimum possible pressure differential across a millimeter-sized liquid droplet or a puddle. Consequently, if the ratio of $P_{breakthrough} / P_{ref}$ is smaller than unity for a given contacting liquid, the surface cannot support a composite interface. On the other hand, a high ratio of $P_{breakthrough} / P_{ref}$ implies the formation of a robust composite interface that can support high breakthrough pressure. For surfaces possessing a cylindrical texture, the robustness factor A^* is given as[45,46]:

(Equation 1.5) $$A^* = \frac{P_{\text{breakthrough}}}{P_{\text{ref}}} = \frac{Rl_{\text{cap}}}{D^2} \frac{1-\cos(\theta)}{1+2(R/D)\sin(\theta)}$$

1.4. Membranes

1.4.1. Membrane-based separation

Membrane-based methodologies physically separate a feed mixture into its components by allowing one phase to permeate through the membrane (the permeate) while retaining the other component (the retentate)[1]. Since the separation is performed at ambient temperature without chemically altering the components, membrane-based separation operations consume less energy than other separation methods. The transportation of components through the membrane is accomplished due to driving forces acting on the individual components in the feed. The driving force can either be a gradient in pressure, concentration, temperature or electrical potential[56,57]. Pressure-driven membrane operations including microfiltration, ultrafiltration and reverse osmosis are commonly used in the separation of oil-water mixtures[58]. The difference between microfiltration, ultrafiltration, and reverse osmosis is the membrane pore size. The pore size decreases from microfiltration (0.05 μm ~ 10 μm) to ultrafiltration (1 nm ~ 0.05 μm) to reverse osmosis (< 1 nm)[57]. As a result, the flux through the membrane decreases as the pore size decreases[17]. In addition to the pore size, membrane fouling also leads to a reduction in the flux. Pore clogging and/or preferential adsorption of liquid which fouls the surface are considered irreversible membrane fouling mechanisms[59,60]. Chemical treatments or membrane replacement is necessary once the flux through the membrane declines[61,62]. The formation of cake layers, another reason that leads to a decline in flux, can be mitigated through backflushing[63]. In addition to the flux and fouling resistance, selectivity is also an important characteristic of membranes. This is typically achieved by

taking advantage of preferential wettability of one phase over the other. Surface modification has been widely used to produce membranes that attain preferential wettability[64,65]. Although appropriate surface modification is effective in controlling selectivity as well as fouling resistance[60-62], it may lead to a reduction in membrane pore size and consequently a decrease in flux[66,67]. Thus, improvements in the performance of membranes often involve fouling mitigation and enhancing selectivity, while attempting to minimize the decline of flux.

1.4.2. Membranes for oil-water separation

The performance of membrane separation is affected by the properties of membrane materials. Membranes are divided into two groups: organic and inorganic membranes. The most important type of membrane materials is organic (polymer) due to their low cost, superior chemical and mechanical stability[68].

Polymers such as polysulfone, polytetrafluoroethylene (PTFE) and polyvinylidene fluoride (PVDF) have been widely used for microfiltration and ultrafiltration membranes to separate oil-water mixtures[69-72]. Most polymeric membranes intrinsically tend to be oleophilic, which leads to membrane fouling and a decline in flux during separation operation[32,33]. To overcome these limitations, modifying the wettability of membrane has attracted a lot of interest. If a membrane displays preferential wettability for oil and water such as hydrophobic (or superhydrophobic) and oleophilic (or superoleophilic), or hydrophilic (or superhydrophilic) and oleophobic (or superoleophobic), it may provide good selectivity required to achieve the desired separation of oil-water mixtures.

Hydrophobic and oleophilic membranes can selectively separate oil from oil-water mixtures. Due to its superior selectivity, high efficiency and applicability to absorb

oil from oil-spills, it has attracted broad attention. Typically separation of oil-water mixtures utilizing hydrophobic and oleophilic membranes is based on size exclusion and selective wettability. Such membranes are composed of hydrophobic and oleophilic chemical components and macroporous structures. They typically allow oil to permeate through while repelling water. To prepare hydrophobic and oleophilic membranes, surface modification of porous substrates has been developed and widely used. Usually, a metal mesh such as stainless steel[8,73], copper[74,75] and nickel[73] is used as a support and a porous substrate. Fluoro-polymers or molecules are commonly used as surface modification materials due to their low solid surface energy[8,75]. To enhance the affinity of a coating and to promote selective wettability, surface roughness is often introduced using electrochemical[74,75] and wet etching methods[73,76,77]. In addition to metal meshes, porous polymers have also been used as substrates[78]. Instead of modifying the surface of porous substrates, constructing porous structures directly on polymers is another method to fabricate hydrophobic and oleophilic membranes. Electrospinning[79] and spray coating[80] processes are commonly used methods to create polymer films with porous and rough structures. These membranes have relatively higher durability and stability during performance because their homogeneous chemical composition inhibits delamination of the coating materials[64].

Hydrophilic and oleophobic membranes, which can selectively separate water from oil-water mixtures, have attracted broad attention recently due to their unique advantages. While hydrophobic and oleophilic membranes are easily fouled by oil leading to a decline in the flux during operation, hydrophilic and oleophobic membranes are resistant to fouling due to their intrinsic oleophobicity. As a result, they show better

performance. In addition, hydrophilic and oleophobic membranes are suitable for gravity-driven separation because water naturally settles below the oil due to its higher density, forming a barrier layer that prevents oil permeation. By contrast, hydrophobic and oleophilic membranes are typically used in energy- intensive cross-flow filtration systems[81-83]. Furthermore, hydrophilic and oleophobic membranes are superior in fuel purification and in the separation of high viscosity oils[64]. In spite of these numerous advantages, it has been considered challenging to develop hydrophilic and oleophobic membranes because the surface tension of water is significantly higher than that of oil. Recently, a novel membrane, that achieves superhydrophilic and oleophobic properties when submerged in water was reported[84-86]. From Young's relation (see equation 1.1), hydrophilic surfaces in air can become oleophobic under water[84,85]. In the presence of rough structures, water readily wets and fills all the cavities present on a surface, leading to a composite solid-oil-water interface. Similar to the composite solid-oil-air interface formed on superoleophobic surfaces in air, this new composite interface shows superoleophobic properties. This is because water trapped in surface structures prevents the permeation of oil droplets, yielding superoleophobicity. Superhydrophilic and underwater superoleophobic membranes have been fabricated utilizing hydrogel coated meshes[86]. This membrane can selectively separate water from oil-water mixtures under gravity. In addition, it shows anti-fouling properties during separation, which is attributed to the low affinity for oil droplets on the membrane under water.

Although membranes with superhydrophilic and under water superoleophobic properties can be used for gravity-driven separation of oil-water mixtures, and are more resistant to fouling by oils[19], they are unsuitable for the separation of free oil-water

mixtures or water-in-oil emulsions because both oil and water can easily permeate through them, unless every pore within the membrane is pre-wet by water. Further, oil easily permeates through the membrane if water dries out from even a single pore within the superhydrophilic membrane, which can typically happen in a matter of minutes[31].

In contrast, superhydrophilic and in air oleophobic (or superoleophobic) membranes allow for the separation of oil-in-water emulsions, water-in-oil emulsions and free oil and water mixtures without any pre-wetting[31]. Hydrophilic (superhydrophilic) and in air oleophobic materials can be fabricated through proper molecular design by combining hydrophilic and low surface energy components[87]. This hydrophilic and oleophobic surface can be further amplified to superhydrophilic and superoleophobic surface when surface roughness is introduced[88]. The mechanism for the hydrophilicity and oleophobicity is interpreted as so-called "flip-flop" reconfiguration[89]. When a water droplet is placed onto the surface, the low surface energy constituent can reorganize and rearrange to allow water molecules to penetrate into the hydrophilic subsurface. This is possible because the low surface energy moieties remain in a relatively mobile state at the surface. On the other hand, when an oil droplet contacts the surface, it is repelled by low surface energy constituent, and has no affinity to the hydrophilic component[64,90]. After modifying the membrane's surface with hydrophilic and oleophobic materials, the membrane selectively allows only water to permeate through[88,90,91].

Blending a polymer matrix with hydrophilic and oleophobic polymers is also an effective method that can be readily achieved. Typically a hydrophilic polymer is blended with the host hydrophobic polymer membrane to improve fouling resistance and selectivity in the membrane separation[92-94]. However, introduction of hydrophilic

polymers may affect the membrane structure, especially the generation of defects in the membranes, which causes the collapse of membranes during operation[92]. In addition to polymer blends with hydrophilic and oleophobic polymers, inorganic nanoparticles have been used along with a host polymer[69,95,96]. Due to the large surface area and hydrophilicity of the nanoparticles, the addition of inorganic nanoparticles has been demonstrated to also be effective in improving membrane resistance to fouling by oils. However, it has been observed that nanoparticles easily form aggregates in the polymer membranes due to their poor dispersibility. Further, the membrane may suffer from the release of nanoparticles because there is no strong interaction with the host polymer[71].

1.5. Design parameters of membranes

The systematic design of membranes for oil-water separation requires the parameterization of two important physical characteristics. One is surface porosity, which affects the rate of permeation of one phase (for example water) through the membrane. Previous works[45,46] have discussed the spacing ratio, D^*, which provides a dimensionless measure of surface porosity. For membranes possessing a predominantly cylindrical texture, such as interwoven meshes or fabrics, $D^* = (R + D)/R$, where R is the radius of a cylinder and $2D$ is the inter-cylinder spacing. Surface porosity increases with increasing D^*. For surfaces possessing cylindrical or spherical texture, the Cassie-Baxter relation can be re-written in terms of D^* as[45]:

(Equation 1.6) $$\cos\theta^* = -1 + \frac{1}{D^*}[\sin\theta + (\pi - \theta)\cos\theta]$$

Higher values of D^* correspond to a higher fraction of air in the composite interface. Thus the surface will be highly non-wetting, i.e., the contacting liquids will

display high apparent contact angles, as long as the applied pressure differential across the membrane is smaller than the breakthrough pressure. Further, membranes with higher values of D^* will show a higher permeation rate for the contacting liquid.

The other vital physical characteristic is the breakthrough pressure $P_{breakthrough}$, the maximum pressure differential across the membrane below which the membrane prevents the permeation of a given liquid. The robustness factor A^* provides a convenient tool to predict the stability of the composite interfaces on membrane surfaces[34,45,46]. Large values of A^* ($A^* >> 1$) indicate the formation of a robust composite interface with very high breakthrough pressures. On the other hand, as A^* approaches unity, $P_{breakthrough}$ approaches P_{ref}. Thus, a composite interface on any surface for which $A^* < 1$ cannot maintain its stability against even small pressure differentials across the liquid–air interface, causing the liquid to penetrate into the textured surface and ultimately be fully imbibed. To achieve both a high permeation rate for one phase (for example, water) and a high breakthrough pressure for the other phase (for example, oil), the two design parameters, D^* and A^* must be maximized. For the membranes to have a high rate of permeation for water and a high breakthrough pressure for oil simultaneously, it is essential to design the membranes with $A^*_{water} \leq 1$, $A^*_{oil} > 1$, and also have high values of D^*.

However, D^* and A^* are strongly coupled for membranes with a periodic geometry of cylindrical features[45,46]. The values of D^* increase by either increasing D or reducing R (with the other geometric variable held constant), which leads to a decrease in A^* (see equation 1.5). Thus it is crucial to increase A^*_{oil} without affecting D^* in order for membranes to maintain a high rate of permeation for water, and a high breakthrough

pressures for oil simultaneously. Such an enhancement can be readily achieved by introducing low surface energy materials on the solid surface, which leads to increase in the values of Young's contact angle θ (see equation 1.1). Using this approach, the values of A^* and the breakthrough pressure increase without changing membrane geometry. However, lowering the surface energy of the solid may result in omniphobic surfaces, which can repel both water and oil[46,97-100]. If membranes are omniphobic, not only oil but also water is repelled by the membrane, and consequently selective permeation of water through such membranes may not be observed. To achieve hydrophilic (or superhydrophilic) and oleophobic (or superoleophobic) membranes, various approaches including blending hydrophilic and oleophobic materials[69,71,72,92-94], surface modification through chemical reactions[101-104], and synthesizing a molecule or polymer which consists of hydrophilic and oleophobic constituents[88,90,91] have been developed.

1.6. Separation of miscible liquids

The separation of miscible components from liquid mixtures is also important in many industries. For example, in the petroleum refining process, small amounts of miscible impurities including sulfur, nitrogen and metal compounds are separated from crude oil to produce fuel oil[105]. Similarly, the high quality of biofuels such as bioethanol or biodiesel can only be produced by removing byproducts generated during the separation process[106]. In addition, recovery of organic acids from agroindustrial wastewater is essential not only for environmental requirements, but also for economic benefits[107,108].

A large number of methodologies including distillation, evaporation and liquid-liquid extraction have been used to separate miscible components from a mixture. Distillation separates components from a mixture based on differences in their boiling points[2]. Distillation processes are used for the separation of organic chemicals in the chemical and petroleum refining industries. Since distillation is a simple and well-established technology, it is by far the most widely used separation process[1]. However, distillation has low energy efficiency and it requires thermal stability of compounds at their boiling points. In addition, it is not suitable for the separation of components with similar boiling points such as azeotropes. Although azeotropic distillation is used to separate such mixtures, it typically requires changing pressure[109,110] or the addition of other chemicals to form heterogeneous ternary azeotropes[111,112].

Liquid-liquid extraction is typically used to separate azeotropes and components with overlapping boiling points where simple distillation cannot be used. Liquid-liquid extraction is a separation technique that separates components of a liquid mixture by contact with another insoluble liquid. Components in a liquid mixture are separated based on their difference in solubility with the insoluble liquid[4]. Since liquid-liquid extraction can be operated at relatively low to moderate temperatures and near atmospheric pressure, large energy savings can be achieved by replacing distillation. One primary challenge in liquid-liquid extraction is to increase contact between the two liquid phases for efficient mass transfer. This is typically achieved by employing ultrasonication[113] or pumping the two liquids through packed columns with high tortuosity[114]. Emulsions, especially those stabilized by surfactants, are known to provide large interfacial area and consequently enhance the mass transfer during extraction[115,116]. However, subsequent separation of

those emulsions is challenging. Thus there is still a dire need to develop a novel methodology with enhanced mass transfer for extraction and the facile separation of emulsions.

1.7. References

1 Oak Ridge National Laboratory & BCS, I. *Materials Research for Separations Technologies: Energy and Emission Reduction Opportunities*. (2005).

2 Kister, H. *Distillation Operation*. 1 edn, (McGraw-Hill Professional, 1990).

3 J. D. Seader, E. J. H., D. Keith Roper. *Separation Process Principles*. (Wiley, 2011).

4 Treybal, R. E. *Liquid Extraction*. (Nabu Press, 2011).

5 Strathmann, H. *Introduction to Membrane Science and Technology*. (Wiley, 2011).

6 Kajitvichyanukul, P., Hung, Y.-T. & Wang, L. K. *Handbook of Environmental Engineering, Vol 13: Membrane and Desalination Technologies*. 639 (The Humana Press Inc., 2011).

7 Adebajo, M. O., Frost, R. L., Kloprogge, J. T., Carmody, O. & Kokot, S. Porous materials for oil spill cleanup: A review of synthesis and absorbing properties. *J Porous Mat* **10**, 159-170, (2003).

8 Feng, L., Zhang, Z. Y., Mai, Z. H., Ma, Y. M., Liu, B. Q., Jiang, L. & Zhu, D. B. A super-hydrophobic and super-oleophilic coating mesh film for the separation of oil and water. *Angew Chem Int Edit* **43**, 2012-2014, (2004).

9 Gossen, L. P. & Velichkina, L. M. Environmental problems of the oil-and-gas industry (Review). *Petrol Chem+* **46**, 67-72, (2006).

10 Yuan, J. K., Liu, X. G., Akbulut, O., Hu, J. Q., Suib, S. L., Kong, J. & Stellacci, F. Superwetting nanowire membranes for selective absorption. *Nat Nanotechnol* **3**, 332-336, (2008).

11 Shannon, M. A., Bohn, P. W., Elimelech, M., Georgiadis, J. G., Marinas, B. J. & Mayes, A. M. Science and technology for water purification in the coming decades. *Nature* **452**, 301-310, (2008).

12 Jenssen, B. M. Review Article - Effects of Oil Pollution, Chemically Treated Oil, and Cleaning on the Thermal Balance of Birds. *Environ Pollut* **86**, 207-215, (1994).

13 Peterson, C. H., Rice, S. D., Short, J. W., Esler, D., Bodkin, J. L., Ballachey, B. E. & Irons, D. B. Long-term ecosystem response to the Exxon Valdez oil spill. *Science* **302**, 2082-2086, (2003).

14 Kammerer, M., Mastain, O., Le Deran-Quenech'du, S., Pouliquen, H. & Larhantec, M. Liver and kidney concentrations of vanadium in oiled seabirds after the Erika wreck. *Sci Total Environ* **333**, 295-301, (2004).

15 Oki, T. & Kanae, S. Global hydrological cycles and world water resources. *Science* **313**, 1068-1072, (2006).

16 Iglesias, A., Garrote, L., Flores, F. & Moneo, M. Challenges to manage the risk of water scarcity and climate change in the Mediterranean. *Water Resour Manag* **21**, 775-788, (2007).

17 Cheryan, M. *Microfiltration and Ultrafiltration Handbook*. (Technomic Publishing, 1998).

18 Yang, S., Jin, X., Liu, K. S. & Jiang, L. Nanoparticles assembly-induced special wettability for bio-inspired materials. *Particuology* **11**, 361-370, (2013).
19 Cheryan, M. & Rajagopalan, N. Membrane processing of oily streams. Wastewater treatment and waste reduction. *J Membrane Sci* **151**, 13-28, (1998).
20 Pal, R. Multiple O/W/O emulsion rheology. *Langmuir* **12**, 2220-2225, (1996).
21 Khurana, J., Singh, S. & Dash, A. K. Multiple Emulsions An Overview and Pharmaceutical Applications. *Surfactant Sci Ser* **148**, 177-202, (2010).
22 Binks, B. P. Particles as surfactants - similarities and differences. *Curr Opin Colloid In* **7**, 21-41, (2002).
23 Tadros, T., Izquierdo, R., Esquena, J. & Solans, C. Formation and stability of nano-emulsions. *Adv Colloid Interfac* **108**, 303-318, (2004).
24 Al-Shamrani, A. A., James, A. & Xiao, H. Destabilisation of oil-water emulsions and separation by dissolved air flotation. *Water Res* **36**, 1503-1512, (2002).
25 Rubio, J., Souza, M. L. & Smith, R. W. Overview of flotation as a wastewater treatment technique. *Miner Eng* **15**, 139-155, (2002).
26 Al-Shamrani, A. A., James, A. & Xiao, H. Separation of oil from water by dissolved air flotation. *Colloid Surface A* **209**, 15-26, (2002).
27 Toyoda, M. & Inagaki, M. Heavy oil sorption using exfoliated graphite - New application of exfoliated graphite to protect heavy oil pollution. *Carbon* **38**, 199-210, (2000).
28 Gupta, V. K., Carrott, P. J. M., Carrott, M. M. L. R. & Suhas. Low-Cost Adsorbents: Growing Approach to Wastewater Treatmenta Review. *Crit Rev Env Sci Tec* **39**, 783-842, (2009).
29 Ichikawa, T. Electrical demulsification of oil-in-water emulsion. *Colloid Surface A* **302**, 581-586, (2007).
30 Rios, G., Pazos, C. & Coca, J. Destabilization of cutting oil emulsions using inorganic salts as coagulants. *Colloid Surface A* **138**, 383-389, (1998).
31 Kota, A. K., Kwon, G., Choi, W., Mabry, J. M. & Tuteja, A. Hygro-responsive membranes for effective oil-water separation. *Nat Commun* **3**, (2012).
32 Song, L. F. Flux decline in crossflow microfiltration and ultrafiltration: mechanisms and modeling of membrane fouling. *J Membrane Sci* **139**, 183-200, (1998).
33 Kong, J. & Li, K. Oil removal from oil-in-water emulsions using PVDF membranes. *Sep Purif Technol* **16**, 83-93, (1999).
34 Tuteja, A., Choi, W., Ma, M. L., Mabry, J. M., Mazzella, S. A., Rutledge, G. C., McKinley, G. H. & Cohen, R. E. Designing superoleophobic surfaces. *Science* **318**, 1618-1622, (2007).
35 Feng, X. J. & Jiang, L. Design and creation of superwetting/antiwetting surfaces. *Adv Mater* **18**, 3063-3078, (2006).
36 Arun K Kota, G. K., Anish Tuteja. The design and applications of superomniphobic surfaces. *Npg Asia Mater* **6**, (2014).
37 Young, T. An essay on the cohesion of fluids. *Philosophical Transactions of the Royal Society of London* **95**, 65, (1805).
38 Zisman, W. A. Relation of the equilibrium contact angle to liquid and solid construction. *In Contact Angle, Wettability and Adhesion, ACS Advances in Chemistry Series*, (1964).

39 Cassie, A. B. D. & Baxter, S. Wettability of porous surfaces. *T Faraday Soc* **40**, 0546-0550, (1944).

40 Wenzel, R. N. Resistance of solid surfaces to wetting by water. *Ind Eng Chem* **28**, 988-994, (1936).

41 Marmur, A. Wetting on hydrophobic rough surfaces: To be heterogeneous or not to be? *Langmuir* **19**, 8343-8348, (2003).

42 Marmur, A. From hygrophilic to superhygrophobic: Theoretical conditions for making high-contact-angle surfaces from low-contact-angle materials. *Langmuir* **24**, 7573-7579, (2008).

43 Quere, D. Rough ideas on wetting. *Physica A* **313**, 32-46, (2002).

44 McHale, G., Shirtcliffe, N. J. & Newton, M. I. Contact-angle hysteresis on super-hydrophobic surfaces. *Langmuir* **20**, 10146-10149, (2004).

45 Choi, W., Tuteja, A., Chhatre, S., Mabry, J. M., Cohen, R. E. & McKinley, G. H. Fabrics with Tunable Oleophobicity. *Adv Mater* **21**, 2190-2195, (2009).

46 Tuteja, A., Choi, W., Mabry, J. M., McKinley, G. H. & Cohen, R. E. Robust omniphobic surfaces. *P Natl Acad Sci USA* **105**, 18200-18205, (2008).

47 Sun, T. L., Feng, L., Gao, X. F. & Jiang, L. Bioinspired surfaces with special wettability. *Accounts Chem Res* **38**, 644-652, (2005).

48 Genzer, J. & Efimenko, K. Recent developments in superhydrophobic surfaces and their relevance to marine fouling: a review. *Biofouling* **22**, 339-360, (2006).

49 Leng, B. X., Shao, Z. Z., de With, G. & Ming, W. H. Superoleophobic Cotton Textiles. *Langmuir* **25**, 2456-2460, (2009).

50 Lee, C. & Kim, C. J. Underwater Restoration and Retention of Gases on Superhydrophobic Surfaces for Drag Reduction. *Phys Rev Lett* **106**, (2011).

51 Nosonovsky, M. Multiscale roughness and stability of superhydrophobic biomimetic interfaces. *Langmuir* **23**, 3157-3161, (2007).

52 Ahuja, A., Taylor, J. A., Lifton, V., Sidorenko, A. A., Salamon, T. R., Lobaton, E. J., Kolodner, P. & Krupenkin, T. N. Nanonails: A simple geometrical approach to electrically tunable superlyophobic surfaces. *Langmuir* **24**, 9-14, (2008).

53 Liu, J. L., Feng, X. Q., Wang, G. F. & Yu, S. W. Mechanisms of superhydrophobicity on hydrophilic substrates. *J Phys-Condens Mat* **19**, (2007).

54 Lafuma, A. & Quere, D. Superhydrophobic states. *Nat Mater* **2**, 457-460, (2003).

55 Noscinovsky, M. & Bhushan, B. Patterned nonadhesive surfaces: Superhydrophobicity and wetting regime transitions. *Langmuir* **24**, 1525-1533, (2008).

56 Treybal, R. E. *Mass-Transfer Operations*. (McGraw-Hill Book Company, 1980).

57 Mulder, M. *Basic Principles of Membrane Technology*. (Kluwer academic publishers, 1997).

58 Subramanian, G. *Bioseparation and Bioprocessing: A Handbook, 2 Volume Set, Volume 1*. (Wiley-VCH, 2007).

59 Wetterau, G. E., Clark, M. M. & Anselme, C. A dynamic model for predicting fouling effects during the ultrafiltration of a groundwater. *J Membrane Sci* **109**, 185-204, (1996).

60 Faibish, R. S. & Cohen, Y. Fouling-resistant ceramic-supported polymer membranes for ultrafiltration of oil-in-water microemulsions. *J Membrane Sci* **185**, 129-143, (2001).

61 Faibish, R. S. & Cohen, Y. Fouling and rejection behavior of ceramic and polymer-modified ceramic membranes for ultrafiltration of oil-in-water emulsions and microemulsions. *Colloid Surface A* **191**, 27-40, (2001).
62 Asatekin, A., Menniti, A., Kang, S. T., Elimelech, M., Morgenroth, E. & Mayes, A. M. Antifouling nanofiltration membranes for membrane bioreactors from self-assembling graft copolymers. *J Membrane Sci* **285**, 81-89, (2006).
63 Shi, Y. F., Jin, F. X. & Wu, Y. Y. Microfiltration membrane bioreactor in stirred backflush operation for biotransformation using intact cells. *Process Biochem* **32**, 387-390, (1997).
64 Xue, Z. X., Cao, Y. Z., Liu, N., Feng, L. & Jiang, L. Special wettable materials for oil/water separation. *J Mater Chem A* **2**, 2445-2460, (2014).
65 Zhu, Y. Z., Wang, D., Jiang, L. & Jin, J. Recent progress in developing advanced membranes for emulsified oil/water separation. *Npg Asia Mater* **6**, (2014).
66 Park, Y. S., Ito, Y. & Imanishi, Y. Photocontrolled gating by polymer brushes grafted on porous glass filter. *Macromolecules* **31**, 2606-2610, (1998).
67 Miyoshi, K., Saito, K., Shiraishi, T. & Sugo, T. Introduction of taurine into polymer brush grafted onto porous hollow-fiber membrane. *J Membrane Sci* **264**, 97-103, (2005).
68 Utracki, L. A. *Polymer Blends Handbook*. (2002).
69 Yi, X. S., Yu, S. L., Shi, W. X., Sun, N., Jin, L. M., Wang, S., Zhang, B., Ma, C. & Sun, L. P. The influence of important factors on ultrafiltration of oil/water emulsion using PVDF membrane modified by nano-sized TiO2/Al2O3. *Desalination* **281**, 179-184, (2011).
70 Mansouri, J., Harrisson, S. & Chen, V. Strategies for controlling biofouling in membrane filtration systems: challenges and opportunities. *J Mater Chem* **20**, 4567-4586, (2010).
71 Yang, Y. N., Zhang, H. X., Wang, P., Zheng, Q. Z. & Li, J. The influence of nano-sized TiO2 fillers on the morphologies and properties of PSFUF membrane. *J Membrane Sci* **288**, 231-238, (2007).
72 Li, Y. S., Yan, L., Xiang, C. B. & Hong, L. J. Treatment of oily wastewater by organic-inorganic composite tubular ultrafiltration (UF) membranes. *Desalination* **196**, 76-83, (2006).
73 Li, M., Xu, J. H. & Lu, Q. H. Creating superhydrophobic surfaces with flowery structures on nickel substrates through a wet-chemical-process. *J Mater Chem* **17**, 4772-4776, (2007).
74 Wang, S. T., Song, Y. L. & Jiang, L. Photoresponsive surfaces with controllable wettability. *J Photoch Photobio C* **8**, 18-29, (2007).
75 La, D. D., Tuan, A. N., Lee, S., Kim, J. W. & Kim, Y. S. A stable superhydrophobic and superoleophilic Cu mesh based on copper hydroxide nanoneedle arrays. *Appl Surf Sci* **257**, 5705-5710, (2011).
76 Wang, C. X., Yao, T. J., Wu, J., Ma, C., Fan, Z. X., Wang, Z. Y., Cheng, Y. R., Lin, Q. & Yang, B. Facile Approach in Fabricating Superhydrophobic and Superoleophilic Surface for Water and Oil Mixture Separation. *Acs Appl Mater Inter* **1**, 2613-2617, (2009).

77 Pan, Q. M., Wang, M. & Wang, H. B. Separating small amount of water and hydrophobic solvents by novel superhydrophobic copper meshes. *Appl Surf Sci* **254**, 6002-6006, (2008).
78 Zhang, J. L., Huang, W. H. & Han, Y. C. A composite polymer film with both superhydrophobicity and superoleophilicity. *Macromol Rapid Comm* **27**, 804-808, (2006).
79 Wang, L. F., Yang, S. Y., Wang, J., Wang, C. F. & Chen, L. Fabrication of superhydrophobic TPU film for oil-water separation based on electrospinning route. *Mater Lett* **65**, 869-872, (2011).
80 Tu, C. W., Tsai, C. H., Wang, C. F., Kuo, S. W. & Chang, F. C. Fabrication of superhydrophobic and superoleophilic polystyrene surfaces by a facile one-step method. *Macromol Rapid Comm* **28**, 2262-2266, (2007).
81 Hlavacek, M. Break-up of Oil-in-Water Emulsions Induced by Permeation through a Microfiltration Membrane. *J Membrane Sci* **102**, 1-7, (1995).
82 Maartens, A., Jacobs, E. P. & Swart, P. UF of pulp and paper effluent: membrane fouling-prevention and cleaning. *J Membrane Sci* **209**, 81-92, (2002).
83 Hu, B. & Scott, K. Influence of membrane material and corrugation and process conditions on emulsion microfiltration. *J Membrane Sci* **294**, 30-39, (2007).
84 Xue, Z. X., Liu, M. J. & Jiang, L. Recent developments in polymeric superoleophobic surfaces. *J Polym Sci Pol Phys* **50**, 1209-1224, (2012).
85 Liu, M. J., Wang, S. T., Wei, Z. X., Song, Y. L. & Jiang, L. Bioinspired Design of a Superoleophobic and Low Adhesive Water/Solid Interface. *Adv Mater* **21**, 665-669, (2009).
86 Xue, Z. X., Wang, S. T., Lin, L., Chen, L., Liu, M. J., Feng, L. & Jiang, L. A Novel Superhydrophilic and Underwater Superoleophobic Hydrogel-Coated Mesh for Oil/Water Separation. *Adv Mater* **23**, 4270-4273, (2011).
87 Wang, Y., Dong, Q. B., Wang, Y. X., Wang, H., Li, G. A. & Bai, R. K. Investigation on RAFT Polymerization of a Y-Shaped Amphiphilic Fluorinated Monomer and Anti-Fog and Oil-Repellent Properties of the Polymers. *Macromol Rapid Comm* **31**, 1816-1821, (2010).
88 Yang, J., Zhang, Z. Z., Xu, X. H., Zhu, X. T., Men, X. H. & Zhou, X. Y. Superhydrophilic-superoleophobic coatings. *J Mater Chem* **22**, 2834-2837, (2012).
89 Sawada, H., Ikematsu, Y., Kawase, T. & Hayakawa, Y. Synthesis and surface properties of novel fluoroalkylated flip-flop-type silane coupling agents. *Langmuir* **12**, 3529-3530, (1996).
90 Howarter, J. A. & Youngblood, J. P. Amphiphile grafted membranes for the separation of oil-in-water dispersions. *J Colloid Interf Sci* **329**, 127-132, (2009).
91 Gao, D. Superoleophobic and Superhydrophilic Fabric Filters for Rapid Water-Oil Separation. (2011).
92 Ochoa, N. A., Masuelli, M. & Marchese, J. Effect of hydrophilicity on fouling of an emulsified oil wastewater with PVDF/PMMA membranes. *J Membrane Sci* **226**, 203-211, (2003).
93 Masuelli, M., Marchese, J. & Ochoa, N. A. SPC/PVDF membranes for emulsified oily wastewater treatment. *J Membrane Sci* **326**, 688-693, (2009).

94 Bowen, W. R., Cheng, S. Y., Doneva, T. A. & Oatley, D. L. Manufacture and characterisation of polyetherimide/sulfonated poly(ether ether ketone) blend membranes. *J Membrane Sci* **250**, 1-10, (2005).
95 Yan, L., Li, Y. S. & Xiang, C. B. Preparation of poly(vinylidene fluoride)(pvdf) ultrafiltration membrane modified by nano-sized alumina (Al2O3) and its antifouling research. *Polymer* **46**, 7701-7706, (2005).
96 Yan, L., Li, Y. S., Xiang, C. B. & Xianda, S. Effect of nano-sized Al2O3-particle addition on PVDF ultratiltration membrane performance. *J Membrane Sci* **276**, 162-167, (2006).
97 Golovin, K., Lee, D. H., Mabry, J. M. & Tuteja, A. Transparent, Flexible, Superomniphobic Surfaces with Ultra-Low Contact Angle Hysteresis. *Angew Chem Int Edit* **52**, 13007-13011, (2013).
98 Kota, A. K., Choi, W. & Tuteja, A. Superomniphobic surfaces: Design and durability. *Mrs Bull* **38**, 383-390, (2013).
99 Pan, S. J., Kota, A. K., Mabry, J. M. & Tuteja, A. Superomniphobic Surfaces for Effective Chemical Shielding. *J Am Chem Soc* **135**, 578-581, (2013).
100 Hensel, R., Finn, A., Helbig, R., Braun, H. G., Neinhuis, C., Fischer, W. J. & Werner, C. Biologically Inspired Omniphobic Surfaces by Reverse Imprint Lithography. *Adv Mater* **26**, 2029-2033, (2014).
101 Belfer, S., Fainshtain, R., Purinson, Y., Gilron, J., Nystrom, M. & Manttari, M. Modification of NF membrane properties by in situ redox initiated graft polymerization with hydrophilic monomers. *J Membrane Sci* **239**, 55-64, (2004).
102 Rahimpour, A., Madaeni, S. S., Zereshki, S. & Mansourpanah, Y. Preparation and characterization of modified nano-porous PVDF membrane with high antifouling property using UV photo-grafting. *Appl Surf Sci* **255**, 7455-7461, (2009).
103 Zhu, Y. Z., Zhang, F., Wang, D., Pei, X. F., Zhang, W. B. & Jin, J. A novel zwitterionic polyelectrolyte grafted PVDF membrane for thoroughly separating oil from water with ultrahigh efficiency. *J Mater Chem A* **1**, 5758-5765, (2013).
104 Zhao, X. T., Su, Y. L., Chen, W. J., Peng, J. M. & Jiang, Z. Y. Grafting perfluoroalkyl groups onto polyacrylonitrile membrane surface for improved fouling release property. *J Membrane Sci* **415**, 824-834, (2012).
105 Meyers, R. A. *Handbook of Petroleum Refining Processes*. (McGraw-Hill, 2004).
106 Birgit Kamm, P. R. G., Michael Kamm. *Biorefineries - industrial processes and products*. (Wiley-VCH, 2006).
107 Yu, L. X., Guo, Q. F., Hao, J. H. & Jiang, W. J. Recovery of acetic acid from dilute wastewater by means of bipolar membrane electrodialysis. *Desalination* **129**, 283-288, (2000).
108 Hong, Y. K. & Hong, W. H. Removal of acetic acid from aqueous solutions containing succinic acid and acetic acid by tri-n-octylamine. *Sep Purif Technol* **42**, 151-157, (2005).
109 Luyben, W. L. Pressure-Swing Distillation for Minimum- and Maximum-Boiling Homogeneous Azeotropes. *Ind Eng Chem Res* **51**, 10881-10886, (2012).
110 Knapp, J. P. & Doherty, M. F. A New Pressure-Swing-Distillation Process for Separating Homogeneous Azeotropic Mixtures. *Ind Eng Chem Res* **31**, 346-357, (1992).

111 Li, G. Z. & Bai, P. New Operation Strategy for Separation of Ethanol-Water by Extractive Distillation. *Ind Eng Chem Res* **51**, 2723-2729, (2012).
112 Orchilles, A. V., Miguel, P. J., Vercher, E. & Martinez-Andreu, A. Ionic liquids as entrainers in extractive distillation: Isobaric vapor-liquid equilibria for acetone plus methanol plus 1-ethyl-3-methylimidazolium trifluoromethanesulfonate. *J Chem Eng Data* **52**, 141-147, (2007).
113 Delgado-Povedano, M. M. & de Castro, L. Ultrasound-assisted analytical emulsification-extraction. *Trac-Trend Anal Chem* **45**, 1-13, (2013).
114 Gabelman, A. & Hwang, S. T. Hollow fiber membrane contactors. *J Membrane Sci* **159**, 61-106, (1999).
115 Kralj, J. G., Schmidt, M. A. & Jensen, K. F. Surfactant-enhanced liquid-liquid extraction in microfluidic channels with inline electric-field enhanced coalescence. *Lab Chip* **5**, 531-535, (2005).
116 Huebner, A., Sharma, S., Srisa-Art, M., Hollfelder, F., Edel, J. B. & Demello, A. J. Microdroplets: A sea of applications? *Lab Chip* **8**, 1244-1254, (2008).

CHAPTER 2

Hygro-responsive membranes for effective oil-water separation[1]

2.1. Introduction

With environmental increasing awareness and tighter regulations, there is a critical need to develop sustainable and energy-efficient strategies to separate oils from domestic and industrial wastewaters, and to protect sensitive ecosystems from marine oil-spills[2]. Oil and water can exist in several forms in the presence of surfactants (or dispersants): free, dispersed or emulsified. Surfactant-stabilized mixtures of oil and water are classified, in terms of the diameter (d) of the dispersed phase, as free oil and water if $d > 150$ μm, a dispersion if 20 μm $\leq d \leq$ 150 μm, or an emulsion if $d < 20$ μm[3]. Conventional gravity separators and skimming techniques are incapable of separating emulsions[3]. Membrane-based technologies are attractive for demulsification (the conversion of an emulsion to a free oil-water mixture) because they are relatively energy-efficient, cost-effective and applicable across a wide range of industrial effluents[3]. However, for complete oil-water separation, demulsification is typically followed by either gravity separation of skimming.

Membranes are typically classified as either hydrophobic or hydrophilic[4-10]. Their wettability by oil is often not specified because, in most cases, such membranes are oleophilic. Hydrophobic (or superhydrophobic[9-11]) and oleophilic membranes are typically used in energy-intensive cross-flow filtration systems because they are unsuitable for gravity-driven oil-water separation[4,7,12]. This is because water naturally settles below oil and against the membrane owing to its higher density, forming a barrier layer that prevents oil permeation. Hydrophobic and oleophilic membranes are also easily fouled by oil during demulsification[7,12]. Although conventional hydrophilic membranes can be used for gravity-driven demulsification, and are more resistant to fouling[3], they are unsuitable for the separation of free oil-water mixtures or water-in-oil emulsions because both oil and water can easily permeate through them (see figure 2.1). In addition, conventional hydrophilic membranes are required to be soaked by water repeatedly to prevent permeation of oil.

The hydrophilic-lipophilic balance (HLB) of the surfactant can be used to predict the formation of either an oil-in-water or a water-in-oil emulsion[13]. However, depending on the concentration of the dispersed phase and/or the temperature, an oil-in-water emulsion may invert to a water-in-oil emulsion or vice-versa[14]. In addition, as many as three different phases (oil, oil-in-water emulsion or water-in-oil emulsion and water) may co-exist in oil-water mixtures[14,15]. To effect gravity-driven separation of all types of oil-water mixtures in a single step, the ideal membrane is expected to be hydrophilic (or superhydrophilic[16]) and oleophobic (or superoleophobic[17]), both in air and when submerged in water. However, a membrane that is oleophobic in air typically loses its oleophobicity under water, and vice-versa[18,19].

In this work, we develop novel membranes with hygro-responsive surfaces[20], which are both sueperhydrophilic ($\theta^*_{water} \approx 0^\circ$) and sueperoleophobic ($\theta^*_{oil} > 150^\circ$) both in air and under water. Our membrane can separate several liters of oil-water mixtures, including surfactant-stabilized emulsions, solely using gravity, in a single-unit operation, with > 99.9% separation efficiency, by using the difference in capillary forces acting on the two phases. Our separation methodology is solely gravity-driven and consequently is expected to be highly energy-efficient. We demonstrate the separation of several liters of oil-water mixtures using a scaled-up apparatus. We also demonstrate continuous separation of oil-water emulsions for over 100 h without a decrease in flux.

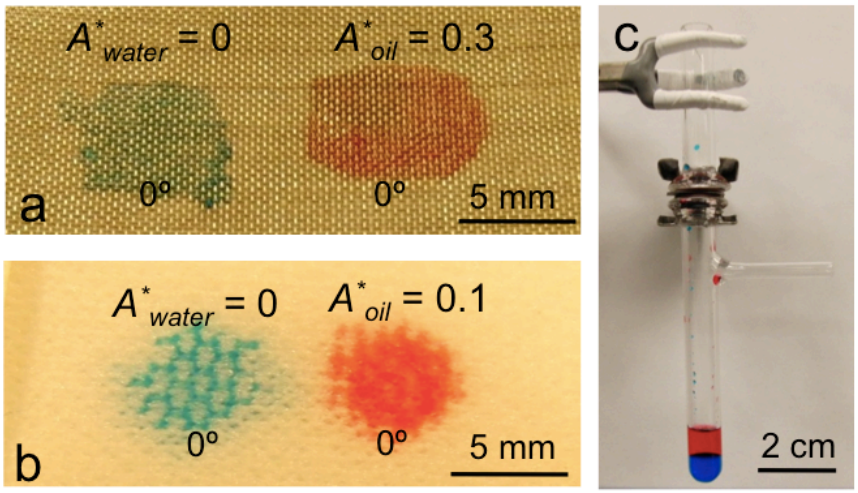

Figure 2.1 Conventional hydrophilic and oleophilic membranes. (a) and (b) Neat x-PEGDA dip-coated mesh 100 and polyester fabric membranes, respectively (see section 2.2.). Both water (dyed blue) and rapeseed oil (dyed red) readily permeate through these membranes. (c) A mesh 100 coated with neat x-PEGDA sandwiched between two vertical glass tubes. Both water and rapeseed oil readily permeate through the membrane.

2.2. Experimental Procedure

2.2.1. Materials

Poly(ethylene glycol)diacrylate (PEGDA) with a number-average molecular mass of $M_n \approx 700$ Da and its cross-linker 2-hydroxy-2-methyl propiophenone (Dacocur 1173) were obtained from Sigma Aldrich. Tecnoflon BR9151 fluoroelastomer was obtained from Solvay Solexis. Desmopan9370 polyurethane was obtained from Bayer Material Science. 1H, 1H, 2H, 2H-heptadecafluorodecyl polyhedral oligomeric silsequioxane (fluorodecyl POSS) was synthesized as described elsewhere[17]. Asahiklin AK-225 solvent was obtained from Structure Probe, Inc. Rapeseed oil, hexadecane, tetrahydrofuran, methylene blue (blue dye), oil red-o (red dye), sodium dodecyl sulphate (SDS), polysorbate 80 (PS80) and span 80 were obtained from Fisher Scientific. Stainless steel meshes of mesh size 100 (R = 56.5 μm, $2D$ = 138 μm, D^* = 2.2), 400 (R = 12.5 μm, $2D$ = 37.5 μm, D^* = 2.5), 500 (R = 10.2 μm, $2D$ = 30.5 μm, D^* = 2.5) were obtained from McMaster Carr. The mesh number refers to the number of openings per inch. The fabric Anticon 100 (R_{bundle} = 150 μm, $2D_{bundle}$ = 300 μm, R_{fiber} = 5 μm, $2D_{fiber}$ = 20 μm; D^* = 6 as described elsewhere[21]) was obtained from VWR. Silicon wafers were obtained from the clean room at the University of Michigan.

2.2.2. Substrate preparation

Solutions (100 mg/ml) of PEGDA, Darocur1173 and fluorodecyl POSS were prepared in Asahiklin AK-225. The PEGDA:Darcour1173 ratio was 95:5 w:w. The fluorodecyl POSS concentrations studied were 0, 0.5, 1, 2, 5, 10, 15 and 20 wt%. Solutions (10 mg/ml) of Desmopan were prepared in tetrahydrofuran. Small pieces of mesh and fabric (2 cm × 2 cm) were dip-coated in the desired solution for 10 min and

dried with nitrogen gas at room temperature (~ 22°C) for 5 min. The non-textured substrates (silicon wafers, 2 cm × 2 cm) were spin-coated using Speciality Coating Systems Spincoater G3P-8 for 30 s at 250−2,000 r.p.m. (0.7*g*–44.7*g*). After dip-coating or spin-coating, the PEGDA containing surfaces were cross-linked for 5 min using a UVP XX-40S UV bench lamp (wavelength, 254 nm). The thickness of the dip-coated layer varied between 100 nm and 1 μm.

2.2.3. Oil-water emulsions

Hexadecane-in-water emulsions (10:90 v:v, 30:70 v:v and 50:50 v:v) were prepared by mixing water and hexadecane using a stir bar (at 700−1,200 r.p.m., or 3.4*g*−10.1*g*) with 0.1–0.5 mg of sodium dodecyl sulphate per milliliter of emulsion, whereas 10:90 v:v, 20:80 v:v and 30:70 v:v water-in-hexadecane emulsions were prepared with 0.1–0.3 mg of PS80 per milliliter of emulsion and 0.1–0.3 mg of span 80 per milliliter of emulsion. Over time, a small degree of demulsification was observed for some emulsions. We determined whether an emulsion is hexadecane-in-water or water-in-hexadecane by measuring the electrical resistance with a multimeter. A KDScientific KDS-200 syringe pump was used to deliver the feed emulsions during continuous separation.

2.2.4. Characterization techniques

2.2.4.1. Contact angle measurements

All measurements of contact angle (in air and under water) were conducted using a Ramé–Hart 200-F1 goniometer. All contact angles reported in this work were measured by advancing or receding a small volume of liquid (~2 μl) onto the surface using a 2-ml

micrometer syringe (Gilmont). At least three measurements were performed on each substrate. The typical error in measurements was ±2°.

2.2.4.2. Microscopy

Tapping-mode atomic force microscopy was conducted in air and under water using a Veeco Innova instrument. Veeco TESPA tips were used for imaging in air, and Veeco SNL-10C tips were used for imaging under water. The thickness of the spin-coated films was determined using an AFM line scan across a scratched location. To ensure conformal coating, scanning electron microscopy of the dip-coated surfaces was conducted using a Hitachi SU8000 at 5 kV. Optical microscopy of the dry and wet spin-coated surfaces was conducted using an Olympus BH-2 optical microscope.

2.2.4.3. Separation efficiency and droplet size distribution

The water content in both the hexadecane-rich phase and the water-rich phase after separation was measured using a Perkin Elmer Pyris 1 TGA. Approximately 50 mg of the sample was heated from room temperature to 105 °C at a rate of 5 °C /min, and the temperature was held constant at 105 °C for 60 min. Note that the boiling point of hexadecane is 287 °C. The loss in weight of water was used to estimate the purity of the water-rich phase. The loss in weight of the hexadecane-rich phase was compared with the loss in weight of the as-obtained hexadecane to estimate the purity of the hexadecane-rich phase. The water content in the hexadecane-rich phase was also determined by injecting samples ranging in volume from 10 μl to 0.6 ml into an EM Science AquaStar C3000 Titrator for coulometric Karl Fischer titration analysis (ASTM D6304). The transmittance of the feed emulsions and the permeates was measured using a Cary 50 Bio UV-Vis spectrophotometer. The size distribution of the dispersed phase with droplet sizes less

than 1 μm was determined by dynamic light scattering using a Malvern Zetasizer Nano ZS instrument.

2.3. Results and discussion

2.3.1. Wetting behavior of water and oil

Figures 2.2a and 2.2b show the wetting behavior of water (γ_{lv} = 72.1 mN/m) and rapeseed oil (γ_{lv} = 35.7 mN/m) on a stainless steel mesh 100 (Figure 2.2a, inset) and polyester fabric (Figure 2.2b, inset), each dip-coated with a blend of 20 wt% fluorodecyl POSS and cross-linked PEGDA (x-PEGDA). For a surface spin-coated with a 20 wt% fluorodecyl POSS + x-PEGDA blend (solid surface energy γ_{sv} = 10.5 mN/m, see section 2.3.2 and Table 2.1), the advancing contact angle for rapeseed oil is $\theta_{oil,adv}$ = 88°. This yields A^*_{oil} values of 8.6 and 4.3 for rapeseed oil on the mesh and fabric membranes, respectively. Because D^*_{fabric} = 6 is greater than D^*_{mesh} = 2.2, the observed apparent advancing contact angle on the dip-coated fabric ($\theta^*_{oil,adv}$ = 152°) is higher than that on mesh 100 ($\theta^*_{oil,adv}$ = 125°). However, despite their low surface energies, both the fabric and the mesh membranes are readily permeated by water, with $\theta^*_{water,adv}$ = 0°. This is a direct consequence of the surface reconfiguration induced by the contacting water droplet.

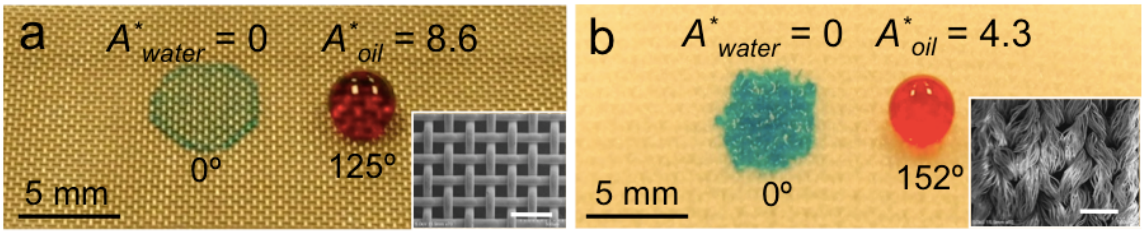

Figure 2.2 Wetting behavior of water and oil. (a) and (b) Droplets of water (dyed blue) and rapeseed oil (dyed red) on stainless steel mesh 100 (a) and polyester fabric (b). Both surfaces have been dip-coated with a 20 wt% fluorodecyl POSS + x-PEGDA blend. Insets, morphologies of the respective dip-coated mesh and fabric surfaces. Scale bars, 500 µm.

Figures 2.3a-c shows atomic force microscope (AFM) phase images of x-PEGDA and two fluorodecyl POSS + x-PEGDA blends, in air. Whereas crystalline domains are absent on the neat x-PEGDA surface (figure 2.3a), the surfaces of both the 10 wt% (figure 2.3b) and the 20 wt% (figure 2.3c) blends are completely covered with crystalline domains of fluorodecyl POSS. This indicates substantial surface segregation of the fluorodecyl POSS molecules, as may be expected owing to their extremely low surface energies[17].

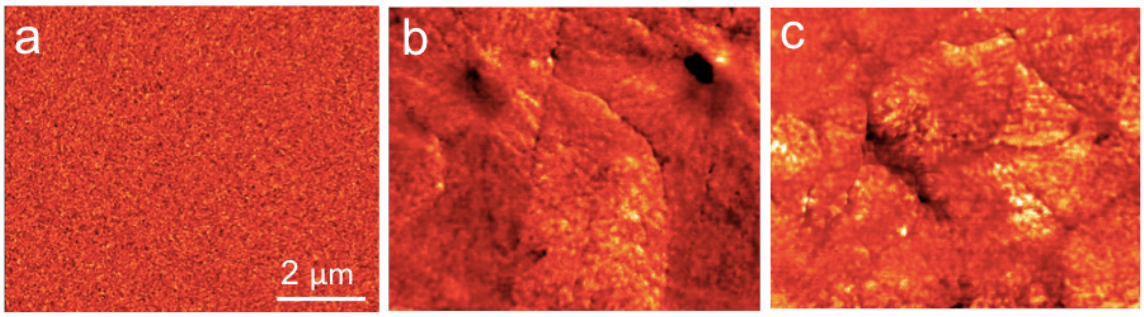

Figure 2.3 AFM phase images of surfaces coated with x-PEGDA (a), a 10 wt% fluorodecyl POSS + x-PEGDA blend (b) and a 20 wt% fluorodecyl POSS + x-PEGDA blend (c). The phase angle ranges are 0°-115° (a), 0°-25° (b) and 0°-21° (c).

2.3.2. Estimation of the solid surface energy

The equilibrium configuration of a liquid drop on a smooth solid surface is given by the Young's equation (see equation 1.1). Of the four parameters in equation 1.1, the liquid surface tension γ_{lv} and the equilibrium contact angle θ are readily measurable. In order to determine both the solid surface energy γ_{sv} and the solid-liquid interfacial energy γ_{sl}, another relationship between γ_{sv} and γ_{sl} is required. Historically, this additional relationship is obtained from an equation of state approach[22] or a surface energy component approach[23,24]. We adopted the surface energy component approach prescribed by Owens and Wendt[24] to estimate γ_{sv}. According to this approach, the solid surface energy is the sum of contributions from two types of intermolecular forces at the surface:

(Equation 2.1) $\gamma_{sv} = \gamma_{sv}^{d} + \gamma_{sv}^{p}$

Here γ_{sv}^{d} is the component that accounts for the dispersive forces, while γ_{sv}^{p} is the component that accounts for the polar forces, such as hydrogen bonding. Further, this approach postulates that:

(Equation 2.2) $\gamma_{sl} = \gamma_{sv} + \gamma_{lv} - 2\sqrt{\gamma_{sv}^{d}\gamma_{lv}^{d}} - 2\sqrt{\gamma_{sv}^{p}\gamma_{lv}^{p}}$

Here, γ_{lv}^{d} and γ_{lv}^{p} are the dispersive and polar components of the liquid surface tension, respectively. Combining equations 2.1 and 2.2 with the Young's equation (equation 1.1.) and recognizing that the polar component of liquid surface tension is zero (γ_{lv}^{p} = 0) for non-polar liquids such as oils, the dispersive component of solid surface energy is given as:

(Equation 2.3) $\gamma_{sv}^{d} = \gamma_{lv}\left(\frac{1+\cos\theta}{2}\right)^{2}$

In equation 2.3, γ_{lv} is the surface tension of a non-polar liquid and θ is the equilibrium contact angle of the same non-polar liquid on the solid surface. We used rapeseed oil (γ_{lv} = 35.7 mN/m) as the non-polar liquid to estimate γ_{sv}^{d}. After determining the dispersive component γ_{sv}^{d}, the polar component of the solid surface energy is determined using a polar liquid ($\gamma_{lv}^{p} \neq 0$) given as:

(Equation 2.4) $\gamma_{sv}^{p} = \frac{1}{\gamma_{lv}^{p}}\left[\frac{\gamma_{lv}(1+\cos\theta)}{2} - \sqrt{\gamma_{sv}^{d}\gamma_{lv}^{d}}\right]^{2}$

In equation 2.4, γ_{lv} is the surface tension of a polar liquid and θ is the equilibrium contact angle for the same polar liquid on the solid surface. We used water (γ_{lv}^{d} = 21.1 mN/m and γ_{lv}^{p} = 51.0 mN/m) as the polar liquid to estimate γ_{sv}^{p}.

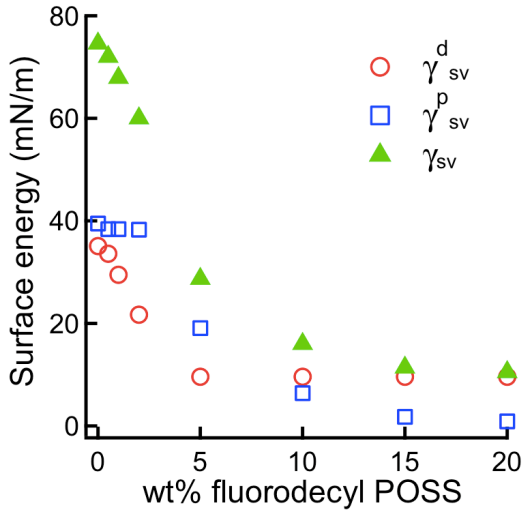

Figure 2.4 Solid surface energy. The polar component (γ_{sv}^{p}), the dispersive component (γ_{sv}^{d}), and the total surface energy (γ_{sv}) values for the as-prepared fluorodecyl POSS + x-PEGDA blends.

We estimated solid surface energy values for the as-prepared fluorodecyl POSS + x-PEGDA blends using this approach. Figure 2.4 shows that both the dispersive (γ_{sv}^{d}) and the polar components (γ_{sv}^{p}) of the blend surface energy rapidly decrease with increase fluorodecyl POSS concentration. This is due to surface migration of fluorodecyl POSS molecules. Table 2.1 summarizes the solid surface energy values estimated by this approach using spin-coated flat substrates. Note that for all surfaces containing x-PEGDA, the contact angles of water reported in Table 2.1 are the instantaneous values observed when water first contacts the solid surface. These values were used to estimate γ_{sv}^{p}.

Table 2.1 Contact angles and surface energies for the materials used.

Solid surface	$\theta_{oil,adv}$	$\theta_{oil,rec}$	$\theta_{water,adv}$	$\theta_{water,rec}$	γ_{sv}^{d} (mN/m)	γ_{sv}^{p} (mN/m)	γ_{sv} (mN/m)
x-PEGDA	10º	0º	0º	0º	35.2	39.5	74.7
0.5 wt% fluorodecyl POSS + x-PEGDA	20º	0º	15º*	0º	33.6	38.4	72.0
1 wt% fluorodecyl POSS + x-PEGDA	35º	0º	23º*	0º	29.5	38.4	67.9
2 wt% fluorodecyl POSS + x-PEGDA	56º	0º	35º*	0º	21.7	38.3	60.0
5 wt% fluorodecyl POSS + x-PEGDA	88º	76º	75º*	0º	9.6	19.1	28.7
10 wt% fluorodecyl POSS + x-PEGDA	88º	82º	96º*	0º	9.6	6.4	16.0
15 wt% fluorodecyl POSS + x-PEGDA	88º	81º	110º*	0º	9.6	1.8	11.4
20 wt% fluorodecyl POSS + x-PEGDA	88º	85º	115º*	0º	9.6	0.9	10.5
Desmopan	20º	10º	89º	52º	33.6	2.0	35.6
50 wt% fluorodecyl POSS + Tecnoflon	88º	78º	120º	100º	9.6	0.3	9.9

*This is the advancing contact angle of water when water first contacts the reconfigurable surfaces. After a short duration (the time of wetting), the contact angle on these surfaces reduces to 0º.

2.3.3. Surface reconfiguration

Figure 2.5a and 2.5b display optical images of spin-coated surfaces of 20 wt% fluorodecyl POSS + x-PEGDA, in air (figure 2.5a) and under water (figure 2.5b). In air, the surface is relatively rough, with several fluorodecyl POSS aggregates. However, under water, fluorodecyl POSS aggregates disappear to reveal a smoother surface that is indicative of surface reconfiguration. PEGDA chains reconfigure to increase their interfacial area with water and facilitate enthalpic gains through hydrogen bonding. Surface reconfiguration is further confirmed by the absence of large crystalline domains in the *in situ*, underwater AFM phase image (figure 2.5c).

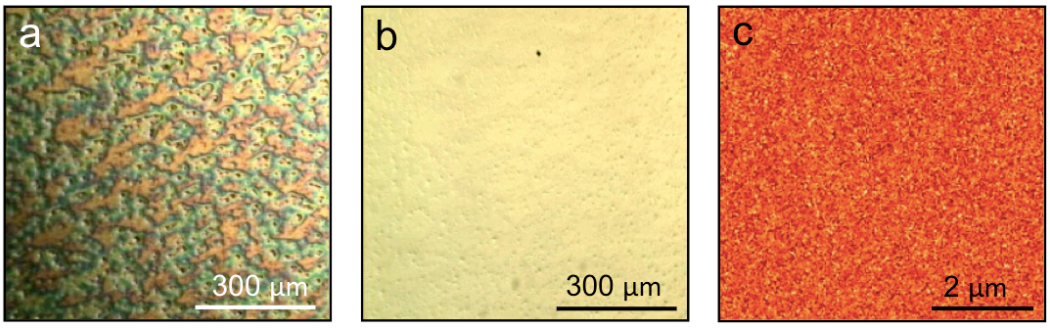

Figure 2.5 Surface reconfiguration. (a) and (b) Optical microscopy images of a surface coated with a 20 wt% fluorodecyl POSS + x-PEGDA blend in air (a) and under water (b). (c) In situ, underwater AFM phase image of a surface coated with a 20 wt% fluorodecyl POSS + x-PEGDA blend. The phase angle range is 0º-112º.

We conducted multiple water wetting–drying cycles and found that this surface reconfiguration is reversible. Figure 2.6a shows drops of rapeseed oil (dyed red) at three different locations on a substrate spin-coated with a 20 wt% fluorodecyl POSS + x-PEGDA blend. At an as-prepared and dry location (i), rapeseed oil shows a contact angle of θ_{oil} = 88° because majority of the surface is covered with fluorodecyl POSS domains.

At a location wet by water (ii), the contact angle of rapeseed oil is significantly lower (θ_{oil} = 45°), indicating that the surface has reconfigured to expose the PEGDA chains. At a location that was previously wet by water and subsequently dried completely (iii), rapeseed oil once again shows a contact angle of θ_{oil} = 88°, indicating that the surface has reverted back to its original configuration, i.e., fluorodecyl POSS domains cover the majority of the surface once again. This reversible stimuli-responsive surface reconfiguration is similar to the so-called "flip-flop" mechanism discussed in previous reports[25,26]. We conducted multiple water wetting-drying cycles and found the rapeseed oil contact angle at a fixed location to cycle between θ_{oil} ~ 88º (dry) and θ_{oil} ~ 45º, as shown in Figure 2.6b.

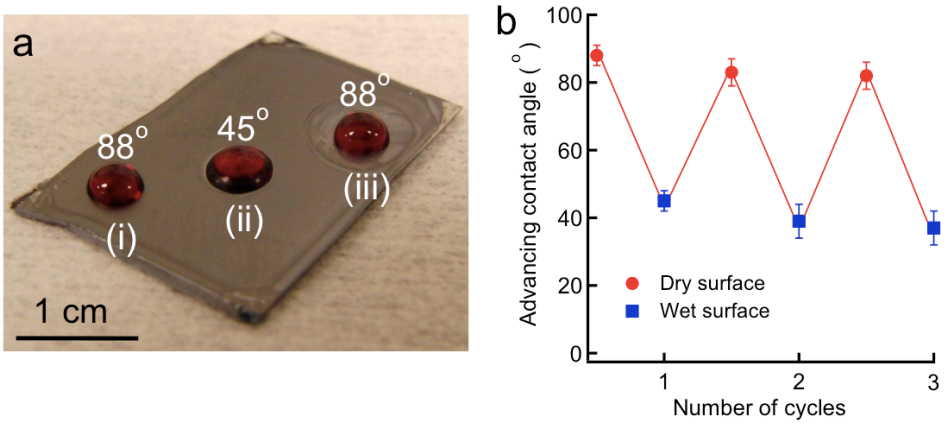

Figure 2.6 Reversible surface reconfiguration. (a) rapeseed oil (i) at a dry location, (ii) at a location previously wet by water, (iii) at a location that was wet by water and subsequently dried. (b) Contact angle of rapeseed oil as a function of water wetting-drying cycles.

We can also theoretically estimate the degree of surface reconfiguration, i.e., the relative amounts of x-PEGDA and fluorodecyl POSS in a solid surface previously wet by water. For a spin-coated surface of 20 wt% fluorodecyl POSS + x-PEGDA previously

wet by water, using equation 2.3 and noting that rapeseed oil shows a contact angle of θ_{oil} = 45º (figure 2.6a), we obtain γ_{sv}^{d} = 26 mN/m. Similarly, using equation 2.4 and noting that water exhibits a contact angle of θ_{water} = 0º, we obtain γ_{sv}^{p} = 46.5 mN/m. Thus, γ_{sv} = 72.5 mN/m. If the surface were assumed to be completely dry, a Young's contact angle θ_{oil} = 45º corresponds to a surface with ~ 1.5 wt% fluorodecyl POSS + x-PEGDA blend (see Table 2.1). However, a completely dry surface is unlikely immediately after surface reconfiguration. This is evident from a higher value of γ_{sv}^{p} = 46.5 mN/m for the reconfigured surface, compared to γ_{sv}^{p} = 39.5 mN/m for neat x-PEGDA. On the other hand, if the surface were assumed to be completely wet by water, γ_{sv} = 72.5 mN/m corresponds to a surface with ~ 0.4 wt% fluorodecyl POSS + x-PEGDA blend (see Table 2.1). Based on this analysis, we estimate that after reconfiguration, the surface is equivalent to an x-PEGDA blend with ~ 0.4−1.5wt% fluorodecyl POSS.

2.3.4. Time of wetting

Addition of fluorodecyl POSS causes a systematic increase in the time required for surface reconfiguration, as is evident from the increased time of wetting (ToW) for water on spin-coated fluorodecyl POSS + x-PEGDA surfaces (figure 2.7a). This is likely due to a reduction in the initial interfacial area between PEGDA chains and the contacting water droplet with increasing fluorodecyl POSS concentration. We define ToW as the time required for the water contact angle on a surface to decrease from its initial value to 0°. We also measured ToW for water on the porous mesh and fabric membranes (figure 2.7b). On these surfaces, we define ToW as the time required for the water droplet to imbibe into the membrane. Membrane imbibition is not instantaneous for

surfaces with reconfigurable chemistry. Rather, the water–air interface progressively penetrates into the surface texture and water permeates through the membrane once the robustness factor $A^*_{water} \leq 1$. (If the liquid does not permeate through the membrane pores, the solid–liquid–air composite interface equilibrates at a location on the membrane where the local texture angle (ψ) is equal to the Young's contact angle, θ.) From equation 1.5, for mesh 100 $A^*_{water} = 1$ when $\theta_{water} = 18°$. Our ToW measurements on the dip-coated meshes match closely with the time required for $\theta_{water,adv}$ to decrease from its initial value to 18° (figure 2.7b).

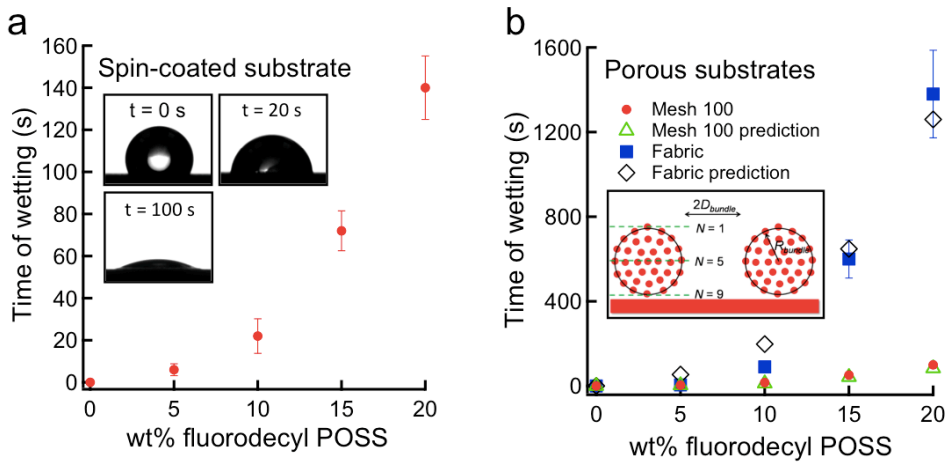

Figure 2.7 Time of wetting (ToW). (a) and (b) ToW of water for spin-coated (a) and porous (b) substrates. Insets in (a) sho the time-dependent decrease in contact angle for a water droplet. Inset in (b) is a schematic illustrating the two scales of texture (bundles and individual fibers) for the fabric. The ToW predictions for mesh 100 and fabric membranes closely match experimental measurements, as shown in (b).

The ToW for water on the dip-coated fabrics was found to be considerably higher than ToW on the meshes. This is because water has to progressively wet multiple fibers during imbibition. The fabrics used in this work have interwoven bundles of fibers (figure

2.2b, inset). Each bundle contains several layers of smaller individual fibers that offer an additional length scale for air entrapment (figure 2.7b, inset). From equation 1.5, for water on an individual fiber (R_{fiber} = 5 μm, D_{fiber} = 20 μm), A^{*}_{water} = 1 when θ_{water} = 7º. Thus, the ToW for water on each layer of the fibers should be the equal to the time taken for $\theta_{water,adv}$ to reach 7º, which is approximately equal to the ToW for water on spin-coated substrates. Assuming N-layers of individual fibers, the ToW for water on the fabric surface should be N times the ToW for water on the spin-coated surface. Fitting the experimental data with this N-layer model yields a best fit for N = 9, which appears to be a reasonable estimate, based on figure 2.2b, inset.

2.3.5. Batch separation of oil-water mixtures

Very few reports on membrane separation[27-29] and microfluidics[30,31] have used the difference in capillary forces acting on the individual phases as the primary mechanism to separate emulsions or dispersions. We call this methodology capillary force-based separation (CFS). In CFS, the wetting phase permeates through the membrane, while the non-wetting phase is retained. From equation 1.5, the breakthrough pressure required to force the non-wetting phase through a membrane already saturated by the wetting phase is

(Equation 2.5) $$P_{\text{breakthrough}} = \frac{2R\gamma_{12}}{D^2}\frac{1-\cos(\theta')}{1+2(R/D)\sin(\theta')}$$

Here γ_{12} is the interfacial tension between the wetting phase and the non-wetting phase, and θ is the contact angle of the non-wetting phase on the solid surface, both of which are completely immersed in the wetting phase. When pressure $P_{applied} < P_{breakthrough}$ is applied, only the wetting phase permeates through the membrane. We use CFS in this

work because it combines both demulsification and separation into a single-unit operation, it provides a very high-quality permeate and it is inherently self-repairing[31]. For a CFS–based system to work effectively, it is necessary that the wetting phase contact the membrane. There are several techniques to achieve this goal: gravity-driven (if the wetting phase has a higher density than the non-wetting phase), electrostatic[32] (if the wetting phase is a polar liquid), forced convection[4,7,12], etc. Here we demonstrate separation of various oil-water mixtures utilizing solely gravity.

2.3.5.1. Separation of free oil and water

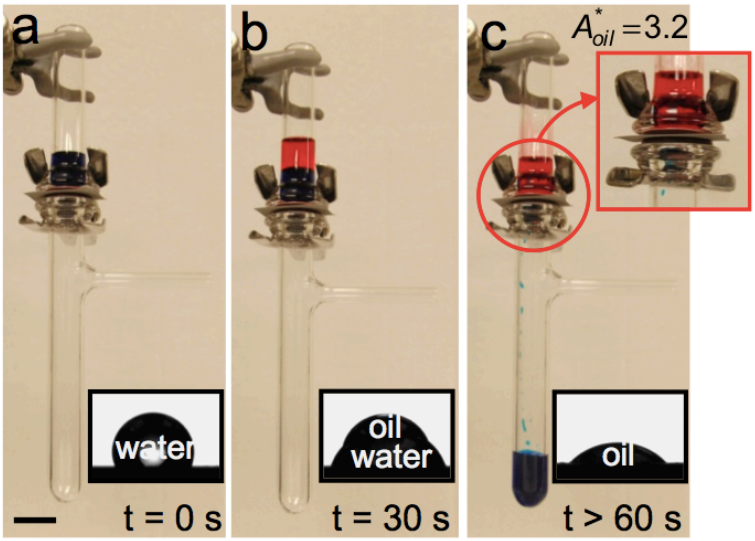

Figure 2.8 Batch separation of free oil and water. (a) Separation apparatus with water above the membrane. (b) Rapeseed oil is added above water. (c) Water permeates through the membrane whereas rapeseed oil is retained. Inset, water droplet on a surface spin-coated with a 20 wt% fluorodecyl POSS + x-PEGDA blend, rapeseed oil droplet on top of the water droplet, rapeseed oil droplet on the reconfigured surface.

Figures 2.8a-c show the solely gravity-driven CFS of free rapeseed oil and water using a mesh 100 ($2D$ = 138 μm) coated with a 20 wt% fluorodecyl POSS + x-PEGDA blend. Water is added to the upper tube (figure 2.8a) immediately followed by rapeseed

oil (figure 2.8b). The corresponding insets in figures 2.8a and 2.8b show a drop of water placed on a spin-coated surface of 20 wt% fluorodecyl POSS + x-PEGDA, and a drop of rapeseed oil immediately placed on top of the drop of water, respectively. Upon surface reconfiguration, water permeates through the membrane, while rapeseed oil is retained above the membrane (figure 2.8c). On a spin-coated 20 wt% fluorodecyl POSS + x-PEGDA surface, previously wet by water, a drop of rapeseed oil displays a contact angle of $\theta_{oil,adv}$ = 45º (figure 2.8c, inset). Thus, for rapeseed oil on the membrane, the robustness factor A^*_{oil} = 3.2. Consequently, rapeseed oil is retained above the membrane. Water permeates through the membrane at $A^*_{water} \approx 1.2$.

The experimentally measured flux of water through the membrane (mesh 100; $2D$ = 138 μm), $Q_{\text{water}} \approx$ 43,200 L/m^2-h. This is significantly lower than the flux of the water ($\mu \sim$ 1 mPa-s), Q_{water} = 509,000 L/m^2-h, predicted using the Hagen-Poiseuille relation[33]. This is because the number of pores through which water is flowing at any given time (so called "active pores") in CFS can be significantly lower (~1–10%) than the actual number of pores[30]. Comparing the measured and the predicted fluxes, we estimate that ~ 8.5% of the total pores are active during the separation of free oil and water.

2.3.5.2. Separation of oil-in-water emulsions

Figure 2.9a shows representative optical image of the hexadecane-in-water emulsion (50 vol% hexadecane) stabilized using sodium dodecyl sulphate (SDS; hydrophilic–lipophilic balance, HLB = 40). We determined the size distributions of the dispersed phase in feed emulsions and permeates using two techniques – optical microscopy image analysis for droplets above 1 μm in diameter and dynamic light

scattering (DLS) for droplets below 1 μm. Figure 2.9b shows the number size distributions of the dispersed phase in hexadecane-in-water feed emulsions determined using image analysis. The average size of dispersed phase in the feed emulsions is between 10−20 μm. Figure 2.9c shows the number size distributions of the dispersed phase in hexadecane-in-water feed emulsions, determined using DLS. The size of dispersed phase in the feed emulsions varies between 100−500 nm.

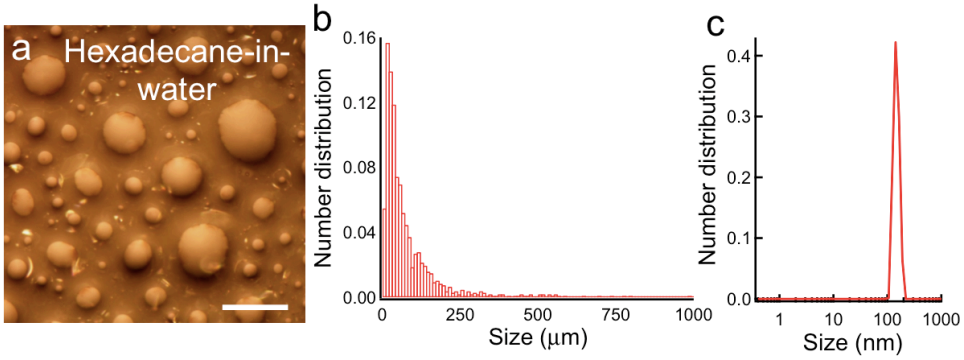

Figure 2.9 Size distributions of hexadecane droplets in the hexadecane-in-water feed emulsion. (a) A representative optical microscopy image of 50:50 v:v hexadecane-in-water feed emulsion. Scale bar, 500 μm. (b) and (c) The number size distributions for the hexadecane-in-water feed emulsion fro droplets > 1 μm and < 1 μm, respectively.

Figures 2.10a and 10b show solely gravity-driven CFS of a hexadecane-in-water emulsion (50 vol% hexadecane). The separation apparatus consists of a mesh 400 ($2D$ = 37.5 μm), dip-coated with a 20 wt% fluorodecyl POSS + x-PEGDA blend and sandwiched between two vertical glass tubes. We used the superhydrophilic and oleophobic meshes as they are available in a range of different pore sizes, allowing us to systematically vary the membrane porosity. Our superhydrophilic and superoleophobic fabrics show a similar performance. The emulsion is added to the upper tube (figure

2.10a). Once water in the emulsion contacts the membrane, the surface starts to reconfigure. Within minutes, the water-rich permeate passes through the membrane while the hexadecane-rich retentate is retained above the membrane (figure 2.10b). Membrane oleophobicity under water is critical for the separation of hexadecane-in-water emulsions (figure 2.10a, inset).

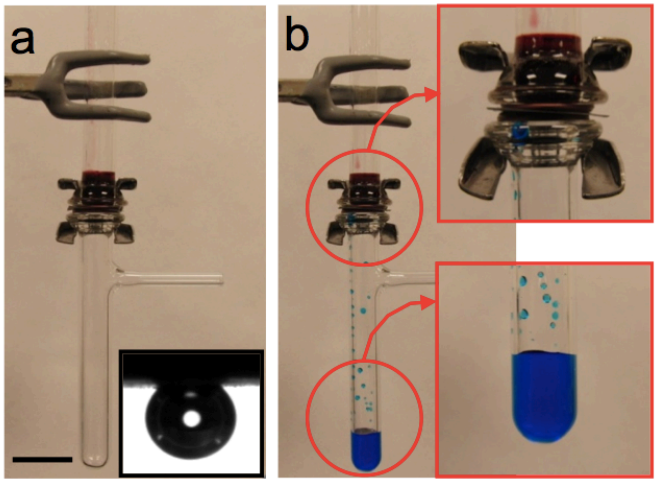

Figure 2.10 Batch separation of oil-in-water emulsion. (a) Separation apparatus with a 50:50 v:v hexadecane-in-water emulsion above the membrane. Inset, hexadecane droplet on a surface spin-coated with a 20 wt% fluorodecyl POSS + x-PEGDA blend, submerged in water containing dissolved SDS (1 mg/ml). (b) Water-rich permeate passes through the membrane whereas hexadecane-rich retentate is retained. Water is dyed blue and hexadecane is dyed red. Scale bar, 2 cm.

Figures 2.11a and 11b show the number size distributions of the permeates obtained from separation of hexadecane-in-water emulsion using mesh 400 ($2D$ = 37.5 μm) and mesh 500 ($2D$ = 30.5 μm), respectively. These were determined using image analysis. The average size of the dispersed phase in both permeates is 10−20 μm. Comparing hexadecane-in-water feed emulsion with the permeates, it is evident that nearly all hexadecane droplets above 40 μm were removed during separation. Figures

2.11c and 11d show the number size distributions of the permeates obtained from the separation of the hexadecane-in-water emulsion using mesh 400 and mesh 500, respectively. These were determined using DLS. The average size of dispersed phase in both the permeates is approximately 100 nm. Comparing the hexadecane-in-water feed emulsion with the permeates, it is evident that the droplet distribution below 1 μm remains unchanged during separation.

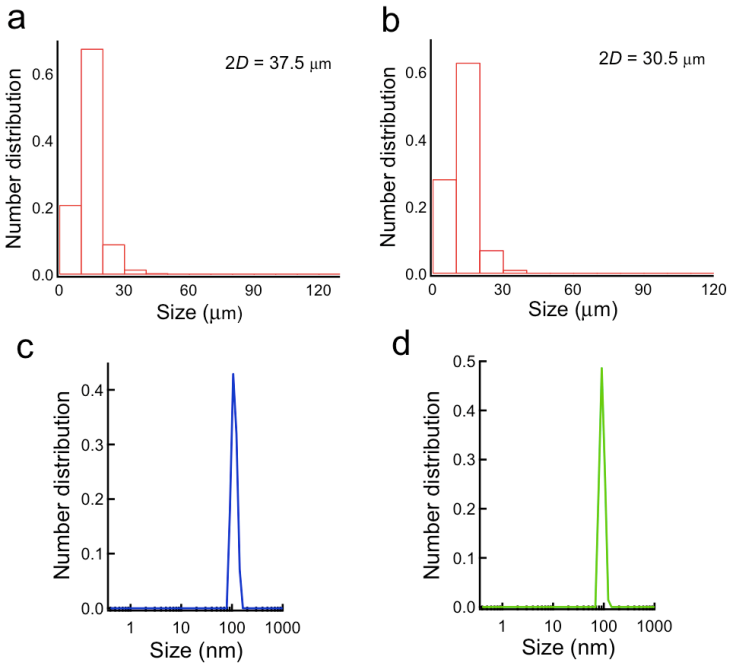

Figure 2.11 Size distributions of dispersed phase in permeates. (a) and (b) The number size distributions of the permeate from the separation of 50:50 v:v hexadecane-in-water emulsion using mesh 400 and mesh 500, respectively, obtained with optical image analysis. (c) and (d) The number size distributions of the permeate from the separation of 50:50 v:v hexadecane-in-water emulsion using mesh 400 and mesh 500, respectively, obtained with DLS.

Thermogravimetric analyses (TGA; figure 2.12a) indicate that the water-rich permeate contains ~ 0.1 wt% hexadecane, whereas the hexadecane-rich retentate contains

~ 0.1 wt% water. In addition to using TGA, we conducted transmittance measurements in order to estimate the permeate (water-rich phase) quality in batch separation relative to the feed emulsions. Figure 2.12b shows the transmittance of 50:50 v:v hexadecane-in-water (absorbance normalized to 1), transmittance of the corresponding permeate, and transmittance of pure water between 390 nm and 750 nm (visible spectrum). It is evident that both the feed emulsions are very turbid, while the corresponding permeate are very clear. This indicates that CFS used here leads to nearly complete separation. We also estimated the degree of separation by comparing the density of the permeates with density calibration curves (figure 2.12c). We developed the calibration curves by measuring the densities of hexadecane-water mixtures with different hexadecane compositions (0 wt%, 1 wt% and 2 wt%). We measured the density of the permeate from separation of the 50:50 v:v hexadecane-in-water emulsions to be 1.004±0.003 g/cm^3. Comparing them with the calibration curves indicates that the permeate have significantly < 1 wt% hexadecane, confirming the separation efficiency for the CFS processes to be > 99%. Additional experiments showed that we can similarly separate, with > 99% efficiency, hexadecane-in-water emulsions containing 10 vol% and 30 vol% hexadecane. We also conducted experiments with hexadecane-in-water emulsions containing salt (sodium chloride). As with the non-saline emulsions, we could separate saline emulsions with > 99% efficiency.

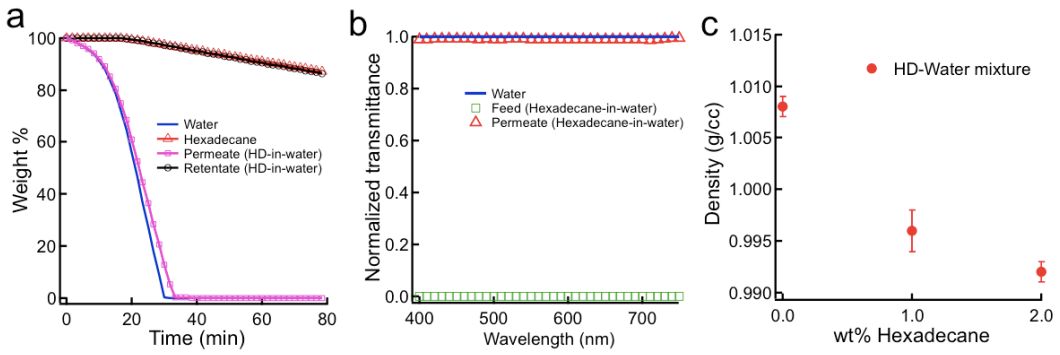

Figure 2.12 TGA, Transmittance and density measurements. (a) TGA data for the permeate and retentate. HD, hexadecane. (b) Transmittance of 50:50 v:v hexadecane-in-water feed emulsion and the permeate. (c) Density of hexadecane-in-water mixtures as a function of hexadecane (HD) composition.

2.3.5.3. Separation of water-in-oil emulsions

Figure 2.13a shows representative optical image of the water-in-hexadecane emulsion (30 vol% water) stabilized using Polysorbate80 (PS80; HLB = 15). Figure 2.13b shows the number size distributions of the dispersed phase in hexadecane-in-water feed emulsions determined using image analysis. The average size of dispersed phase in the feed emulsions is between 10−20 μm. Figure 2.13c shows the number size distributions of the dispersed phase in water-in-hexadecane feed emulsions, determined using DLS. The size of dispersed phase in both the feed emulsions varies between 100−500 nm.

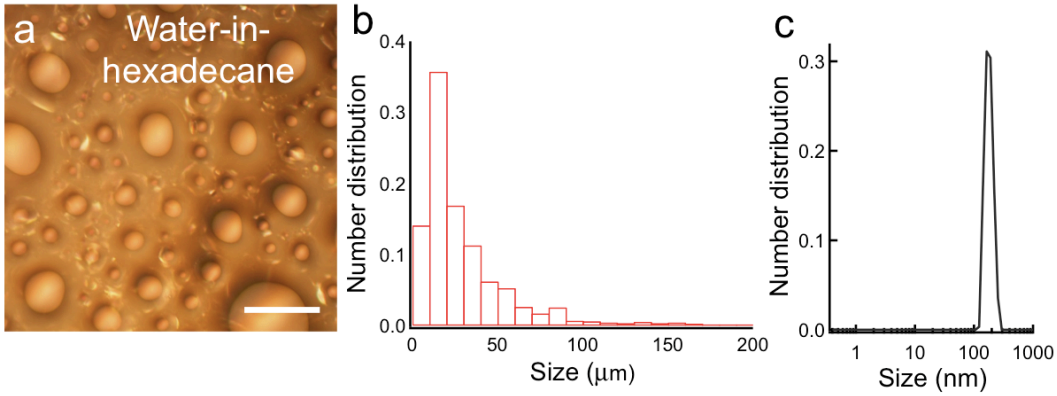

Figure 2.13 Size distributions of water droplets in the water-in-hexadecane feed emulsion. (a) A representative optical microscopy image of 30:70 v:v water-in-hexadecane feed emulsion. Scale bar, 200 µm. (b) and (c) The number size distributions for the water-in-hexadecane feed emulsion fro droplets > 1 µm and < 1 µm, respectively.

Figures 2.14a and 14b show the solely gravity-driven CFS of a water-in-oil emulsion (30 vol% water) stabilized using PS80. The apparatus is the same as that used for the separation of oil-in-water emulsions. The emulsion is added to the upper tube (figure 2.14a). Once water droplets within the emulsion contact the membrane, the surface starts to reconfigure. Before the breakthrough of the water-rich permeate, hexadecane is retained above the membrane because of membrane oleophobicity in air. After surface reconfiguration, the water-rich permeate passes through the membrane while the hexadecane-rich retentate is retained above the membrane (figure 2.14b). During the permeation of the water-rich permeate, the hexadecane-rich retentate is retained above the membrane because of membrane oleophobicity under water. Membrane oleophobicity, both in air and under water, is critical for separating water-in-hexadecane emulsions.

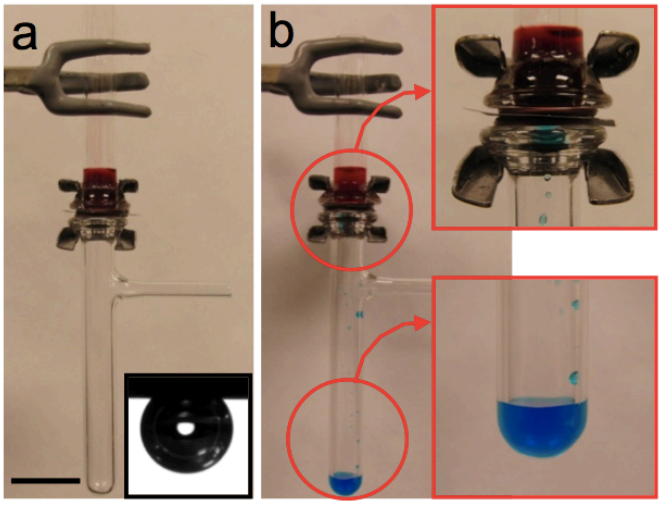

Figure 2.14 Batch separation of water-in-oil emulsion. (a) Apparatus with a 30:70 v:v water-in-hexadecane emulsion above the membrane. Inset, hexadecane droplet on a surface spin-coated with a 20 wt% fluorodecyl POSS + x-PEGDA blend, submerged in water containing dissolved PS80 (1 mg/ml). (b) Water-rich permeate passes through the membrane whereas hexadecane-rich retentate is retained. Water is dyed blue and hexadecane is dyed red. Scale bar, 2 cm.

TGA (figure 2.15a) and transmittance (figure 2.15b) measurements indicate that the permeate contains ~ 0.1 wt% hexadecane, whereas the retentate contains ~ 0.1 wt% water. We measured the density of the permeate to be 1.006±0.004 g/cm^3. Comparing them with the calibration curves (see figure 2.12c) indicates that the permeate have significantly < 1 wt% hexadecane, confirming the separation efficiency for the CFS processes to be > 99%. Additional experiments showed that we can similarly separate, with > 99% efficiency, water-in-hexadecane emulsions containing 10 vol% and 20 vol% water. Further, we can also similarly separate span80 (HLB = 4.3) stabilized water-in-hexadecane emulsions containing 10 vol%, 20 vol% and 30 vol% water, with > 99% efficiency.

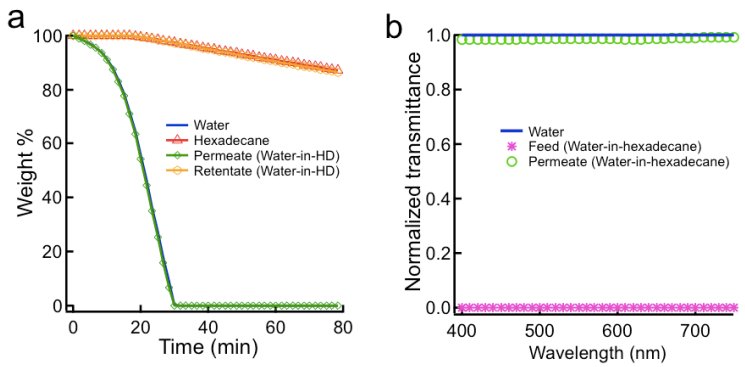

Figure 2.15 TGA and transmittance measurements. (a) TGA data for the permeate and retentate. HD, hexadecane. (b) Transmittance of 30:70 v:v water-in- hexadecane feed emulsion and the permeate.

2.3.5.4. Separation of four-component mixtures

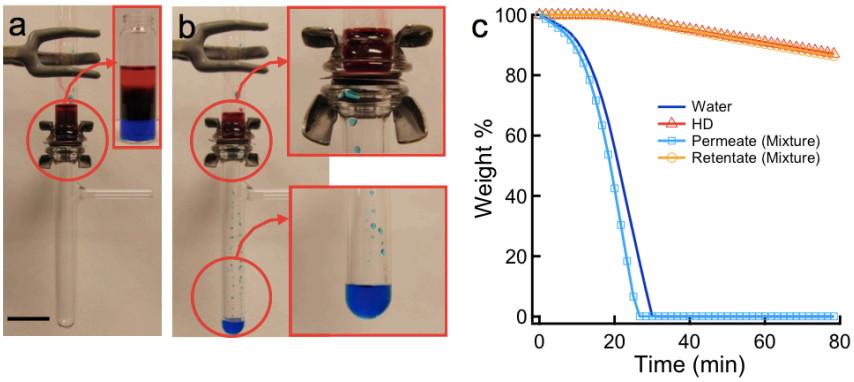

Figure 2.16 Batch separation of four component mixtures. (a) Apparatus with four-component mixture above the membrane. Inset, larger quantity of the feed in a glass vial, depicting the presence of different phases. (b) Water-rich permeate passes through the membrane whereas hexadecane-rich retentate is retained. Water is dyed blue and hexadecane is dyed red. Scale bar, 2cm. (c) TGA data for the permeate and retentate. HD, hexadecane.

Figures 2.16a and 16b show the separation of a mixture containing four components: water, hexadecane, water-in-hexadecane emulsion and hexadecane-in-water

emulsion. Again, mesh 400 dip-coated with a 20 wt% fluorodecyl POSS + x-PEGDA blend separated this mixture into highly pure constituents, that is, a permeate containing ~ 0.1 wt% hexadecane and a retentate containing ~ 0.1 wt% water, as confirmed by TGA (figure 2.16c).

2.3.6. Estimation of hexadecane-water interfacial tension in the presence of surfactants

We estimated hexadecane-water interfacial tension γ_{ow} in the presence of surfactants by using the relationship postulated by previous work[23]:

(Equation 2.6) $\gamma_{ow} = \gamma_{ov} + \gamma_{wv} - 2\sqrt{\gamma_{ov}^{d}\gamma_{wv}^{d}}$

Note that here we use γ_{ow} to refer to hexadecane-water interfacial tension. γ_{ov} and γ_{wv} are the surface tensions, and γ_{ov}^{d} and γ_{wv}^{d} are the dispersive components of the surface tensions of hexadecane and water, respectively, in the presence of surfactants. Recognizing that $\gamma_{ov} = \gamma_{ov}^{d}$ for hexadecane (non-polar liquid), three unknown parameters (i.e., γ_{ov}, γ_{wv} and γ_{wv}^{d}) are required to determine γ_{ow}. We used three different experiments to estimate these three parameters:

(i) *Estimation of surface tension of hexadecane* (γ_{ov}) *with surfactants:*

We used the capillary rise method to estimate γ_{ov}. According to this method:

(Equation 2.7) $\gamma_{ov} = \dfrac{\rho_{oil} g r h_{oil}}{2\cos\theta_{oil}}$

Here, ρ_{oil} = 0.77 g/ml is the density of hexadecane, g = 9.81 m/s^2 is the acceleration due to gravity, and r = 200 μm is the radius of the glass capillary used. We measured the capillary rise of hexadecane, h_{oil} = 2.9 cm and h_{oil} = 3.3 cm, with SDS and PS80, respectively. The contact angle of hexadecane on glass was measured to be θ_{oil} = 0° with

both surfactants. Using these values in equation 2.7, we determined γ_{ov} = 21.9 mN/m and γ_{ov} = 24.9 mN/m with SDS and PS80, respectively.

(ii) *Estimation of surface tension of water* (γ_{wv}) *with surfactants:*

We used the capillary rise method to estimate γ_{wv} as well. According to this method:

(Equation 2.8) $\gamma_{wv} = \frac{\rho_{water} g r h_{water}}{2\cos\theta_{water}}$

Here, ρ_{water} = 1.0 g/ml is the density of water, g = 9.81 m/s^2 is the acceleration due to gravity, and r = 200 μm is the radius of the glass capillary used. We measured the capillary rise of water, h_{water} = 4.5 cm and h_{water} = 4.6 cm, and the contact angle of water on glass, θ_{water} = 0° with SDS and θ_{water} = 0° with PS80. Using these values in equation 2.8, we determined γ_{wv} = 44.1 mN/m and γ_{wv} = 45.1 mN/m with SDS and PS80, respectively.

(iii) *Estimation of the dispersive component of water surface tension* (γ_{wv}^d) *with surfactants*

The solid-water interfacial tension for a non-polar solid such as 50 wt% fluorodecyl POSS + Tecnoflon is given as:

(Equation 2.9) $\gamma_{sw} = \gamma_{sv} + \gamma_{wv} - 2\sqrt{\gamma_{sv}^d \gamma_{wv}^d}$

Here, γ_{sv} = 9.9 mN/m is the solid surface energy (see Table 2.1), γ_{wv} is the surface tension of water with surfactants, γ_{sv}^d = 9.6 mN/m is the dispersive component of the solid surface energy (see Table 2.1) and γ_{wv}^d is the dispersive component of the surface tension of water with surfactants. The 50 wt% fluorodecyl POSS + Tecnoflon blend was chosen because it is nearly completely non-polar and does not reconfigure when in contact with

water or hexadecane. Combining equation 2.9 with Young's equation (equation 1.1), we obtain:

(Equation 2.10) $\gamma_{wv}^{d} = \frac{\left[\gamma_{wv}(1+\cos\theta)\right]^2}{4\gamma_{sv}^{d}}$

On a spin-coated surface of 50 wt% fluorodecyl POSS + Tecnoflon, we measured the contact angles of water θ_{water} = 94° and θ_{water} = 95° with 0.5 mg/ml of SDS and 0.3 mg/ml of PS80, respectively. Using these values and the previously estimated values of γ_{wv} in equation 2.10, we determined γ_{wv}^{d} = 43.8 mN/m and γ_{wv}^{d} = 44.1 mN/m with SDS and PS80, respectively.

Using the values estimated from the above three experiments in equation 2.6, we determined γ_{ow} = 4.0 mN/m and γ_{ow} = 3.7 mN/m with SDS and PS80, respectively. As may be expected, these values are significantly lower than the hexadecane-water interfacial tension (γ_{ow} = 51.4 mN/m) in the absence of surfactants.

2.3.7. Breakthrough height

For the separation apparatus used in the batch separation, the maximum height of the liquid column before the oil phase permeates through the membrane ($h_{breakthrough}$) can be obtained using equation 1.5 when the membrane is in air or equation 2.5 when the membrane is submerged under water. Note that $P_{breakthrough} = \rho g h_{breakthrough}$. For free oil and water separation, $\theta_{oil,adv}$ = 45°, γ_{lv} = 35.7 mN/m and $h_{breakthrough}$ is predicted to be 1.3 cm ($P_{breakthrough}$ = 117 Pa) using equation 1.5. For the SDS stabilized 50:50 v:v hexadecane-in-water emulsion, $\theta_{oil,adv}$ = 120° (figure 2.10a, inset), $\gamma_{1,2}$ = 4.0 mN/m and $h_{breakthrough}$ is predicted to be 2.3 cm ($P_{breakthrough}$ = 198 Pa) using equation 2.5. For water-in-oil emulsions, $h_{breakthrough}$ should be predicted using equation 1.5 before the

breakthrough of the water-rich permeate and using equation 2.5 during the permeation of the water-rich permeate. The lower value of the two predicted breakthrough heights limits the operating height. For the PS80 stabilized 30:70 v:v water-in-hexadecane emulsion, before the breakthrough of the water-rich permeate, $\theta_{oil,adv}$ = 70°, γ_{lv} = 24.9 mN/m and $h_{breakthrough}$ is predicted to be 6.3 cm ($P_{breakthrough}$ = 519 Pa) using equation 1.5. For the same emulsion, during the permeation of the water-rich permeate, $\theta_{oil,adv}$ = 125° (figure 2.14a, inset), $\gamma_{1,2}$ = 3.7 mN/m and $h_{breakthrough}$ is predicted to be 2.4 cm ($P_{breakthrough}$ = 198 Pa). Consequently, the operating height during the water-in-hexadecane emulsion separation is limited by $h_{breakthrough}$ during the permeation of the water-rich permeate. Indeed, these predicted values of $h_{breakthrough}$ closely match experimentally measured values of 1.3 cm, 2 cm and 2.2 cm for the free oil and water, hexadecane-in-water emulsion and water-in-hexadecane emulsion separation, respectively. In order to ensure CFS, we used an operating height $h < h_{breakthrough}$ in all our separation operations.

2.3.8. Continuous separation of oil-water emulsion

In the batch separation apparatus design, oil accumulates above the membrane over time and will eventually break through once the operating height > $h_{breakthrough}$. Therefore, we developed a continuous oil–water separation apparatus (figure 2.17a), with two CFS-based operations in parallel, using a superhydrophilic and oleophobic membrane at the bottom and a hydrophobic and oleophilic membrane on the side wall. The feed emulsion is fed into the glass tube at a constant rate using a syringe pump. Water (dyed blue) permeates through the superhydrophilic and oleophobic membrane at the bottom, while hexadecane (dyed red) permeates through the hydrophobic and

oleophilic membrane on the side-wall. Using this apparatus, we achieved continuous, solely gravity-driven CFS of oil–water emulsions.

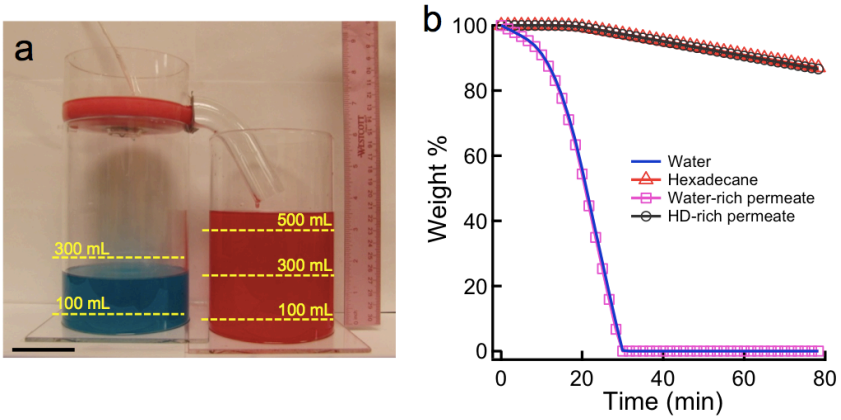

Figure 2.17 Continuous separation of water-in-oil emulsion. (a) A scaled-up apparatus used for the continuous separation of 30:70 v:v water-in-hexadecane emulsions stabilized by PS80. During continuous separation, water-rich permeate continuously passes through the superhydrophilic and oleophobic membrane at the bottom, whereas hexadecane-rich permeate continuously passes through the hydrophobic and oleophilic membrane on the side-wall. Water is dyed blue and hexadecane is dyed red. Scale bar, 5 cm. (b) TGA data for both the permeates. HD, hexadecane.

TGA (figure 2.17b) indicates that the water-rich permeate contains ~ 0.1 wt% hexadecane and that the hexadecane-rich permeate contains ~ 0.1 wt% water, which is the limit of detection using TGA. Karl Fischer analysis[34] indicates that the hexadecane-rich permeate contains ~25 ± 8 ppm. water (i.e., ~ 0.0025 wt% water). Note that the as-obtained hexadecane contains ~20 ± 5 ppm. water. Further, the solubility of water in hexadecane at room temperature is between ~20-50 ppm[35,36]. This indicates that we are removing nearly all of emulsified water droplets during the operation.

We computed the fraction of emulsified water droplets removed from water-in-hexadecane emulsions during the separation. 100 ml of 30:70 v:v water-in-hexadecane

feed emulsion contains 30 ml of water and 70 ml of hexadecane. We determined the volume fraction of emulsified water droplets (< 20 μm) in our feed emulsions to be 0.018 from the volume size distribution (figure 2.18). Thus, the volume of emulsified water droplets in 100 ml of feed emulsion is 0.54 ml. In continuous separation, 100 ml of feed emulsion results in approximately 30 ml of water-rich permeate and 70 ml of hexadecane-rich permeate. Karl Fischer analysis indicates that the amount of water in the hexadecane-rich permeate is ~ 0.0025 wt%, which is equivalent to ~ 0.0019 vol%. Thus, the volume of water in the hexadecane-rich permeate is 0.0013 ml. Even if we assume that the size of all the water droplets in the hexadecane-rich permeate is < 20 μm, comparing the volume of the emulsified water droplets in the feed emulsion (0.54 ml) to that in the hexadecane-rich permeate (0.0013 ml), we conclude that the volumetric fraction of emulsified droplets removed during separation is at least 99.8%. Thus, it is clear that the membrane allows for the removal of dispersed-phase droplets that are considerably smaller than the membrane pore size ($2D$ = 37.5 μm).

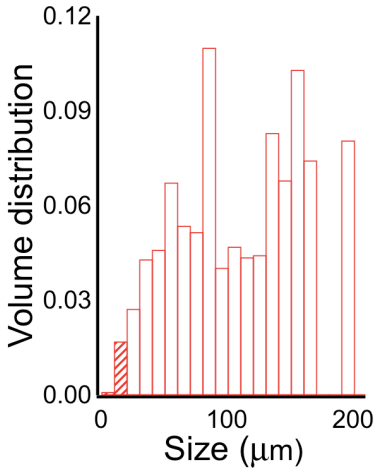

Figure 2.18 Volume size distribution. Volume size distribution of water droplets for the 30:70 v:v water-in-hexadecane feed emulsion. The dashed region represents droplets below 20 μm (emulsified droplets).

2.3.9. Location and concentration of surfactant after separation

We estimated the amount of surfactant in the permeates after emulsion separation by measuring their contact angles and comparing them with calibration curves of contact angles of water and hexadecane as a function of surfactant concentration. The calibration curves were developed by measuring the contact angles on flat surfaces spin-coated with a 50 wt% fluorodecyl POSS + Tecnoflon blend. The 50 wt% fluorodecyl POSS + Tecnoflon blend was chosen because it is nearly completely non-polar (see Table 2.1) and it does not reconfigure when in contact with water or hexadecane. Figures 2.19a and 19b show the advancing and receding contact angles of water as a function of SDS and PS80 concentration. Figure 2.19c shows the advancing and receding contact angles of hexadecane as a function of PS80 concentration. As SDS is nearly insoluble in hexadecane, we could not obtain the corresponding calibration curve.

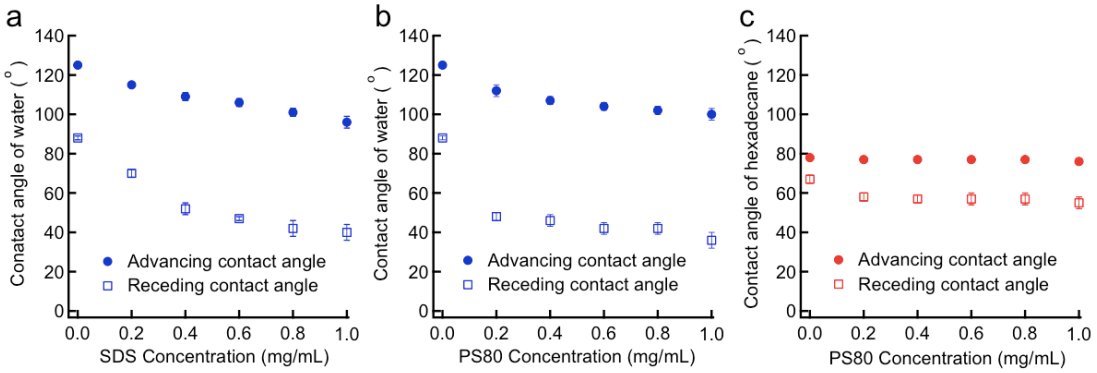

Figure 2.19 Location and concentration of surfactant after emulsion separation. (a) and (b) Advancing and receding contact angles of water as a function of SDS concentration and PS80 concentration, respectively. (c) Advancing and receding contact angles of hexadecane as a function of PS80 concentration.

Consider the permeate (~ 99.9% water) from batch separation of SDS stabilized hexadecane-in-water emulsion. The advancing and receding contact angles of the permeate from hexadecane-in-water emulsion separation are 94°±2° and 39°±4°. By comparing these contact angles with figure 2.19a, it is evident that the concentration of SDS in the permeate is approximately 1 mg/ml. In other words, after separation, nearly all the surfactant is in the permeate. This is likely due to the fact that SDS is virtually insoluble in hexadecane.

Now consider the two permeates (~ 99.9% water) from continuous separation of PS80 stabilized water-in-hexadecane emulsion. The advancing and receding contact angles of the water-rich permeate through the hydrophilic and oleophobic membrane are 98°±2° and 38°±4°, while those of the hexadecane-rich permeate through the hydrophobic and oleophilic membrane are 76°±2° and 56°±4°. By comparing these contact angles with figures 2.19b and 19c, it is evident that the concentration of PS80 in the permeate through the hydrophilic and oleophobic membrane is between 0.8-1 mg/ml, while the concentration of PS80 in the permeate through the hydrophobic and oleophilic membrane is between 0-0.2 mg/ml.

2.3.10. Prediction of permeates fluxes during continuous separation of water-in-hexadecane emulsions

Fluxes of water-rich and hexadecane-rich permeates through the membranes were measured to be 90 and 210 L/m^2-h, respectively. These values are comparable to those reported in previous work on membrane separation under externally applied pressures[4,5,7,12,37,38]. Furthermore, in intermittent stop-and-go operation, the fluxes did not decrease over a period of 100 hr (see figure 2.20 and Table 2.2), indicating that the

membranes are highly resistant to fouling by oil. Membrane wettability, and the considerably larger pore sizes of the membranes used here, compared with those used traditionally[4,6,8,12], are expected to be two major contributing factors towards the observed resistance to fouling.

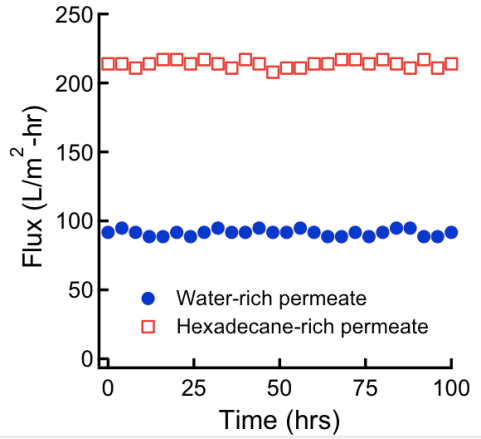

Figure 2.20 Measured fluxes for both the permeates as a function of time.

We seek to predict the flux of water-rich permeate through the superhydrophilic and oleophobic mesh 400 and the flux of hexadecane-rich permeate through the hydrophobic and oleophilic mesh 400 used in the continuous separation of 30:70 v:v water-in-hexadecane emulsions. In this analysis, we assume that the water-rich permeate (≤ 0.1 wt% hexadecane) and the hexadecane-rich permeate (≤ 0.1 wt% water) have the same fluid flow characteristics as those of pure water and pure hexadecane, respectively.

Consider the flow of water-rich permeate through the superhydrophilic and oleophobic membrane. For a 30:70 v:v water-in-hexadecane emulsion column of height 1.2 cm above mesh 400 (R = 12.5 μm, $2D$ = 37.5 μm), the flux of water-rich permeate (μ = 1 mPa-s) predicted using the Hagen-Poiseuille relation[33] is 88,400 L/m^2-h. This is

three orders of magnitude higher than the experimentally measured flux of 90 L/m^2-h (see figure 2.20 and Table 2.2). Such a large discrepancy arises from the assumption that the water droplets (dispersed phase) are constantly in contact with the membrane, so that they may readily permeate through, without any discontinuity. In reality, a majority of the dispersed water droplets are not in physical contact with the membrane. Each dispersed water droplet must settle (or sediment) under gravity, reach the membrane, wet the membrane and permeate through. The rate of sedimentation decreases rapidly as the size of the dispersed water droplets decreases. Consequently, the flux for the water-rich permeate is limited by the rate of sedimentation of water droplets. In previous work[39], a comprehensive analysis on the sedimentation velocity v_d of droplets in dispersions was conducted to arrive at equations 2.11-14 and validated them through extensive sets of experiments. They suggest:

(Equation 2.11) $v_{\mathrm{d}} = v_{\mathrm{r}}\left(1-\alpha_{\mathrm{d}}\right)$

(Equation 2.12) $v_r^2 = \frac{8}{3}\frac{r_d}{C_D\rho_c}(\rho_d - \rho_c)$

(Equation 2.13) $C_{\mathrm{D}} = \frac{24}{\mathrm{Re}}$

(Equation 2.14) $\mathrm{Re} = \frac{2r_d\rho_c v_r}{\mu_m}$

Here, v_{r} is the relative velocity between the dispersed and the continuous phases, r_{d} is the radius of the dispersed phase droplets, C_{D} is the drag coefficient, r_{c} and r_{d} are the densities of the continuous and the dispersed phase, a_{d} is the volume fraction of the dispersed phase, and μ_{m} is the effective viscosity of the mixture. For the 30:70 v:v water-in-hexadecane emulsion used in this work, r_{c} = 0.77 g/cm^3, r_{d} = 1 g/cm^3, a_{d} = 0.3 and μ_{m} = 2.5 mPa-s. We calculate the mean volumetric radius r_{d} of the water droplet as:

(Equation 2.15) $V_{mean} = \frac{4}{3}\pi r_d^3$

where the mean volume V_{mean} is given by:

(Equation 2.16) $V_{mean} = \sum x_i V_i$

Here x_i and V_i refer to the number fraction and volume, respectively, of water droplets with diameter d_i. From the number distribution shown in figure 2.13b, we obtain r_d = 28 μm. Using equations 2.11-14, we predict the average sedimentation velocity of water droplets to be v_d = 77 μm/s, which leads to a water-rich permeate flux of 83 L/m^2-h through the superhydrophilic and oleophobic mesh 400. This value is in reasonable agreement with the experimentally measured flux of 90 L/m^2-h. As the sedimentation velocity is proportional to square of the droplet radius (combining equations 2.12-15), the flux of water-rich permeate will be impractically low (< 1 L/m^2-h) for fine emulsions with droplet diameter less than 5 μm. In such cases, other techniques such as electrostatic coalescence (if the wetting phase is a polar liquid)[32], or forced convection[4], may be useful.

Now, consider the flow of hexadecane-rich permeate through the hydrophobic and oleophilic membrane. Since we conducted continuous separation at steady state with a feed flux of 300 L/m^2-h, material balance for a 30:70 v:v water-in-hexadecane emulsion yields a hexadecane-rich permeate flux of 217 L/m^2-h. This predicted flux is in reasonable agreement with the experimentally measured flux of 210 L/m^2-h (see Table 2.2). Note that our fluxes are comparable to those reported in membrane separation literature for dead-end filtration[38] and cross-flow filtration[4], where separation was engendered using an energy intensive, externally applied pressure difference, as opposed to the sole use of gravity in this report. As the flux of hexadecane-rich permeate through

the hydrophobic and oleophilic membrane is constrained by the material balance, the maximum possible flux may be significantly higher.

In addition, it is evident from Hagen-Poiseuille relation[33] that the flux decrease is proportional to the fourth power of the pore radius, when all other parameters are held constant. As the pore diameter decreases, viscous resistance to fluid flow through pores of the membrane increases and consequently, the flux decreases. We calculate that the flux predicted by Hagen-Poiseuille relation equals the flux predicted by the sedimentation velocity of water droplets when the membrane pore diameter is ~ 5 μm. Thus, for all pore diameters $2D >> 5$ μm, the flux of water-rich permeate is only limited by the sedimentation velocity and is independent of the pore diameter. As a result, we were able to obtain the same flux for water using both mesh 400 ($2D$ = 37.5 μm) and mesh 500 ($2D$ = 30.5 μm) during continuous separation. A membrane with a smaller pore diameter, such as mesh 500, has a higher value for $P_{breakthrough}$ and is therefore more resistance to pressure perturbations.

Table 2.2. Measured fluxes for the water-rich permeate and the hexadecane-rich permeate during the continuous separation of 30:70 v:v water-in-hexadecane emulsions as a function of time.

Time (hr)	Water-rich permeate flux (L/m^2-hr)	Hexadecane-rich permeate flux (L/m^2-hr)	Time (hr)	Water-rich permeate flux (L/m^2-hr)	Hexadecane-rich permeate flux (L/m^2-hr)
0	91.7	213.9	52	91.7	210.8
4	94.7	213.9	56	94.7	210.8
8	91.7	210.8	60	91.7	213.9
12	88.6	213.9	64	88.6	213.9
16	88.6	217.0	68	88.6	217.0
20	91.7	217.0	72	91.7	217.0
24	88.6	213.9	76	88.6	213.9
28	91.7	217.0	80	91.7	217.0
32	94.7	213.9	84	94.7	213.9
36	91.7	210.8	88	94.7	210.8
40	91.7	217.0	92	88.6	217.0
44	94.7	213.9	96	88.6	210.8
48	91.7	207.8	100	91.7	213.9

2.4. Conclusions

We have developed novel membranes with hygro-responsive surfaces, which are both superhydrophilic and superoleophobic. These membranes are oleophobic both in air and when submerged under water. Consequently, CFS-based unit operations using these membranes can separate a range of different oil–water mixtures, with >99% efficiency.

We have also engineered an apparatus that uses two CFS-based operations in parallel, to achieve continuous, solely gravity-driven separation of oil–water emulsions, with a separation efficiency 99.9%. We anticipate that our separation methodology will have numerous applications, including the clean-up of oil spills, wastewater treatment, fuel purification and the separation of commercially relevant emulsions.

2.5. References

1 Kota, A. K., Kwon, G., Choi, W., Mabry, J. M. & Tuteja, A. Hygro-responsive membranes for effective oil-water separation. *Nat Commun* **3**, (2012).

2 Kintisch, E. GULF OIL SPILL An Audacious Decision in Crisis Gets Cautious Praise. *Science* **329**, 735-736, (2010).

3 Cheryan, M. & Rajagopalan, N. Membrane processing of oily streams. Wastewater treatment and waste reduction. *J Membrane Sci* **151**, 13-28, (1998).

4 Hlavacek, M. Break-up of Oil-in-Water Emulsions Induced by Permeation through a Microfiltration Membrane. *J Membrane Sci* **102**, 1-7, (1995).

5 Sun, D. Z., Duan, X. D., Li, W. X. & Zhou, D. Demulsification of water-in-oil emulsion by using porous glass membrane. *J Membrane Sci* **146**, 65-72, (1998).

6 Hoffmann, S. & Nitsch, W. Membrane coalescence for phase separation of oil-in-water emulsions stabilized by surfactants and dispersed into smallest droplets. *Chem Eng Technol* **24**, 22-27, (2001).

7 Maartens, A., Jacobs, E. P. & Swart, P. UF of pulp and paper effluent: membrane fouling-prevention and cleaning. *J Membrane Sci* **209**, 81-92, (2002).

8 Kukizaki, M. & Goto, M. Demulsification of water-in-oil emulsions by permeation through Shirasu-porous-glass (SPG) membranes. *J Membrane Sci* **322**, 196-203, (2008).

9 Feng, L., Zhang, Z. Y., Mai, Z. H., Ma, Y. M., Liu, B. Q., Jiang, L. & Zhu, D. B. A super-hydrophobic and super-oleophilic coating mesh film for the separation of oil and water. *Angew Chem Int Edit* **43**, 2012-2014, (2004).

10 Tian, D. L., Zhang, X. F., Wang, X., Zhai, J. & Jiang, L. Micro/nanoscale hierarchical structured ZnO mesh film for separation of water and oil. *Phys Chem Chem Phys* **13**, 14606-14610, (2011).

11 Yuan, J. K., Liu, X. G., Akbulut, O., Hu, J. Q., Suib, S. L., Kong, J. & Stellacci, F. Superwetting nanowire membranes for selective absorption. *Nat Nanotechnol* **3**, 332-336, (2008).

12 Hu, B. & Scott, K. Influence of membrane material and corrugation and process conditions on emulsion microfiltration. *J Membrane Sci* **294**, 30-39, (2007).

13 Binks, B. P. Particles as surfactants - similarities and differences. *Curr Opin Colloid In* **7**, 21-41, (2002).

14 Tadros, T., Izquierdo, R., Esquena, J. & Solans, C. Formation and stability of nano-emulsions. *Adv Colloid Interfac* **108**, 303-318, (2004).

15 Jacques Meunier, D. L., Professor Nino Boccara. *Physics of Amphiphilic Layers*. (Springer Proceedings in Physics, 1987).

16 Yang, J., Zhang, Z. Z., Xu, X. H., Zhu, X. T., Men, X. H. & Zhou, X. Y. Superhydrophilic-superoleophobic coatings. *J Mater Chem* **22**, 2834-2837, (2012).

17 Tuteja, A., Choi, W., Ma, M. L., Mabry, J. M., Mazzella, S. A., Rutledge, G. C., McKinley, G. H. & Cohen, R. E. Designing superoleophobic surfaces. *Science* **318**, 1618-1622, (2007).

18 Jung, Y. C. & Bhushan, B. Wetting Behavior of Water and Oil Droplets in Three-Phase Interfaces for Hydrophobicity/philicity and Oleophobicity/philicity. *Langmuir* **25**, 14165-14173, (2009).
19 Lin, L., Liu, M. J., Chen, L., Chen, P. P., Ma, J., Han, D. & Jiang, L. Bio-Inspired Hierarchical Macromolecule-Nanoclay Hydrogels for Robust Underwater Superoleophobicity. *Adv Mater* **22**, 4826-4830, (2010).
20 Marmur, A. From hygrophilic to superhygrophobic: Theoretical conditions for making high-contact-angle surfaces from low-contact-angle materials. *Langmuir* **24**, 7573-7579, (2008).
21 Choi, W., Tuteja, A., Chhatre, S., Mabry, J. M., Cohen, R. E. & McKinley, G. H. Fabrics with Tunable Oleophobicity. *Adv Mater* **21**, 2190-2195, (2009).
22 Kwok, D. Y. & Neumann, A. W. Contact angle measurement and contact angle interpretation. *Adv Colloid Interfac* **81**, 167-249, (1999).
23 Fowkes, F. M. Attractive Forces at Interfaces. *Ind Eng Chem* **56**, 40-52, (1964).
24 Owens, D. K. & Wendt, R. C. Estimation of Surface Free Energy of Polymers. *J Appl Polym Sci* **13**, 1741-1747, (1969).
25 Kakehi, H., Muira, M., Isu, N. & Sawada, H. Surface Modification of Aluminum Plate with Fluoroalkyl End-capped Acrylic Acid Oligomer/silica Nanocomposites-Oleophobic to Hydrophilic Switching Behavior Adapted to the Environmental Change on the Modified Plate Surface. *Polym J* **40**, 1081-1086, (2008).
26 Vaidya, A. & Chaudhury, M. K. Synthesis and surface properties of environmentally responsive segmented polyurethanes. *J Colloid Interf Sci* **249**, 235-245, (2002).
27 Howarter, J. A. & Youngblood, J. P. Amphiphile grafted membranes for the separation of oil-in-water dispersions. *J Colloid Interf Sci* **329**, 127-132, (2009).
28 Tirmizi, N. P., Raghuraman, B. & Wiencek, J. Demulsification of water/oil/solid emulsions by hollow-fiber membranes. *Aiche J* **42**, 1263-1276, (1996).
29 Xue, Z. X., Wang, S. T., Lin, L., Chen, L., Liu, M. J., Feng, L. & Jiang, L. A Novel Superhydrophilic and Underwater Superoleophobic Hydrogel-Coated Mesh for Oil/Water Separation. *Adv Mater* **23**, 4270-4273, (2011).
30 Kralj, J. G., Sahoo, H. R. & Jensen, K. F. Integrated continuous microfluidic liquid-liquid extraction. *Lab Chip* **7**, 256-263, (2007).
31 Angelescu, D. E., Mercier, B., Siess, D. & Schroeder, R. Microfluidic Capillary Separation and Real-Time Spectroscopic Analysis of Specific Components from Multiphase Mixtures. *Anal Chem* **82**, 2412-2420, (2010).
32 Ichikawa, T., Itoh, K., Yamamoto, S. & Sumita, M. Rapid demulsification of dense oil-in-water emulsion by low external electric field - I. Experimental evidence. *Colloid Surface A* **242**, 21-26, (2004).
33 Batchelor, G. K. *An Introduction in Fluid Dynamics*. (Cambridge University Press, 1970).
34 Margolis, S. A. Amperometric Measurement of Moisture in Transformer Oil Using Karl-Fischer Reagents. *Anal Chem* **67**, 4239-4246, (1995).
35 Schatzberg, P. Solubilities of Water in Several Normal Alkanes from C7 to C16. *J Phys Chem-Us* **67**, 776-779, (1963).

36 Schatzbe.P. Diffusion of Water through Hydrocarbon Liquids. *J Polym Sci Pol Sym*, 87-92, (1965).
37 Arnot, T. C., Field, R. W. & Koltuniewicz, A. B. Cross-flow and dead-end microfiltration of oily-water emulsions - Part II. Mechanisms and modelling of flux decline. *J Membrane Sci* **169**, 1-15, (2000).
38 Koltuniewicz, A. B., Field, R. W. & Arnot, T. C. Cross-Flow and Dead-End Microfiltration of Oily-Water Emulsion .1. Experimental-Study and Analysis of Flux Decline. *J Membrane Sci* **102**, 193-207, (1995).
39 Ishii, M. & Zuber, N. Drag Coefficient and Relative Velocity in Bubbly, Droplet or Particulate Flows. *Aiche J* **25**, 843-855, (1979).

CHAPTER 3

Self-cleaning membranes for efficient oil-water separation

3.1. Introduction

Recent events including the Deepwater Horizon oil spill in the Gulf of Mexico have highlighted the difficulty of effective oil-water separation[1,2]. To date, numerous separation methodologies including decantation, centrifugation, air floatation, coagulation and flocculation have been widely used to separate oil and water[3-7]. However, these methodologies are either unsuitable to separate oil-water emulsions, especially those stabilized by a surfactant, or are followed by a demulsification process through the addition of chemicals and/or application of heat or an electric field, which typically involves high energy consumption and secondary pollution[4,5,8-10]. Thus, energy-efficient and broadly applicable processes for oil-water separation are highly desired[2].

Membrane-based separation technologies are attractive because they are relatively energy-efficient, cost-effective, and are applicable across a wide range of industrial effluents[2,8]. Membrane-based separations of oil-water mixtures are classified[11,12] in terms of the membrane pore diameter (d), as microfiltration if 0.05 μm ≤ d < 10 μm, ultrafiltration if 1 nm ≤ d < 0.05 μm, or reverse osmosis if d < 1 nm. The membrane pore

size used in the separation of oil-water mixtures is strongly dependent on the dispersed phase diameter[8,13]. For an effective separation, the pore size is typically comparable or smaller than the dispersed phase diameter[13-16]. However, it is evident from the Hagen-Poiseulle relation that the flux decrease is proportional to the fourth power of the pore radius, when all other parameters are held constant[17]. As the pore diameter decreases, viscous resistance to fluid flow through a membrane's pore increases and consequently, the flux decreases[2,17]. Furthermore, membrane fouling during operation affects the flux. Pore clogging and/or preferential adsorption of a liquid that fouls the membrane are considered irreversible membrane fouling mechanisms, and cause a severe decrease in the flux[18-21]. Once the flux through the membrane declines, recovery is typically achieved by chemical treatments, membrane replacement or backflushing[22-24].

In addition to the decrease in the flux due to membrane fouling, poor selectivity hinders the widespread application of membrane-based separation technologies[25-27]. Recently, research on the critical role of preferential wettability has attracted attention to achieve the desired separation of oil and water[2,28-30]. Membranes with preferential wettability of oil over water, such as hydrophobic (or superhydrophobic) and oleophilic (or superoleophilic) membranes can selectively separate oil from oil-water mixtures. However, such membranes have disadvantages in that they are unsuitable for gravity-driven separation and are easily fouled by oil, causing a decrease in the flux[31-33]. Recently, a few membranes with hydrophilic (or superhydrophilic) and oleophobic (or superoleophobic) surfaces, capable of selectively separating water from oil-water mixtures, have been developed[2,34-36]. It has been demonstrated that they are suitable for gravity-driven separation and are highly resistant to fouling[2]. In order to produce

membranes that attain such preferential wettability, surface modification[34,37,38] or blending a polymer matrix[39-41] have been widely used. Although the appropriate surface treatment can create a surface with preferential wettability of water over oil, and fouling resistance, it may lead to the reduction in the pore diameter of membranes resulting in a decrease in the flux[42].

In this work, we have developed novel membranes with hygro-responsive surfaces[43], which are superhydrophilic ($\theta^*_{water} \approx 0^\circ$) and oleophobic ($\theta^*_{oil} > 90^\circ$). Controlled silanization of cellulose-based filter papers leads to a robust and homogeneous coating on the surface. This hygro-responsive coating can be applied to the filter papers having pore sizes as small as 10 nm. The developed membranes were found to have unique 'self-cleaning' ability as water can displace oil from the membrane surface. This allows the membranes to be extremely fouling resistant. Utilizing our membranes, we have demonstrated that our membranes can separate surfactant-stabilized oil-in-water emulsions with the oil droplets diameter as small as 10 nm.

3.2. Experimental Procedure

3.2.1. Materials

Cellulose-based filter papers with nominal pore sizes ≈ 200 nm or 450 nm were obtained from Sterlitech Corporation. Cellulose-based filter papers with nominal pore size ≈ 10 nm were obtained from Millipore. P25 cellulose film was obtained from Innovia film. Dodecane and poly(methyl methacrylate) (PMMA) were obtained from Sigma Aldrich. Methylene blue (blue dye), oil red-o (red dye), sodium dodecyl sulphate (SDS) and toluene were obtained from Fisher Scientific. Asahiklin AK-225 was obtained

from Structure Probe, Inc. Heptadecafluoro-1,1,2,2-tetrahydrodecyl triethoxy silane and 2-[methoxy (polyethyleneoxy)-propyl] trimethoxy silane were obtained from Gelest.

3.2.2. Substrate preparation

3.2.2.1. Substrates with hygro-responsive surface

Cellulose-based filter papers and films were treated using oxygen plasma for 5 min and subsequently exposed to vapor phase heptadecafluoro-1,1,2,2-tetrahydrodecyl triethoxysilane for 20 h at room temperature (~ 22 °C).

3.2.2.2.Conventional substrate with $\theta_{water} > \theta_{oil}$

A solution (10 mg/mL) of poly(methylmethacrylate) (PMMA) was prepared in Asahiklin AK-225. Cellulose-based filter papers and films were dip-coated in the solution for 30 min and dried with nitrogen gas at room temperature (~ 22 °C) for 5 min.

3.2.2.3. Conventional omniphilic substrate

A solution (1 mg/mL) of 2-[methoxy (polyethyleneoxy)-propyl] trimethoxy silane was prepared in toluene. Cellulosed-based filter papers and films were dip-coated in the solution for 18 h followed by thorough rinsing with ethanol and deionized water. They were then dried with nitrogen gas at room temperature (~ 22 °C) for 5 min.

3.2.3. Oil-water emulsion

A dodecane-in-water emulsion (20:80 v:v) was prepared by mixing water and dodecane by ultrasound sonication at an amplitude of 180 μm and a power of 240 W using Misonix ultrasonic liquid processor XL 2020. 0.1 mg of sodium dodecyl sulphate (SDS) per milliliter of emulsion was used. The prepared emulsions were then vacuum degassed to remove dissolved bubbles before they were used. Over time, a small degree of demulsification was observed.

3.2.4. Characterization techniques

3.2.4.1. Contact angle measurements

All measurements of contact angle were conducted using a Ramé–Hart 200-F1 goniometer. All contact angles reported in this work were measured by advancing or receding a small volume of liquid (~2 μl) onto the surface using a 2 ml micrometer syringe (Gilmont). At least three measurements were performed on each substrate. The typical error in measurements was ±2°.

3.2.4.2. Microscopy

The surface morphology of the membranes was characterized using a Hitachi SU8000 scanning electron microscope at 5kV. Optical microscopy of prepared emulsions were conducted using an Olympus BH-2 optical microscope.

3.2.4.3. Separation efficiency and droplet size distributions

The water content in both the dodecane-rich phase and the water-rich phase after separation was measured using a TA Discovery differential scanning calorimeter (DSC). Approximately 10 mg of the sample was frozen to – 30 °C. The sample was then thawed to 30 °C at a rate of 1.0 °C/min. The heat flow into the sample is measured. Dodecane melts around – 10 °C, while the crystallized water melts around 0 °C. Such a difference in melting points leads to separate peaks for the water and dodecane. By comparing the data obtained from DSC with calibration curves, the water content in the permeates was estimated. The size distribution of the dispersed phase was determined by dynamic light scattering (DLS) using a Malvern Zetasizer Nano ZS instrument.

3.3. Results and discussion

3.3.1. Self-cleaning surfaces in air

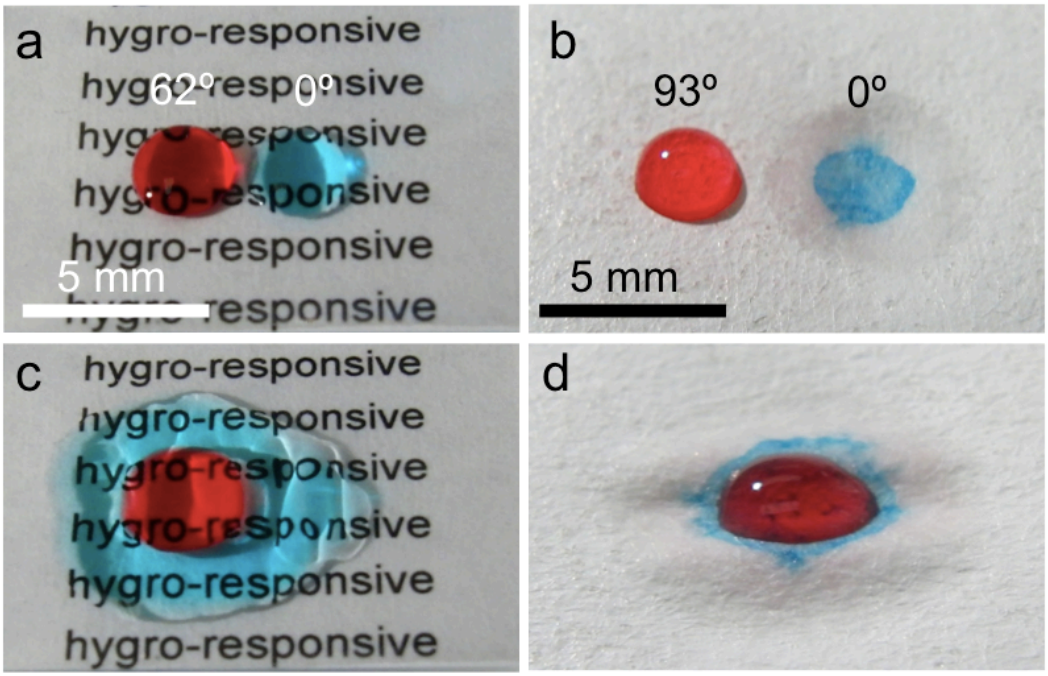

Figure 3.1 Self cleaning surfaces. (a) and (b) Droplets of water (dyed blue) and dodecane (dyed red) on a cellulose film (a) and cellulose-based filter paper with pore size ≈ 200 nm (b). Both surfaces have been treated with Heptadecafluoro-1,1,2,2-tetrahydrodecyl triethoxy silane. (c) and (d) Water displaces dodecane droplet from the surface. The displaced dodecane droplet floats on top of the water.

Figures 3.1a and 3.1b show the wetting behavior of water (γ_{lv} = 72.1 mN/m) and dodecane (γ_{lv} = 25.4 mN/m) on a cellulose film and a cellulosed-based filter paper (nominal pore size ≈ 200 nm), respectively, treated with vapor phase of heptadecafluoro-1,1,2,2-tetrahydrodecyl triethoxysilane (see section 3.2.2.1.). The advancing contact angles for dodecane and water are $\theta_{adv,dodecane}$ = 62° and $\theta_{adv,water}$ = 0° on the film (figure 3.1a) and $\theta^{*}_{adv,dodecane}$ = 93° and $\theta^{*}_{adv,water}$ = 0° on the filter paper (figure 3.1b). A possible

use for such preferential wettability of water over oil is in "self-cleaning" surfaces. Most self-cleaning surfaces that have been reported are superhydrophobic surfaces[44,45], such as the lotus leaf, and maintain a clean surface by causing droplets of water to bead up and roll-off, carrying away any unwanted dust or debris from the surface. However, if such superhydrophobic surfaces contact low surface tension liquids, such as oils or other contaminants, they rapidly lose their self-cleaning ability[46]. On the other hand, oils or other contaminants on surfaces with $\theta_{oil} > \theta_{water}$ can be easily cleaned with water as it can displace oil from the surfaces[47,48].

The surfaces fabricated here show such contact angle behavior. Figures 3.1c and 3.1d demonstrate that a droplet of dodecane (dyed red) can be removed from the surface by the application of water (dyed blue). The droplet of water was placed close enough to the oil droplet so that they can coalesce. After coalescence, the water undercuts and displaces the oil droplet on the surface (see figures 3.1c and 3.1d).

Figures 3.2a and 3.2b show the wetting behavior of water and dodecane on a cellulose film and a cellulosed-based filter paper (nominal pore size ≈ 200 nm), respectively, coated with PMMA (see section 3.2.2.2.). The advancing contact angles for dodecane and water are $\theta_{adv,dodecane}$ = 10° and $\theta_{adv,water}$ = 55° on the film (figure 3.2a) and $\theta^*_{adv,dodecane}$ = 0° and $\theta^*_{adv,water}$ = 92° on the filter paper (figure 3.2b). On such conventional surfaces with $\theta_{water} > \theta_{oil}$ (see figure 3.2a) or hydrophobic and oleophilic surfaces (see figure 3.2b), water was found to spread on top of dodecane, preventing the surface from being cleaned, even though the density of water is higher than that of dodecane (see figures 3.2c and 3.2d). This demonstrates the difficulty in cleaning oil or releasing soil stains from hydrophobic or superhydrophobic surfaces.

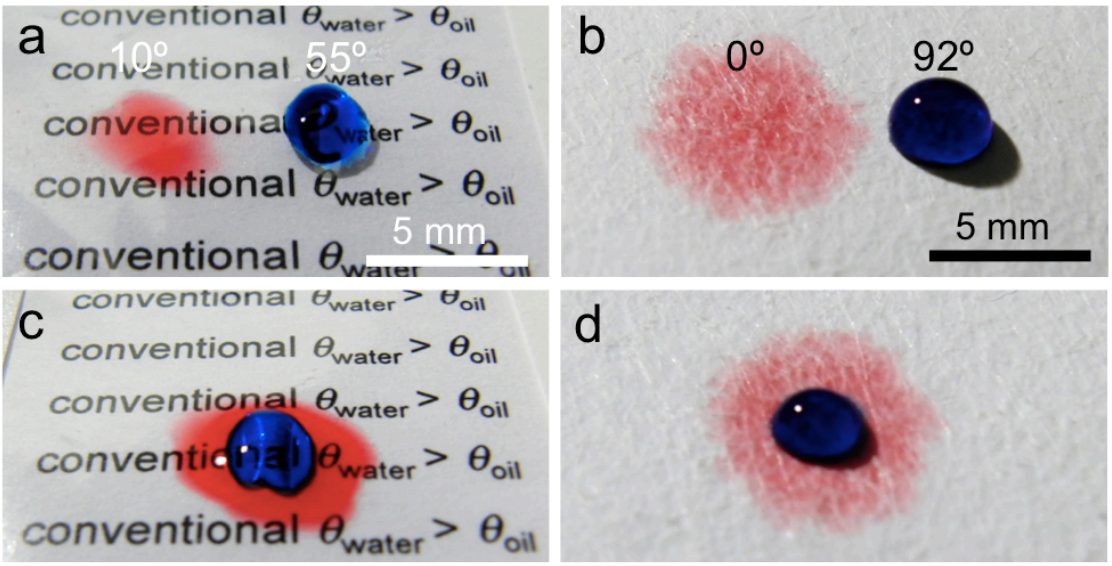

Figure 3.2 Surfaces with $\theta_{water} > \theta_{oil}$. (a) and (b) Droplets of water (dyed blue) and dodecane (dyed red) on a cellulose film (a) and cellulose-based filter paper with pore size ≈ 200 nm (b). Both surfaces have been coated with PMMA. (c) and (d) Water spreads on top of dodecane, preventing the surface from being cleaned.

Membranes with high surface energy including hydrophilic (or superhydrophilic) surfaces are easily contaminated with oils[49,50]. Once contaminated, it is difficult to clean the surface because the low surface tension of oils render them difficult to remove[47-50]. Figures 3.3a and 3.3b show droplets of water and dodecane on the omniphilic (i.e., both contact angles for water and oil < 90°) or superomniphilic (i.e., both contact angles for water and oil = 0°) surfaces coated with 2-[methoxy (polyethyleneoxy)-propyl] trimethoxy silane (see section 3.2.2.3.), respectively. The advancing contact angles for dodecane and water are $\theta_{adv,dodecane} = 0°$ and $\theta_{adv,water} = 16°$ on the film (figure 3.3a) and $\theta^*_{adv,dodecane} = 0°$ and $\theta^*_{adv,water} = 0°$ on the filter paper with nominal pore size ≈ 200 nm (figure 3.3b). Similar to conventional surfaces where $\theta_{water} > \theta_{oil}$ (see figure 3.2a), water

cannot displace the oil (see figures 3.3c and 3.3d). This indicates that water fails to clean the surface and oil is retained on omniphilic or superomniphilic surfaces.

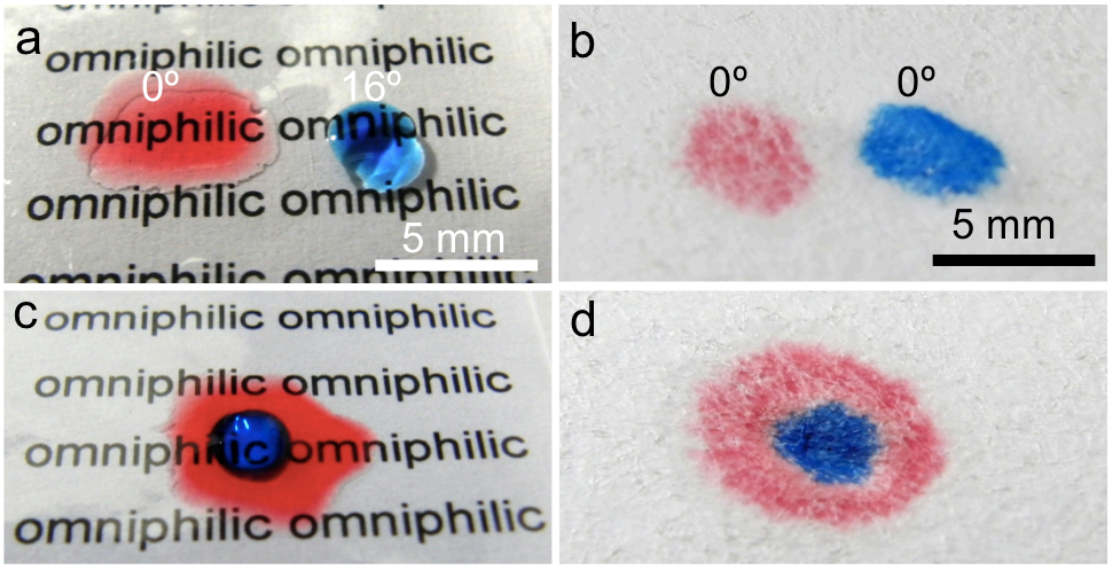

Figure 3.3 Omniphilic surfaces. (a) and (b) Droplets of water (dyed blue) and dodecane (dyed red) on a cellulose film (a) and cellulose-based filter paper with pore size ≈ 200 nm (b). Both surfaces have been treated with 2-[methoxy (polyethyleneoxy)-propyl] trimethoxy silane. (c) and (d) Water spreads on top of dodecane although the density of water is higher than that of dodecane.

3.3.2. Self-cleaning surfaces under oil

The mechanism for oil displacement is highly dependent on the wettability of surfaces discussed in section 3.3.1. For an efficient removal of low surface tension oils on a surface using water, it is necessary to design the surface with $\theta_{oil} > \theta_{water}$ such as hydrophilic (or superhydrophilic) and oleophobic (or superoleophobic) surfaces.

Self-cleaning surfaces have been widely used in various applications including stain-free cloth, anti-fogging windows and anti-fingerprint displays[47,48,51,52]. Self-cleaning

surfaces where water can displace oils have another application in the membrane-based separation of oil and water[38,51]. In previous literature, however, such membranes have the disadvantage of suffering from poor separation efficiency[38]. This is because oil droplets not only contact the membrane surface but they also form a film on the wall of the pores and strongly interact with the surface[53]. Furthermore, they typically lose their self-cleaning ability in the long-term due to the lack of robust and conformal coatings on the membranes[38]. Thus the membranes should retain their self-cleaning ability for effective separation of oil and water with high separation efficiency as well as long-term usage.

We demonstrate that the controlled silanization of cellulose-based filter papers can create a robust and homogeneous, hygro-responsive coating on the membrane's surface. This coating can be applied to filter papers having pore sizes as small as 10 nm without affecting the surface morphologies. Figures 3.4a-c show SEM images of surface morphologies for as-obtained cellulose-based filter papers with nominal pore sizes of 450 nm, 200 nm and 10 nm, respectively. Figures 3.4d-f show SEM images of surface morphologies for silanized cellulose-based filter papers (see section 3.2.2.1.) with nominal pore sizes of 450 nm, 200 nm and 10 nm, respectively. By comparing these with figures 3.4a-c, it is evident that the surface morphologies are not affected by silanization even on the membranes having ≈ 10 nm pore size.

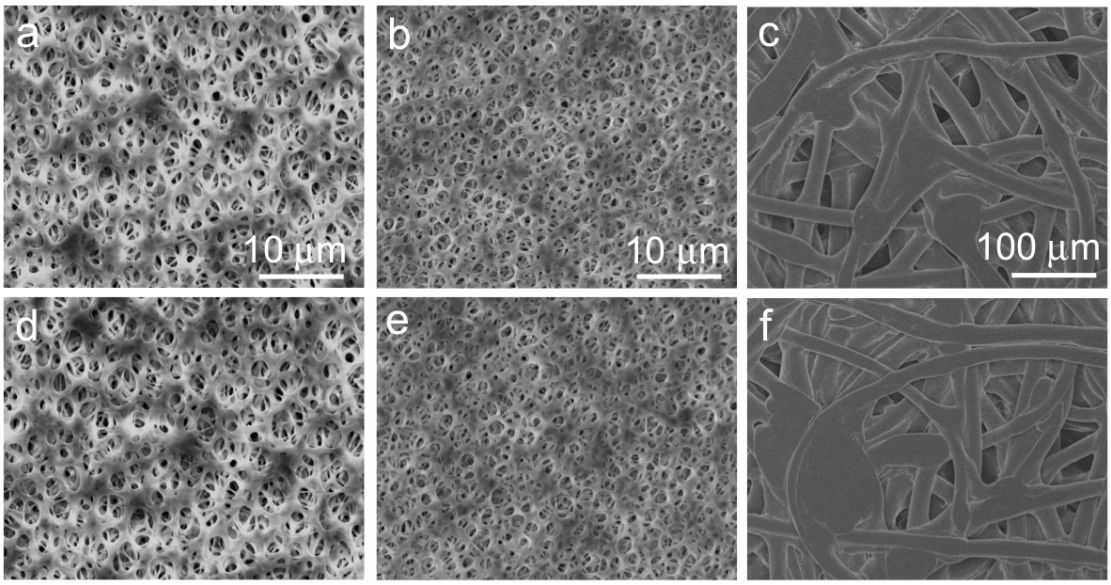

Figure 3.4 SEM images of cellulose-based filter papers. (a), (b) and (c) SEM images of filter papers with nominal pore sizes of 450 nm, 200 nm and 10 nm, respectively, before silanization. (d), (e) and (f) SEM images of filter papers with nominal pore sizes of 450 nm, 200 nm and 10 nm, respectively, after surface treatment.

We also demonstrate that our membranes retain their self-cleaning ability when they are contaminated or fully saturated with oils. In order to saturate our membranes (nominal pore size ≈ 200 nm) with dodecane, we apply a pressure ($P_{applied}$ = 30 kPa) which is higher than the measured breakthrough pressure for dodecane ($P_{breakthrough}$ = 20 kPa) on the membrane. After dodecane permeates through, the membrane is completely imbibed by dodecane. Since the transition from the Cassie-Baxter state to the 'fully-wetted' Wenzel state is irreversible, dodecane wets the surface and walls of the pores in the membrane. Figures 3.5 shows sequential images of a water droplet placed on the membrane submerged in dodecane. When a droplet of water is added, it naturally settles on the membrane surface owing to its higher density. As soon as the water droplet

contacts the membrane, it starts to wet the surface and simultaneously it is imbibed into the pores by displacing oil, as is evident from a decrease in contact angle. This clearly indicates that our membranes maintain their self-cleaning ability even when they are completely contaminated or saturated with oils. This unique ability of our membranes, to displace oil from the surface, allows them to separate oil and water with very high separation efficiency, as is discussed in following section.

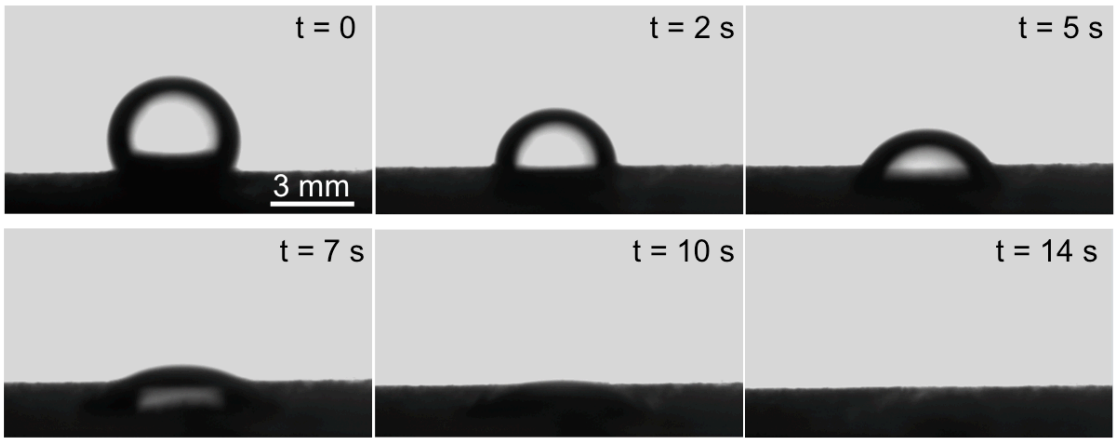

Figure 3.5 Self-cleaning surface under oil. A series of snapshots showing a droplet of water on a cellulose-based filter paper with pore size 200 nm, submerged in dodecane. The water droplet displaces dodecane and penetrates into the membrane in a few seconds.

3.3.3. Recovery of oleophobicity

Hydrophilic (or superhydrophilic) and oleophobic (or superoleophobic) membranes for the separation of oil and water considered in this work have attracted lots of attention because they are highly resistant to fouling by oils and are suitable for gravity-driven separation[2]. Such membranes allow water to selectively permeate through while oil is retained above the membranes[2]. In real cases, however, various sources

including mechanical vibration, gravity and Laplace pressure creates a significant pressure perturbation which may lead to the permeation of oil. Once oil permeates through the membrane, it is difficult to recover oleophobicity unless oil is displaced from the membrane surface by water. Thus the self-cleaning ability of the membrane, both in air and under oil, is critical for the separation of oil and water.

We demonstrate that our membranes can recover oleophobicity when they are fouled or saturated by oil. First, we saturate our membranes (nominal pore size ≈ 200 nm) with dodecane by applying $P_{applied}$ = 30 kPa > $P_{breakthrough}$ = 20 kPa for dodecane to permeate through the membrane. Then the membrane is immersed in dodecane so that the membrane surface and walls of the pores are completely wetted (see figure 3.6a inset). Figures 3.6a and 3.6b show the separation of free dodecane and water utilizing this prefouled membrane. The separation apparatus consists of a prefouled membrane (nominal pore size ≈ 200 nm) sandwiched between two vertical glass tubes. Water (dyed blue) is added to the upper tube immediately followed by dodecane (dyed red). Once water contacts the membrane, water displaces the dodecane entrapped in the membrane. Within minutes, the water-rich permeate passes through the membrane while the dodecane-rich retentate is retained above the membrane (see figure 3.6b). Note that negative pressure ($P_{applied}$ = 10 kPa < $P_{breakthrough}$ = 20 kPa) is continuously applied to the lower tube to facilitate the permeation of water. After separation, the water-rich permeate collected in the bottom tube is almost perfectly transparent, indicating that it is almost pure water. For a quantitative study, differential scanning colorimetriy (DSC) was used to probe the dodecane content in the water-rich permeate[54]. First the sample was frozen to – 30 °C and then thawed to 30 °C at a rate of 1.0 °C/s. The heat flow into the sample was

measured. Dodecane melts around – 10 °C, while the crystallized water melts around 0 °C. Such a difference in melting points leads to separate peaks for the water and dodecane. Figure 3.6c shows DSC data for the water-rich permeate obtained from the separation of free dodecane and water. Absence of a noticeable peak around – 10 °C indicates that dodecane is not present in the permeate at a discernable level. As might be expected, this is because water displaces dodecane entrapped in the membrane and consequently the membrane recovers its oleophobicity.

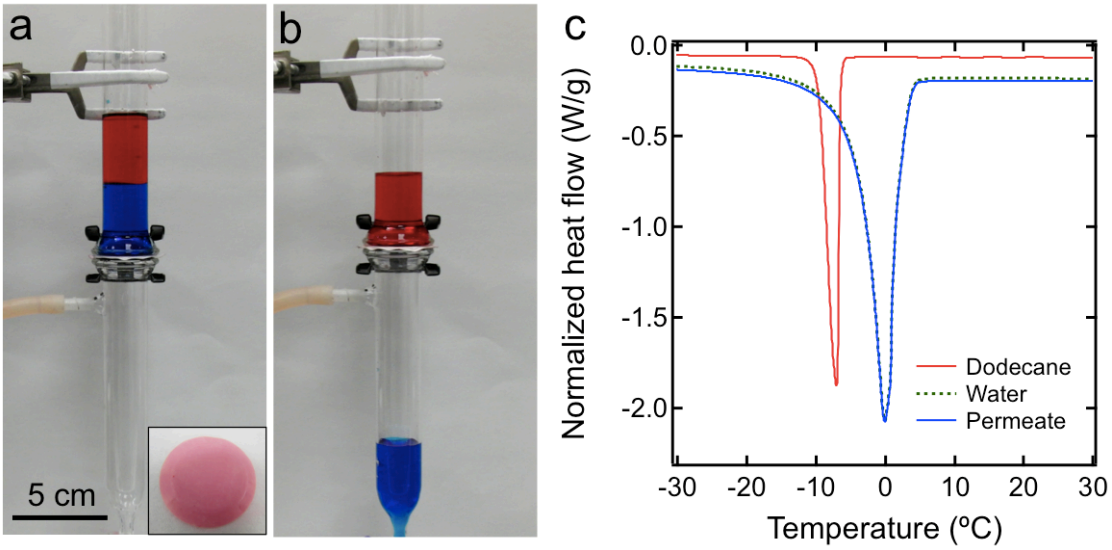

Figure 3.6 Recovery of oleophobicity. (a) Separation apparatus with water and dodecane above the membrane. The membrane sandwiched between the two glass tube is prefouled by dodecane. Inset, the membrane saturated with dodecane. Water is dyed blue and dodecane is dyed red. (b) The water-rich permeate passes through the membrane while the dodecane-rich retentate is retained above the membrane. (c) DSC data for the water-rich permeate. DSC data for as-obtained dodecane and water are also shown for comparison.

We also demonstrate that our membrane which is prefouled by oil can separate SDS-stabilized dodecane-in-water emulsions. Again, the membrane (nominal pore size ≈

200 nm) is saturated with dodecane (see figure 3.6a inset). Figure 3.7a and 3.7b show the separation of dodecane-in-water emulsion (20 vol% dodecane) stabilized using SDS. The apparatus is the same as that used for the separation of free dodecane and water. The emulsion is added to the upper tube (see figure 3.7a). Once water contacts the membrane, water displaces dodecane from the surface. Within minutes, the water-rich permeate passes through the membrane while the dodecane-rich retentate is retained above the membrane (see figure 3.7b). In order to facilitate water permeation, negative pressure ($P_{applied}$ = 10 kPa < $P_{breakthrough}$ = 20 kPa) is continuously applied to the lower tube. Comparing the image of the membrane after separation (see figure 3.7b inset) with the inset in figure 3.6a, it indicates that the membrane surface is cleaned due to the displacement of dodecane. DSC measurements (see figure 3.7c) indicate that the water-rich permeate does not contain dodecane at a discernible level. Additional experiments show that our membranes with different pore sizes (450 nm and 10 nm) can also recover oleophobicity, allowing for the separation of dodecane-in-water emulsions.

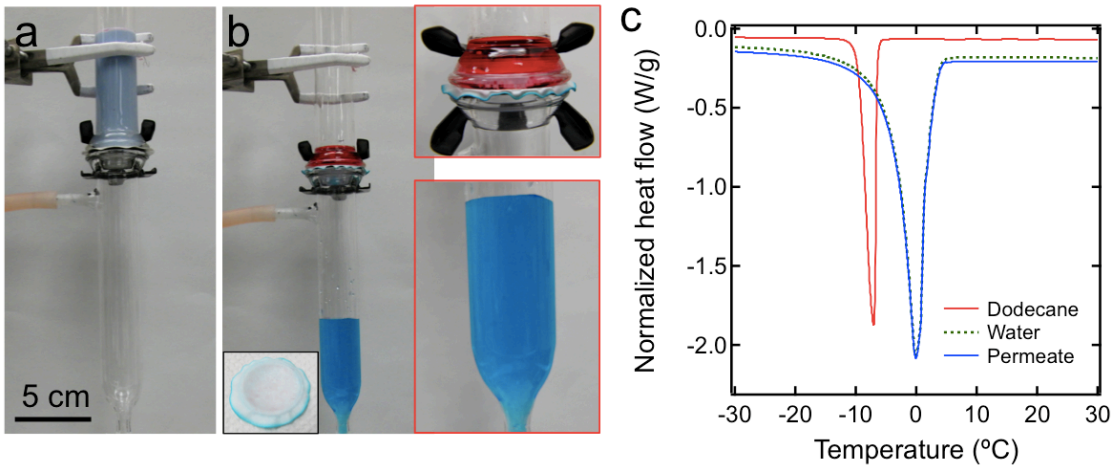

Figure 3.7 Recovery of oleophobicity. (a) Separation apparatus with a 20:80 v:v dodecane-in-water emulsion above the membrane. The membrane sandwiched between the two glass tube is prefouled by dodecane. Water is dyed blue and dodecane is dyed red. (b) The water-rich permeate passes through the membrane while the dodecane-rich retentate is retained above the membrane. (c) DSC data for the water-rich permeate. DSC data for as-obtained dodecane and water are also shown for comparison.

3.3.4. Separation of dodecane-in-water emulsions

The pore size of the membrane has a strong effect on the separation efficiency[55]. For an effective separation, the pore size of the membrane should be comparable or smaller than the dispersed phase diameter[13-16]. This is because membranes with larger pore size are likely to allow smaller dispersed droplets to readily permeate through the membrane. However, it is evident from the Hagen-Poiseulle relation that the flux decrease is proportional to the fourth power of the pore radius, when all other parameters are held constant[17]. Therefore, it is critical to use membranes with the appropriate pore size in the separation operations. Here we utilized membranes with three different pore

sizes (450 nm, 200 nm and 10 nm) to separate SDS-stabilized dodecane-in-water emulsions.

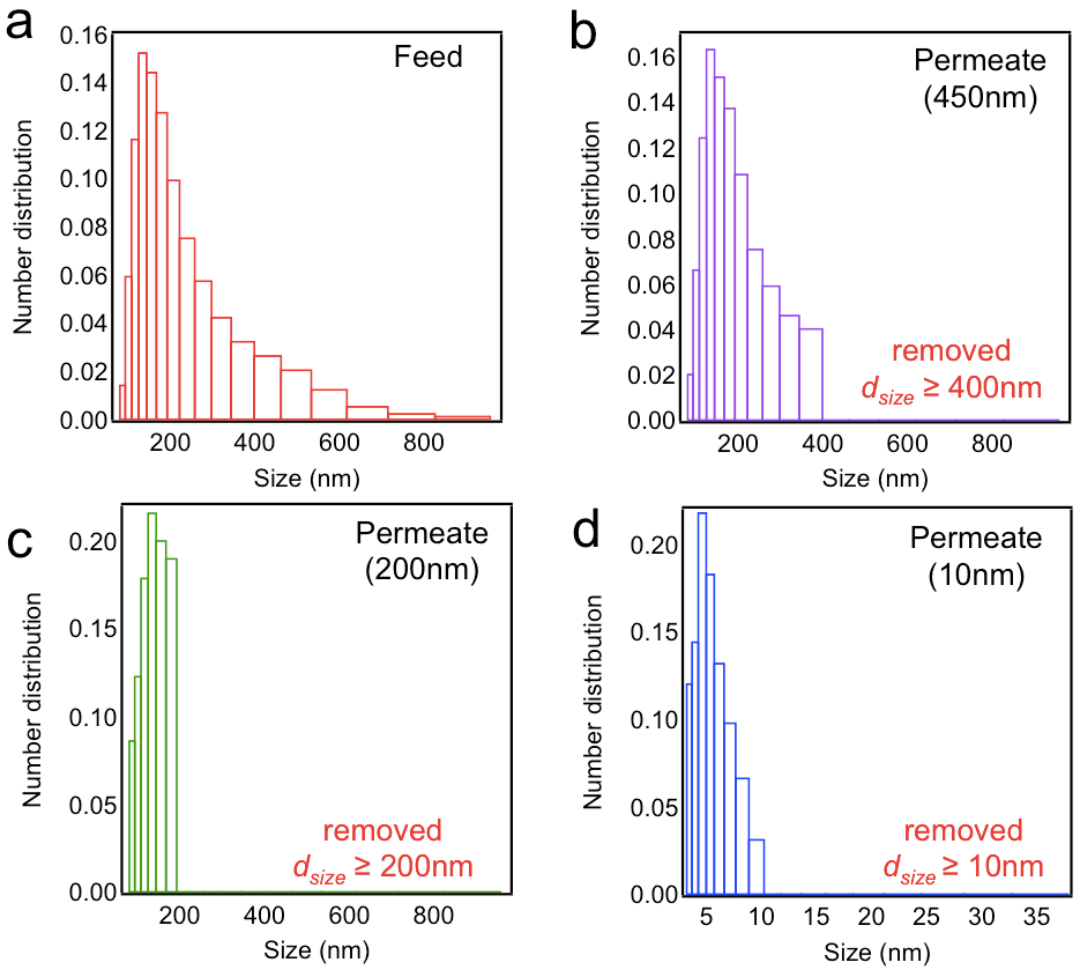

Figure 3.8 Size distributions of dodecane droplets (a) The number size distribution for the dodecane-in-water feed emulsion. (b), (c) and (d) The number size distributions for the permeates obtained from the separation of dodecane-in-water feed emulsion using filter papers with pore size = 450 nm, 200nm and 10 nm, respectively.

Figure 3.8a shows the number size distribution of the dispersed phase in dodecane-in-water feed emulsions (20 vol% dodecane) determined using DLS. The size

of the dispersed phase in the feed emulsion varies between 1 nm – 950 nm. Figures 3.8b-d show the number size distributions of the permeates obtained from separation of the feed emulsion using membranes with pore sizes of 450 nm, 200nm and 10 nm, respectively. Comparing the dodecane-in-water feed emulsion with the permeates, it is evident that dodecane droplets above the pore size of the membrane used in each separation were completely removed. This is a direct consequence of size exclusion as previously reported[56-58]. In addition, the self-cleaning ability of our membranes promotes water to displace dodecane droplets and release it from the membrane surface[38]. After water has displaced the dodecane, the dodecane droplets larger than the pore size of the membrane are easily removed during separations.

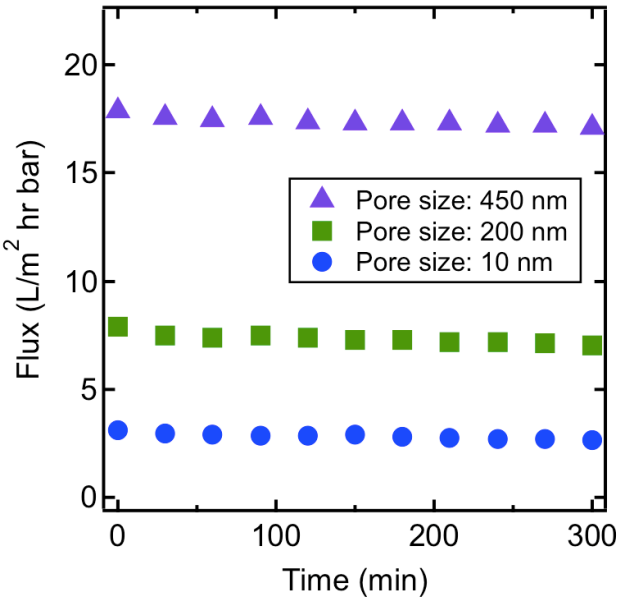

Figure 3.9 Measured fluxes for the permeates obtained from separations of dodecane-in-water emulsion using a membrane with different pore size.

Figure 3.9 shows measured fluxes of the water-rich permeates through the membranes with different pore sizes. The fluxes were measured to be 17.7 , 7.4 and 2.9 L/m^2-hr-bar using a membrane with pore size = 450 nm, 200nm and 10 nm, respectively. Furthermore, the fluxes decreased negligibly over a period of 5 hr (see figure 3.9 and table 3.1.), indicating that the membranes are highly resistant to fouling by oil. As might be expected, the self-cleaning ability of our membranes is a major contributing factor towards the observed resistance to fouling.

We also compared the total energy consumptions for separating oil-water mixtures using our hygro-responsive membrane with a conventional electrocoagulation technique, which is widely used in wastewater treatment. First, consider the separation of a dodecane-in-water emulsion using our hygro-responsive membrane. The separation described in this work requires electric energy to pump and to apply negative pressure to facilitate permeation of water-rich permeate. We estimated the electric energy required to separate 1 L of feed emulsion as 15 kJ. In the estimation, we assume the separation uses a scaled-up apparatus due to the hygro-responsive membrane being readily scalable. This value is lower than that required for the same amount of synthesized wastewater using a conventional electrocoagulation technique, which varies between 20 – 41 kJ[59-61]. Thus, our hygro-responsive membrane can be very useful for saving energy in oil-water separation and/or wastewater treatment.

Table 3.1 Measured fluxes for the permeates obtained from separations of 20:80 v:v dodecane-in-water emulsion using a membrane with different pore size.

Time (min)	Flux (L/m^2-hr-bar)		
	Pore size = 450 nm	Pore size = 200 nm	Pore size = 10 nm
0	17.9	7.6	3.1
30	17.6	7.5	2.9
60	17.5	7.4	2.9
90	17.6	7.5	2.8
120	17.4	7.4	2.8
150	17.3	7.3	2.9
180	17.3	7.3	2.8
210	17.3	7.2	2.7
240	17.2	7.2	2.7
270	17.2	7.1	2.7
300	17.1	7.1	2.7

3.4. Conclusions

In this work, we have demonstrated that silanization on the cellulose-based filter papers can also produce hygro-responsive surfaces, which are superhydrophilic and oleophobic. The controlled silanization adopted in this work creates a robust and homogeneous coating without clogging nanoscale pore as small as 10 nm. Our membranes were found to display unique wetting behaviors of oil and water, so-called 'self-cleaning', as water displaces oil from the surface. This self-cleaning property is important to membrane fouling resistance. We have demonstrated that our membranes

can recover their oleophobicity when they are fouled with oil by the application of water. We have also demonstrated that our membranes can separate surfactant-stabilized oil-water emulsions with the oil droplets diameter as small as 10 nm.

3.5. References

1 Kintisch, E. GULF OIL SPILL An Audacious Decision in Crisis Gets Cautious Praise. *Science* **329**, 735-736, (2010).

2 Kota, A. K., Kwon, G., Choi, W., Mabry, J. M. & Tuteja, A. Hygro-responsive membranes for effective oil-water separation. *Nat Commun* **3**, (2012).

3 J. D. Seader, E. J. H., D. Keith Roper. *Separation Process Principles*. (Wiley, 2011).

4 Al-Shamrani, A. A., James, A. & Xiao, H. Separation of oil from water by dissolved air flotation. *Colloid Surface A* **209**, 15-26, (2002).

5 Rubio, J., Souza, M. L. & Smith, R. W. Overview of flotation as a wastewater treatment technique. *Miner Eng* **15**, 139-155, (2002).

6 Xue, Z. X., Cao, Y. Z., Liu, N., Feng, L. & Jiang, L. Special wettable materials for oil/water separation. *J Mater Chem A* **2**, 2445-2460, (2014).

7 Zhu, Y. Z., Wang, D., Jiang, L. & Jin, J. Recent progress in developing advanced membranes for emulsified oil/water separation. *Npg Asia Mater* **6**, (2014).

8 Cheryan, M. & Rajagopalan, N. Membrane processing of oily streams. Wastewater treatment and waste reduction. *J Membrane Sci* **151**, 13-28, (1998).

9 Ichikawa, T. Electrical demulsification of oil-in-water emulsion. *Colloid Surface A* **302**, 581-586, (2007).

10 Rios, G., Pazos, C. & Coca, J. Destabilization of cutting oil emulsions using inorganic salts as coagulants. *Colloid Surface A* **138**, 383-389, (1998).

11 Mulder, M. *Basic Principles of Membrane Technology*. (Kluwer academic publishers, 1997).

12 Subramanian, G. *Bioseparation and Bioprocessing: A Handbook, 2 Volume Set, Volume 1*. (Wiley-VCH, 2007).

13 Cheryan, M. *Microfiltration and Ultrafiltration Handbook*. (Technomic Publishing, 1998).

14 Gabelman, A. & Hwang, S. T. Hollow fiber membrane contactors. *J Membrane Sci* **159**, 61-106, (1999).

15 Kajitvichyanukul, P., Hung, Y.-T. & Wang, L. K. *Handbook of Environmental Engineering, Vol 13: Membrane and Desalination Technologies*. 639 (The Humana Press Inc., 2011).

16 Belfer, S., Fainshtain, R., Purinson, Y., Gilron, J., Nystrom, M. & Manttari, M. Modification of NF membrane properties by in situ redox initiated graft polymerization with hydrophilic monomers. *J Membrane Sci* **239**, 55-64, (2004).

17 Batchelor, G. K. *An Introduction in Fluid Dynamics*. (Cambridge University Press, 1970).

18 Faibish, R. S. & Cohen, Y. Fouling-resistant ceramic-supported polymer membranes for ultrafiltration of oil-in-water microemulsions. *J Membrane Sci* **185**, 129-143, (2001).

19 Wetterau, G. E., Clark, M. M. & Anselme, C. A dynamic model for predicting fouling effects during the ultrafiltration of a groundwater. *J Membrane Sci* **109**, 185-204, (1996).

20 Song, L. F. Flux decline in crossflow microfiltration and ultrafiltration: mechanisms and modeling of membrane fouling. *J Membrane Sci* **139**, 183-200, (1998).
21 Kong, J. & Li, K. Oil removal from oil-in-water emulsions using PVDF membranes. *Sep Purif Technol* **16**, 83-93, (1999).
22 Faibish, R. S. & Cohen, Y. Fouling and rejection behavior of ceramic and polymer-modified ceramic membranes for ultrafiltration of oil-in-water emulsions and microemulsions. *Colloid Surface A* **191**, 27-40, (2001).
23 Asatekin, A., Menniti, A., Kang, S. T., Elimelech, M., Morgenroth, E. & Mayes, A. M. Antifouling nanofiltration membranes for membrane bioreactors from self-assembling graft copolymers. *J Membrane Sci* **285**, 81-89, (2006).
24 Shi, Y. F., Jin, F. X. & Wu, Y. Y. Microfiltration membrane bioreactor in stirred backflush operation for biotransformation using intact cells. *Process Biochem* **32**, 387-390, (1997).
25 Toyoda, M. & Inagaki, M. Heavy oil sorption using exfoliated graphite - New application of exfoliated graphite to protect heavy oil pollution. *Carbon* **38**, 199-210, (2000).
26 Zhu, Q., Pan, Q. M. & Liu, F. T. Facile Removal and Collection of Oils from Water Surfaces through Superhydrophobic and Superoleophilic Sponges. *J Phys Chem C* **115**, 17464-17470, (2011).
27 Yuan, J. K., Liu, X. G., Akbulut, O., Hu, J. Q., Suib, S. L., Kong, J. & Stellacci, F. Superwetting nanowire membranes for selective absorption. *Nat Nanotechnol* **3**, 332-336, (2008).
28 Shi, Z., Zhang, W. B., Zhang, F., Liu, X., Wang, D., Jin, J. & Jiang, L. Ultrafast Separation of Emulsified Oil/Water Mixtures by Ultrathin Free-Standing Single-Walled Carbon Nanotube Network Films. *Adv Mater* **25**, 2422-2427, (2013).
29 Wang, C. F. & Lin, S. J. Robust Superhydrophobic/Superoleophilic Sponge for Effective Continuous Absorption and Expulsion of Oil Pollutants from Water. *Acs Appl Mater Inter* **5**, 8861-8864, (2013).
30 Tao, M. M., Xue, L. X., Liu, F. & Jiang, L. An Intelligent Superwetting PVDF Membrane Showing Switchable Transport Performance for Oil/Water Separation. *Adv Mater* **26**, 2943-2948, (2014).
31 Hlavacek, M. Break-up of Oil-in-Water Emulsions Induced by Permeation through a Microfiltration Membrane. *J Membrane Sci* **102**, 1-7, (1995).
32 Maartens, A., Jacobs, E. P. & Swart, P. UF of pulp and paper effluent: membrane fouling-prevention and cleaning. *J Membrane Sci* **209**, 81-92, (2002).
33 Hu, B. & Scott, K. Influence of membrane material and corrugation and process conditions on emulsion microfiltration. *J Membrane Sci* **294**, 30-39, (2007).
34 Yang, J., Zhang, Z. Z., Xu, X. H., Zhu, X. T., Men, X. H. & Zhou, X. Y. Superhydrophilic-superoleophobic coatings. *J Mater Chem* **22**, 2834-2837, (2012).
35 Tian, D. L., Zhang, X. F., Wang, X., Zhai, J. & Jiang, L. Micro/nanoscale hierarchical structured ZnO mesh film for separation of water and oil. *Phys Chem Chem Phys* **13**, 14606-14610, (2011).

36 Xue, Z. X., Wang, S. T., Lin, L., Chen, L., Liu, M. J., Feng, L. & Jiang, L. A Novel Superhydrophilic and Underwater Superoleophobic Hydrogel-Coated Mesh for Oil/Water Separation. *Adv Mater* **23**, 4270-4273, (2011).
37 Gao, D. Superoleophobic and Superhydrophilic Fabric Filters for Rapid Water-Oil Separation. (2011).
38 Howarter, J. A. & Youngblood, J. P. Amphiphile grafted membranes for the separation of oil-in-water dispersions. *J Colloid Interf Sci* **329**, 127-132, (2009).
39 Masuelli, M., Marchese, J. & Ochoa, N. A. SPC/PVDF membranes for emulsified oily wastewater treatment. *J Membrane Sci* **326**, 688-693, (2009).
40 Ochoa, N. A., Masuelli, M. & Marchese, J. Effect of hydrophilicity on fouling of an emulsified oil wastewater with PVDF/PMMA membranes. *J Membrane Sci* **226**, 203-211, (2003).
41 Bowen, W. R., Cheng, S. Y., Doneva, T. A. & Oatley, D. L. Manufacture and characterisation of polyetherimide/sulfonated poly(ether ether ketone) blend membranes. *J Membrane Sci* **250**, 1-10, (2005).
42 Lin, Y. S. & Burggraaf, A. J. Experimental Studies on Pore-Size Change of Porous Ceramic Membranes after Modification. *J Membrane Sci* **79**, 65-82, (1993).
43 Marmur, A. From hygrophilic to superhygrophobic: Theoretical conditions for making high-contact-angle surfaces from low-contact-angle materials. *Langmuir* **24**, 7573-7579, (2008).
44 Barthlott, W. & Neinhuis, C. Purity of the sacred lotus, or escape from contamination in biological surfaces. *Planta* **202**, 1-8, (1997).
45 Patankar, N. A. Mimicking the lotus effect: Influence of double roughness structures and slender pillars. *Langmuir* **20**, 8209-8213, (2004).
46 Tuteja, A., Choi, W., Ma, M. L., Mabry, J. M., Mazzella, S. A., Rutledge, G. C., McKinley, G. H. & Cohen, R. E. Designing superoleophobic surfaces. *Science* **318**, 1618-1622, (2007).
47 Howarter, J. A. & Youngblood, J. P. Self-cleaning and next generation anti-fog surfaces and coatings. *Macromol Rapid Comm* **29**, 455-466, (2008).
48 Howarter, J. A. & Youngblood, J. P. Self-cleaning and anti-fog surfaces via stimuli-responsive polymer brushes. *Adv Mater* **19**, 3838-3843, (2007).
49 Goss, K. U. Predicting the Enrichment of Organic-Compounds in Fog Caused by Adsorption on the Water-Surface. *Atmos Environ* **28**, 3513-3517, (1994).
50 Dain, S. J., Hoskin, A. K., Winder, C. & Dingsdag, D. P. Assessment of fogging resistance of anti-fog personal eye protection. *Ophthal Physl Opt* **19**, 357-361, (1999).
51 Brown, P. S., Atkinson, O. D. L. A. & Badyal, J. P. S. Ultrafast Oleophobic-Hydrophilic Switching Surfaces for Antifogging, Self-Cleaning, and Oil Water Separation. *Acs Appl Mater Inter* **6**, 7504-7511, (2014).
52 Lai, Y. K., Tang, Y. X., Gong, J. J., Gong, D. G., Chi, L. F., Lin, C. J. & Chen, Z. Transparent superhydrophobic/superhydrophilic TiO2-based coatings for self-cleaning and anti-fogging. *J Mater Chem* **22**, 7420-7426, (2012).
53 Zhou, D. G. & Stenby, E. H. Displacement of Trapped Oil from Water-Wet Reservoir Rock. *Transport Porous Med* **11**, 1-16, (1993).

54 Enrico Drioli, L. G. *Comprehensive Membrane Science and Engineering*. Vol. 1 (Newnes, 2010).
55 Shin, C. & Chase, G. G. Water-in-oil coalescence in micro-nanofiber composite filters. *Aiche J* **50**, 343-350, (2004).
56 Barth, H. G., Boyes, B. E. & Jackson, C. Size exclusion chromatography and related separation techniques. *Anal Chem* **70**, 251R-278R, (1998).
57 Ray, A. K., Bird, P. B., Iacobucci, G. A. & Clark, B. C. Functionality of Gum-Arabic - Fractionation, Characterization and Evaluation of Gum Fractions in Citrus Oil-Emulsions and Model Beverages. *Food Hydrocolloid* **9**, 123-131, (1995).
58 Dobarganes, M. C., Perezcamino, M. C. & Marquezruiz, G. High-Performance Size Exclusion Chromatography of Polar Compounds in Heated and Non-Heated Fats. *Fett Wiss Technol* **90**, 308-311, (1988).
59 Pinotti, A. & Zaritzky, N. Effect of aluminum sulfate and cationic polyelectrolytes on the destabilization of emulsified wastes. *Waste Manage* **21**, 535-542, (2001).
60 Tir, M. & Moulai-Mostefa, N. Optimization of oil removal from oily wastewater by electrocoagulation using response surface method. *J Hazard Mater* **158**, 107-115, (2008).
61 Chavalparit, O. & Ongwandee, M. Optimizing electrocoagulation process for the treatment of biodiesel wastewater using response surface methodology. *J Environ Sci-China* **21**, 1491-1496, (2009).

CHAPTER 4

On-demand separation of oil-water mixtures[1]

4.1. Introduction

Over a hundred years ago, Lippmann observed that the capillary rise of mercury changes under an external electric potential[2]. However, his work had not been applied broadly because of electrolysis caused by current flow between a conductive liquid and the metallic substrate. Recently a thin insulating layer was introduced to prevent direct contact between the liquid and an electrode[3,4] (see figure 4.1) and observed a decrease in contact angle of a sessile droplet of a conductive liquid on the application of an external electric potential. The decrease in the macroscopic contact angle for a sessile polar liquid droplet on a dielectric material in response to an electric field is commonly known as electrowetting on a dielectric (EWOD)[5-7]. EWOD eliminates the problem of electrolysis and provides a facile route for tuning wettability of polar (or conducting) liquids. EWOD has found applications in numerous fields such as lab-on-chip devices[8-10], optics[11,12], and displays[13,14].

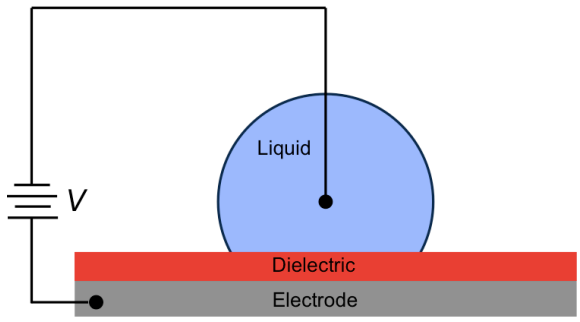

Figure 4.1 A schematic illustration of Electrowetting on a dielectric (EWOD) configuration.

While EWOD is traditionally employed on non-textured substrates, a few recent studies have demonstrated EWOD with textured substrates[15-17]. When a liquid contacts a textured substrate, it can adopt either the Cassie-Baxter state[18] or the Wenzel state[19]. In the Cassie-Baxter state, air is trapped between the liquid and the solid forming a composite (liquid-air-solid) interface. In the Wenzel state, the liquid fills all the cavities present on a textured surface, leading to so-called a 'fully-wetted' interface. Recent EWOD experiments on textured substrates reveal that polar liquids (e.g., water) can transition from the Cassie-Baxter state to the Wenzel state in response to the applied electric field[15-17]. However, non-polar liquids (e.g., oils) on textured substrates do not undergo such a transition.

For effective on-demand separation of oil-water mixtures, the membranes must be designed such that they support both water and oil in the Cassie-Baxter state before the electric field is applied. While it is relatively easy to support water in the Cassie-Baxter state because of its high surface tension, it is significantly more difficult to do so

with oils because of their low surface tension. Based on previous work[20-22] that recognized the importance of re-entrant texture (i.e., convex topography) along with surface chemistry in designing super-repellent surfaces, several superoleophobic membranes have been engineered[20-23] that can support both water and various oils in the Cassie-Baxter state under gravity.

Utilizing similar membranes in this work, we demonstrate a gravity-driven, membrane-based, single unit operation to separate various oil-water mixtures, including free oil and water, oil-in-water emulsions and water-in-oil emulsions, with ≥ 99.9% separation efficiency. The separation is triggered on-demand, i.e., upon applying an electric field. In addition, we have also developed an apparatus for the continuous separation of oil-water mixtures that features on-demand triggering.

4.2. Experimental Procedure

4.2.1. Materials

Sylgard184 base and curing agent was obtained from Dow Corning. 1H, 1H, 2H, 2H-heptadecafluorodecyl polyhedral oligomeric silsequioxane (fluorodecyl POSS) was synthesized as described elsewhere[24]. Asahiklin AK-225 solvent was obtained from Structure Probe, Inc. Nylon mesh of mesh size 376 (R = 20.3 μm, $2D$ = 28 μm) and stainless steel meshes of mesh size 100 (R = 56.5 μm, $2D$ = 138 μm) and 400 (R = 12.5 μm, $2D$ = 37.5 μm) were obtained from McMaster Carr. The mesh number refers to the number of openings per inch. Tecnoflon BR9151 fluoroelastomer was obtained from Solvay Solexis. Desmopan9370 polyurethane was obtained from Bayer Material Science. Hexadecane, tetrahydrofuran (THF), methylene blue (blue dye), oil red-o (red dye),

sodium dodecyl sulphate (SDS), polysorbate 80 (PS80) and span 80 were obtained from Fisher Scientific.

4.2.2. Non-textured substrate fabrication

A 10:1 w:w ratio of Sylgard184 base:curing agent was prepared in a petri dish, degassed in a vacuum oven at room temperature for 10 min and cross-linked at 70 ºC for 3 h. The cross-linked PDMS (x-PDMS) sheet (thickness, $d \sim 120$ μm) was sliced into 2 cm long x 2 cm wide pieces and spin-coated with 10 mg/ml solutions of 50 wt% fluorodecyl POSS + 50 wt% PDMS (10:1 w:w Sylgard 184 base:curing agent) in Asahiklin AK-225 at 1000 RPM for 20 s. The spin-coated surfaces were cross-linked at 70 ºC for 1 h. The substrate thickness $d \sim 120$ μm and the spin-coated layer of 50 wt% fluorodecyl POSS + x-PDMS were chosen so that they are similar to the textured substrates.

4.2.3. Textured substrate fabrication

2 cm long x 2 cm wide pieces of nylon membranes were dip-coated by immersing in 10 mg/ml solutions of 50 wt% fluorodecyl POSS + 50 wt% PDMS (10:1 w:w Sylgard 184 base:curing agent) in Asahiklin AK-225 for 30 min. Subsequently, the dip-coated membranes were dried with air at room temperature for 3 min and cross-linked at 70 ºC for 1 h. The nylon membranes were dip-coated with 50 wt% fluorodecyl POSS + x-PDMS. A stack of three dip-coated nylon membranes and a stainless steel membrane (mesh size 100) formed the membrane module. The hydrophobic and oleophilic membranes used in continuous separation were made by dip-coating stainless steel membranes (mesh size 400) in 10 mg/ml solution of Desmopan 9370 in THF.

4.2.4. Oil-water emulsions

50:50 vol:vol hexadecane-in-water emulsions were prepared by mixing water and hexadecane using a stir bar (800-1200 RPM) with 0.75 mg of PS80/ml of emulsion, while 30:70 vol:vol water-in-hexadecane emulsions were prepared with 1.0 mg of span80/ml of emulsion. The hydrophilic-lipophilic balance (HLB) values of PS80 and span80 are 15 and 4, respectively. We determined whether an emulsion is hexadecane-in-water or water-in-hexadecane by measuring the electrical resistance with a multimeter. A KDScientific KDS-200 syringe pump was used to deliver the feed emulsions during continuous separation.

4.2.5. Characterization techniques

4.2.5.1. Contact angle and surface tension measurements

All measurements of contact angle (in air and under water) were conducted using a Ramé–Hart 200-F1 goniometer. All contact angles reported in this work were measured by advancing or receding a small volume of liquid (~2 μl) onto the surface using a 2-ml micrometer syringe (Gilmont). At least three measurements were performed on each substrate. The typical error in measurements was ±2°. We determined the surface tension of water and hexadecane in the presence of surfactants using the capillary rise method.

4.2.5.2. Thermogravimetric analysis and Karl Fischer analysis

Composition of the hexadecane-rich and the water-rich phases after separation was measured using a Perkin Elmer Pyris 1 TGA. Approximately 50 mg of the sample was heated from room temperature to 105°C at a rate of 5 °C/s, and the temperature was held constant at 105 °C for 60 minutes. Note that the boiling point of hexadecane is 287 ºC. The loss in weight of water was used to estimate the purity of the water-rich phase.

The loss in weight of the hexadecane-rich phase was compared with the loss in weight of the as-obtained hexadecane to estimate the purity of the hexadecane-rich phase. The water content in the hexadecane-rich phase was also determined by injecting samples ranging from 10 μL to 0.6 mL into an EM Science AquaStar C3000 Titrator for coulometric Karl Fischer titration analysis (ASTM D6304).

4.2.5.3. Transmittance, dynamic light scattering and optical microscopy

The transmittance of the feed emulsions and the permeates was measured using a Cary 50 Bio UV-vis spectrophotometer. The size distribution of the dispersed phase with droplet sizes less than 1 μm was determined by dynamic light scattering using a Malvern Zetasizer Nano ZS instrument. Optical microscopy of the emulsions was conducted using an Olympus BH-2 optical microscope.

4.3. Results and discussion

4.3.1. EWOD of water and oil on non-textured substrates

For non-textured substrates, the decrease in the macroscopic contact angle as a function of the electric field during EWOD is expressed by the Young-Lippmann equation as[4]:

(Equation 4.1) $$\cos\theta^{ew} = \cos\theta + \frac{\varepsilon_o \varepsilon_d}{2\gamma_{12} d} V^2$$

Here, θ^{ew} is the macroscopic contact angle observed at a distance on the order of dielectric thickness d or larger from the three-phase contact line[5], θ is the Young's contact angle[25], ε_0 is the vacuum permittivity, γ_{12} is the interfacial tension between the liquid and ambient medium, and V is the voltage applied across the dielectric of

permittivity ε_d. While the macroscopic contact angle decreases upon the application of an electric field, the local (or microscopic) contact angle close to the three-phase contact line does not change and remains equal to the Young's contact angle[26,27].

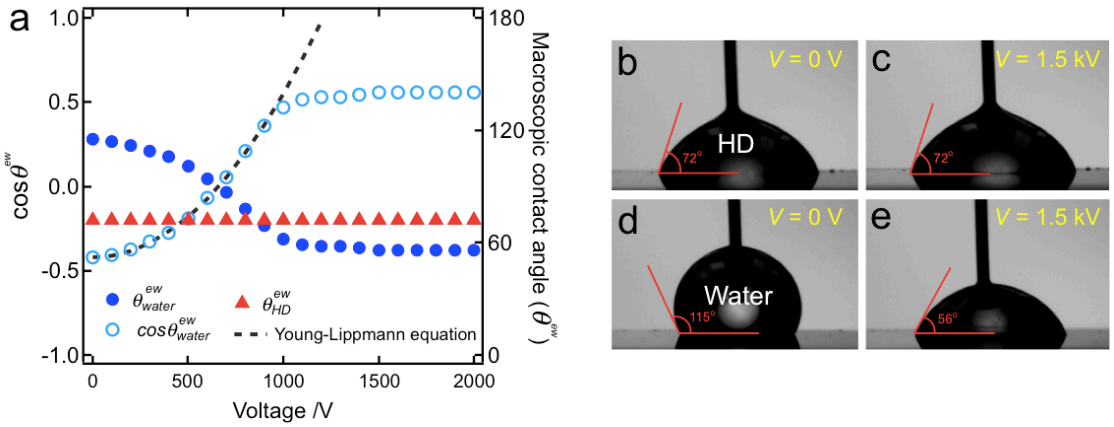

Figure 4.2 EWOD behavior of water and oil. (a) Macroscopic contact angles for water and hexadecane (HD) as a function of applied voltage on the non-textured substrate. (b) and (c) The macroscopic contact angle for hexadecane remain unchanged with increasing voltage. (d) and (e) The macroscopic contact angle for water decreases with increasing voltage.

In order to demonstrate the preferential wettability of water (polar liquid) over oil (non-polar liquid) upon the application of an electric field, we conducted EWOD of water (γ_{lv} = 72.1 mN/m) and hexadecane (representative oil, γ_{lv} = 27.5 mN/m) on non-textured 50 wt% fluorodecyl POSS + x-PDMS substrates. Figure 4.2a shows the macroscopic contact angles for water and hexadecane as a function of the voltage V applied across the dielectric layer. As may be expected, the macroscopic contact angle for the non-polar hexadecane ($\theta^{ew}_{hexadecane}$ = 72°) is independent of V (see figures 4.2b and 4.2c). On the other hand, the macroscopic contact angle for water decreases from θ^{ew}_{water} = 115° at V = 0 V

(see figure 4.2d) with increasing voltage and finally saturates at θ_{water}^{ew} = 56º for all V > 1.5 kV (see figure 4.2e). As shown in figure 4.2a, for ε_d = 1.9, the predictions from the Young-Lippmann equation (equation 4.1) match well with the experimental data, except for the contact angle saturation at high voltage. The inability of equation 4.1 to predict contact angle saturation has been well documented in literature and continues to remain an active area of research[5,28].

4.3.2. Transition from the Cassie-Baxter state to the Wenzel state

4.3.2.1. Derivation of the critical pressure $P_{critical}$ and the estimated values for $P_{critical}$

In the Cassie-Baxter state, the liquid-air interface makes an angle θ, locally with the substrate[29-31]. As the applied pressure $P_{applied}$ on the liquid increases, the liquid-air interface bends downward, thereby increasing the sagging angle $\delta\theta$. This in turn causes the liquid-air interface to advance downward along the solid surface in order to locally maintain an angle θ with the substrate[31] (see figure 4.3). For textured substrates possessing a spherical or cylindrical geometry and sufficiently large pore depth (such that the sagged liquid-air interface does not touch the bottom surface), the liquid-air interface continues to bend and advance downward along the surface curvature with increasing pressure, until it approaches a critical texture angle ψ_{cr}. The critical texture angle corresponds to the location where the liquid-air interface can withstand the maximum pressure $P_{critical}$, before transitioning to the Wenzel state.

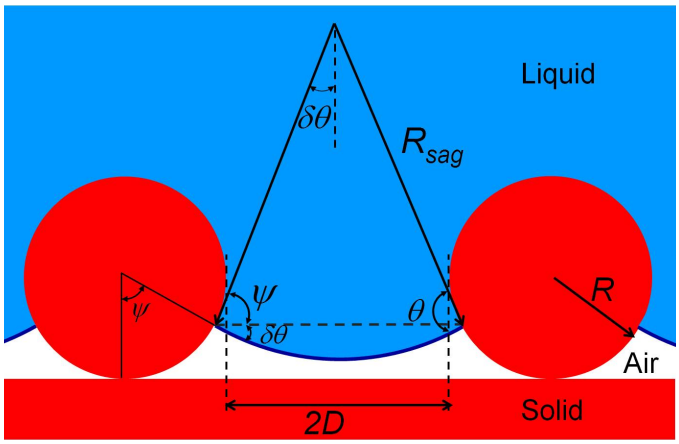

Figure 4.3 A schematic illustrating the pressure-induced sagging of the liquid-air interface.

We derived the critical texture angle (ψ_{cr}) and the maximum pressure ($P_{critical}$) for textured substrates possessing a cylindrical geometry, such as the membranes considered in this work. First, consider a liquid in the Cassie-Baxter state on a textured surface composed of periodic, non-woven cylindrical fibers with radius R and half inter-fiber spacing D (see figure 4.3). The liquid-air interface is located at a local texture angle ψ of the re-entrant texture with a sagging angle $\delta\theta = \theta - \psi$, as shown in figure 4.3. A force balance between the applied pressure $P_{applied}$ on a droplet and the surface tension γ_{12} can be written as:

(Equation 4.2) $P_{applied} \cdot \left(interfacial\ area\right) = \gamma_{12} \cdot \left(contact\ line\ length\right) \cdot \sin\delta\theta$

For cylindrical fibers of length L, equation 4.2 becomes:

(Equation 4.3) $P_{applied} \cdot L \cdot 2\left(D + R - R\sin\psi\right) = \gamma_{12} \cdot 2L \cdot \sin\delta\theta$

Simplifying equation 4.3, we get:

(Equation 4.4) $P_{applied} = \dfrac{\gamma_{12}\sin(\theta - \psi)}{D + R - R\sin\psi}$

For a given liquid and re-entrant texture geometry, equation 4.3 indicates that the applied pressure $P_{applied}$ determines the local texture angle ψ, where the liquid forms a stable composite interface. We determine the critical texture angle ψ_{cr}, which corresponds to the maximum pressure $P_{critical}$ that the liquid-air interface can withstand by solving:

(Equation 4.5) $\dfrac{dP_{applied}}{d\psi} = 0$ with $\dfrac{d^2P_{applied}}{d\psi^2} < 0$ at $\psi = \psi_{cr}$

From equations 4.4 and 4.5 we obtain,

$$(D + R - R\sin\psi_{cr})\cdot(-\cos(\theta - \psi_{cr})) - \sin(\theta - \psi_{cr})\cdot(-R\cos\psi_{cr}) = 0$$

$$\Rightarrow (D + R)\cdot\cos(\theta - \psi_{cr}) - R\sin\theta = 0$$

Simplifying further, we obtain,

(Equation 4.6) $P_{critical} = \dfrac{\gamma_{12}\sin(\theta - \psi_{cr})}{D + R - R\sin\psi_{cr}}$, where $\psi_{cr} = \theta - \cos^{-1}\left(\dfrac{R\sin\theta}{R + D}\right)$

When $P_{applied} > P_{critical}$, the liquid-air interface spontaneously advances downwards (i.e., to $\psi < \psi_{cr}$) and the liquid transitions to the Wenzel state.

Table 4.1 shows the values of $P_{critical}$ for water and hexadecane, with and without surfactants, on the dip-coated nylon membranes (R = 20.3 μm, $2D$ = 28 μm). We estimated the surface tensions γ_{12} for water and hexadecane with surfactants using the capillary rise method[32]. Note that Young's contact angle θ can be estimated from θ_{adv} and θ_{rec} as[33]:

(Equation 4.7) $$\theta = \cos^{-1}\left(\frac{\Gamma_{adv}\cos\theta_{adv} + \Gamma_{rec}\cos\theta_{rec}}{\Gamma_{adv} + \Gamma_{rec}}\right)$$

where,

(Equation 4.8) $$\Gamma_{adv} = \left(\frac{\sin^3\theta_{adv}}{2 - 3\cos\theta_{adv} + \cos^3\theta_{adv}}\right)^{1/3}$$

and

(Equation 4.9) $$\Gamma_{rec} = \left(\frac{\sin^3\theta_{rec}}{2 - 3\cos\theta_{rec} + \cos^3\theta_{rec}}\right)^{1/3}$$

The advancing and receding contact angles for water and hexadecane, with and without surfactants, are measured on surfaces spin-coated with 50 wt% fluorodecyl POSS + x-PDMS blend.

Table 4.1. Calculated values of $P_{critical}$ for water and hexadecane on the dip-coated nylon membranes (R = 20.3 μm, $2D$ = 28 μm), with and without surfactants.

	θ (θ_{adv}, θ_{rec})	γ_{12} (mN/m)	ψ_{cr}	$P_{critical}$ (Pa)
Water	115° (122°, 109°)	72.1	57.4°	3540
Water with 1.2 mg/ml PS80	79° (95°, 65°)	40.2	24.5°	1265
Hexadecane	72° (77°, 68°)	27.5	16.3°	794
Hexadecane with 0.3 mg/ml PS80	68° (75°, 61°)	24.9	11.3°	686
Hexadecane with 1.4 mg/ml span80	68° (76°, 61°)	25.7	11.3°	708

4.3.2.2. Electric field driven Cassie-Baxter to Wenzel transition

A liquid column of height h above a textured substrate exerts a hydrostatic pressure $P_{hydrostatic} = \rho g h$ on the liquid-air interface. Here, ρ is the effective density of the liquid column and the g is the acceleration due to gravity. In addition, when a polar liquid column is subjected to an electric field, a Maxwell stress $P_{Maxwell}$ is exerted on the liquid-air interface, pulling it outward along the surface normal[15,16]. Assuming a configuration similar to a parallel plate capacitor with air as the dielectric medium[16], $P_{Maxwell} = \varepsilon_o \varepsilon_d V^2 / 2 t_{eff}^2$. Here, ε_d = 1 is the relative permittivity of the dielectric medium (air), and t_{eff} is the thickness of the dielectric medium, i.e., the effective distance between the sagged liquid-air interface and the bottom electrode.

The membranes module adopted in this work consists of a stack of three dip-coated nylon membranes (R = 20.3 μm, $2D$ = 28 μm) and an electrode. When the liquid-air interface is located at $\psi = \psi_{cr}$ on the first layer of texture (i.e., the top dip-coated nylon membrane), t_{eff} is given as (see figure 4.4):

(Equation 4.10) $t_{eff} = 6R - R\left(1 + \cos\psi_{cr}\right) - R_{sag,cr}\left[1 - \cos\left(\theta - \psi_{cr}\right)\right]$

Here, $R_{sag,cr} = \left(D + R - R\sin\psi_{cr}\right) / \sin\left(\theta - \psi_{cr}\right)$ is the critical radius of curvature of the liquid-air interface. Using equation 4.10, we estimate t_{eff} = 81.1 μm for water and t_{eff} = 69.7 μm for water with 1.2 mg/ml of PS80.

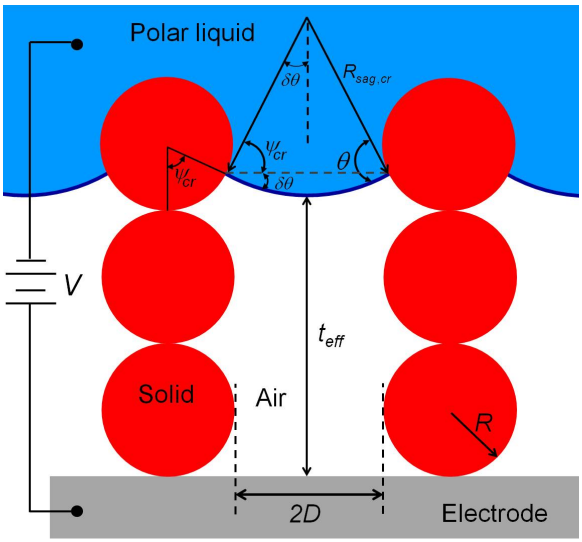

Figure 4.4 A schematic showing the pressure-induced sagging of the liquid-air interface on a stack of three membranes with cylindrical texture.

The liquid-air interface can withstand the maximum pressure $P_{critical}$ when it is located at $\psi = \psi_{cr}$. If the applied voltage V is such that $P_{applied} = \left(P_{hydrostatic} + P_{Maxwell}\right) > P_{critical}$, the liquid-air interface spontaneously advances downwards (i.e., to $\psi < \psi_{cr}$) until it reaches the bottom of the first layer of texture. At the same applied voltage V, the liquid cannot form a stable composite interface on subsequent layers of the texture (i.e., the middle or the bottom dip-coated nylon membranes) because $P_{Maxwell}$ is amplified due to a decrease in t_{eff} , which leads to an increase in $P_{applied}$. Consequently, once the liquid-air interface advances past $\psi = \psi_{cr}$ on the first layer of texture, the liquid transitions from the Cassie-Baxter state to the Wenzel state. On the other hand, a non-polar liquid (e.g., oil) in the Cassie-Baxter state under gravity, will not transition to the Wenzel state as it will not experience $P_{Maxwell}$.

4.3.3. Estimation of hexadecane-water interfacial tension in the presence of surfactants

We estimated the interfacial tension γ_{ow} between water and hexadecane in the presence of PS80 by using the relationship postulated by previous work[34]:

(Equation 4.11) $\gamma_{ow} = \gamma_{ov} + \gamma_{wv} - 2\sqrt{\gamma_{ov}^{d}\gamma_{wv}^{d}}$

Here, γ_{ow} is the hexadecane-water interfacial tension. γ_{ov} and γ_{wv} are the surface tensions, while γ_{ov}^{d} and γ_{wv}^{d} are the dispersive components of the surface tensions for hexadecane and water, respectively. Note that $\gamma_{ov} = \gamma_{ov}^{d}$ for hexadecane (non-polar liquid). Using the capillary rise method, we determined γ_{ov} = 24.9 mN/m with 0.3 mg/ml of PS80 and γ_{wv} = 40.2 mN/m with 1.2 mg/ml of PS80. In order to estimate γ_{wv}^{d}, we combined the Young's equation (equation 1.1) with equation 4.11 for the interfacial tension of a non-polar solid (such as a 50 wt% fluorodecyl POSS + x-PDMS blend) and water to obtain:

(Equation 4.12) $\gamma_{wv}^{d} = \dfrac{\gamma_{wv}(1+\cos\theta)}{4\gamma_{sv}^{d}}$

Here, γ_{sv}^{d} is the dispersive component of the solid surface energy and θ is the Young's contact angle for water. On a spin-coated surface of 50 wt% fluorodecyl POSS + x-PDMS, the contact angles for water with 1.2 mg/ml of PS80 is θ_{water} = 95°. Using this value in equation 4.12, we obtained γ_{wv}^{d} = 32.6 mN/m for water with 1.2 mg/ml of PS80. Substituting the values of γ_{ov}, γ_{wv} and γ_{wv}^{d} in equation 4.11, we determined γ_{ow} = 8.1 mN/m in the presence of PS80.

4.3.4. Batch separation of oil-water mixtures

4.3.4.1. Separation of free oil and water

To utilize the electric field driven preferential wettability transition of water over hexadecane for separation, it is essential to use porous oleophobic (or superoleophobic) membranes. Upon applying an electric field, under gravity, such a membrane allows water (higher density, polar liquid) to permeate through, but retains hexadecane (lower density, non-polar liquid). The oleophobic membrane module (see figure 4.5a inset) assembled for this work consists of a stack of three nylon membranes ($2D$ = 28 μm, R = 20.3 μm) and a stainless steel membrane ($2D$ = 138 μm, R = 56.5 μm). The stainless steel membrane serves as one electrode, while a copper wire immersed in water serves as the counter electrode. The nylon membranes are dip-coated with 50 wt% fluorodecyl POSS + x-PDMS. The nylon membranes are dip-coated with 50 wt% fluorodecyl POSS + x-PDMS. The membranes support both water ($\theta^{*}_{water,adv}$ = 142°) and hexadecane ($\theta^{*}_{hexadecane,adv}$ = 99°) in the Cassie-Baxter state before applying an electric field. On non-textured 50 wt% fluorodecyl POSS + x-PDMS substrates, at V = 0 V, $\theta_{hexadecane}$ = 72° and θ_{water} = 115° (see Table 4.1). Using these values in equation 4.6, we estimate $P_{critical,hexadecane}$ = 794 Pa for the hexadecane-air interface and $P_{critical,water}$ = 3540 Pa for the water-air interface (see Table 4.1).

The membrane module is sealed between two vertical glass tubes (see figure 4.5a). A 4 cm column of water (dyed blue) is added to the upper tube immediately followed by a 4 cm column of hexadecane (dyed red) on top of water. Before applying the electric field, the dip-coated nylon membranes can easily support a total liquid

column of height h = 8 cm because the hydrostatic pressure $P_{hydrostatic}$ = 694 Pa < $P_{critical,water}$ = 3540 Pa. Upon applying the electric field, the Maxwell stress $P_{Maxwell}$ increases with increasing voltage V across the dip-coated nylon membranes. At V = 2.1 kV, we calculate t_{eff} = 81.1 μm (see Table 4.1) and $P_{applied} \approx P_{critical,water}$. This matches well with our experimental observation of the permeation of water through the membrane module at an applied voltage $V = 2.0 \pm 0.3$ kV. Note that the electric field is applied only for a short period of time because after water permeates through the dip-coated nylon membranes, contact with the stainless steel membrane creates a path for current flow and an electric field is no longer required to maintain the flow of water. After a few minutes, all the water is collected in the lower tube, while hexadecane is retained in the upper tube (see figure 4.5b). The dip-coated nylon membranes can then prevent the permeation of hexadecane (column height h = 4 cm) because the hydrostatic pressure $P_{hydrostatic}$ = 302 Pa < $P_{critical,hexadecane}$ = 794 Pa.

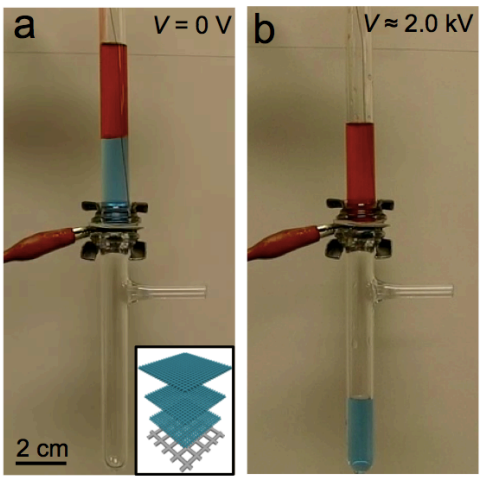

Figure 4.5 Batch separation of free oil and water. (a) An apparatus with a liquid column of free oil (dyed red) and water (dyed blue) above the membrane before applying an electric field. The inset shows a schematic of the membrane module. (b) Water permeates through while hexadecane is retained when a voltage V ~ 2.0 kV is applied.

4.3.4.2. Separation of oil-in-water emulsion

We have also extended our separation methodology to separate oil-in-water emulsion. Here, we demonstrate polysorbate80 (PS80, 0.75 mg/ml) stabilized 50:50 vol:vol hexadecane-in-water emulsions. First, we determined the size distributions of the dispersed phase in the emulsions using two techniques – optical microscopy image analysis for droplets above 1 µm in diameter and dynamic light scattering for droplets below 1 µm. Figure 4.6a shows representative optical microscopy image for the 50:50 vol:vol PS80 stabilized hexadecane-in-water emulsion. Figures 4.6b and 4.6c show the number size distributions of the dispersed phase determined using image analysis and DLS, respectively. The average size of dispersed phase is between 10-20 µm and 200-300 nm, respectively.

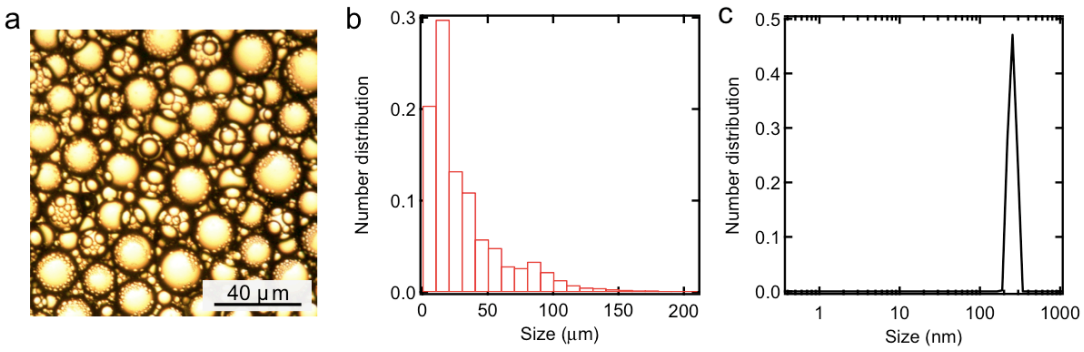

Figure 4.6 Size distributions of hexadecane droplets in the feed hexadecane-in-water emulsion. (a) A representative optical microscopy image of the feed hexadecane-in-water emulsion. (b) and (c) The number size distributions for the hexadecane-in-water feed emulsion for droplets > 1 µm and < 1 µm, respectively.

To demonstrate the preferential wetting of water over oil, in the presence of PS80, we measured the macroscopic contact angles for water with 1.2 mg/ml of PS80 (γ_{lv} =

40.2 mN/m) and hexadecane with 0.3 mg/ml of PS80 (γ_{lv} = 24.9 mN/m) as a function of the voltage V applied across the dielectric layer (see figure 4.7a). The macroscopic contact angle for hexadecane ($\theta^{ew}_{hexadecane}$ = 68°) is independent of V, while the macroscopic contact angle for water decreases from θ^{ew}_{water} = 80º at V = 0 V until it saturates at θ^{ew}_{water} = 38º for all V > 0.8 kV. For ε_d = 1.9 (as was the case for the data shown in figure 4.2a), the predictions from equation 4.1 match well with experimental data.

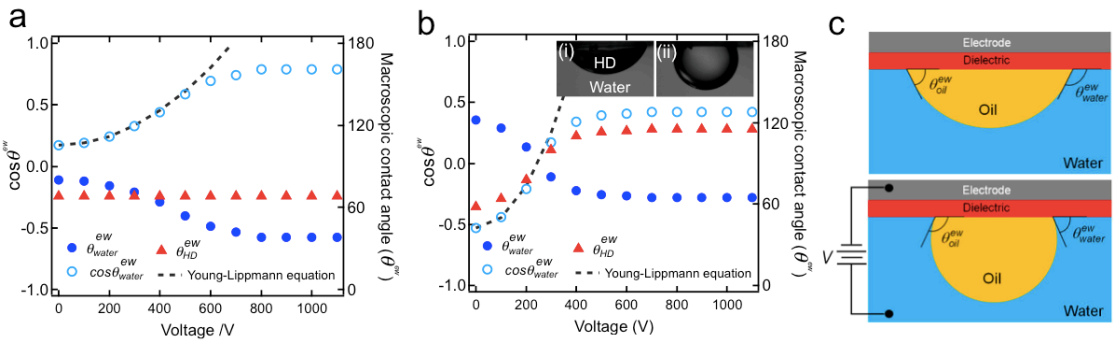

Figure 4.7 EWOD behavior of water and oil in the presence of PS80. (a) Macroscopic contact angles for water and hexadecane (HD) in the presence of PS80 as a function of applied voltage on the non-textured substrate. (b) Competitive wetting of water and hexadecane containing PS80. Insets (i) and (ii) show the macroscopic contact angle for hexadecane before and after applying voltage, respectively. (c) A schematic showing the competitive wetting of water and oil.

In the case of hexadecane-in-water emulsions, the medium surrounding the emulsified hexadecane droplets is water. In order to study the wetting behavior of hexadecane surrounded by water upon applying an electric field, we conducted EWOD of a hexadecane droplet on a non-textured 50 wt% fluorodecyl POSS + x-PDMS substrate submerged in water, in the presence of PS80. Figure 4.7b shows the macroscopic contact

angles for hexadecane as a function of the voltage V applied across the dielectric layer. In contrast to the behavior observed in figures 4.2a and 4.7a, the macroscopic contact angle for hexadecane *increases* from $\theta^{ew}_{hexadecane}$ = 58º at V = 0 V (see inset (i) in figure 4.7b) until it saturates at $\theta^{ew}_{hexadecane}$ = 115º (see inset (ii) in figure 4.7b). This is a direct consequence of the decrease in the macroscopic contact angle for water, $\theta^{ew}_{water} = \pi - \theta^{ew}_{hexadecane}$, as shown in figure 4.7c. The macroscopic contact angle for water decreases from θ^{ew}_{water} = 122º at V = 0 V until it saturates at θ^{ew}_{water} = 65º, and this manifests as an increase in the macroscopic contact angle for hexadecane. For ε_d = 1.9 (as was the case for the data shown in figures 4.2a and 4.7a) and oil-water interfacial tension γ_{ow} = 8.1 mN/m, the predictions from equation 4.1 match well with experimental data for water.

Utilizing the electric field driven preferential wettability transition of water over hexadecane in the presence of PS80, we are able to separate hexadecane-in-water emulsions. The membrane module and the electrode configuration are the same as those used for free oil and water separation. In the presence of PS80, on non-textured 50 wt% fluorodecyl POSS + x-PDMS substrates, at V = 0 V, $\theta_{hexadecane}$ = 68° and θ_{water} = 79° (see Table 4.1). Using these values in equation 4.6, we estimate $P_{critical,hexadecane}$ = 686 Pa for the hexadecane-air interface (γ_{lv} = 24.9 mN/m) and $P_{critical,water}$ = 1265 Pa for the water-air interface (γ_{lv} = 40.2 mN/m).

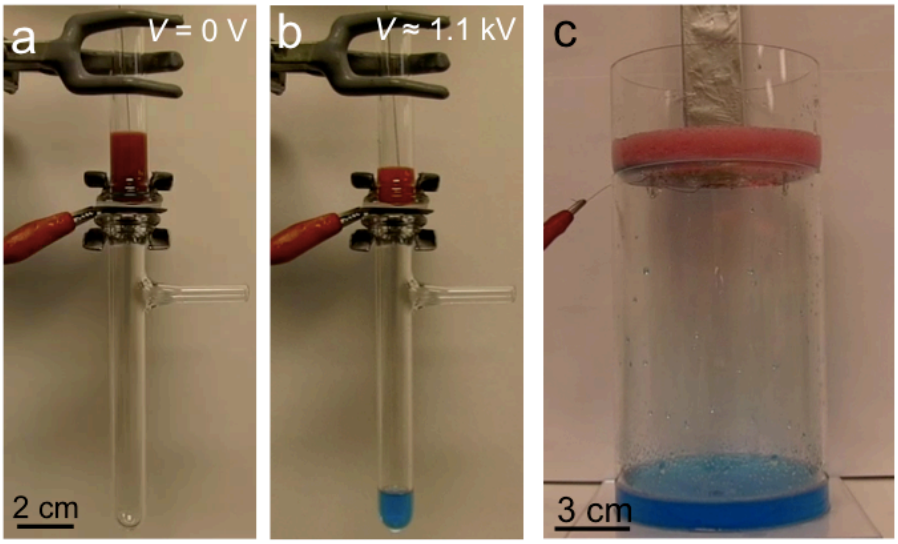

Figure 4.8 Separation of oil-in-water emulsion. (a) An apparatus with a liquid column of hexadecane-in-water emulsion above the membrane before applying an electric field. (b) Water-rich permeate passes through while hexadecane-rich retentate is retained when a voltage V ~ 1.1 kV is applied. (c) Separation of the hexadecane-in-water emulsion using a scaled-up apparatus. Water is dyed blue and hexadecane is dyed red.

Before applying an electric field, the dip-coated nylon membranes can support a 3 cm column of 50:50 vol:vol hexadecane-in-water emulsion (see figure 4.8a) because $P_{hydrostatic}$ = 260 Pa < $P_{critical,water}$ = 1265 Pa. Upon the application of the electric field, $P_{Maxwell}$ increases with increasing voltage, and at V = 1.1 kV, we calculate t_{eff} = 69.7 µm (see section 4.3.2.2), $P_{applied} \approx P_{critical,water}$. This matches well with our experimental observation of the permeation of water-rich phase through the membrane module at an applied voltage $V = 1.1 \pm 0.3$ kV. After separation (see figure 4.8b), the dip-coated nylon membranes can prevent the permeation of the hexadecane-rich phase (column height h = 1.5 cm) because $P_{hydrostatic}$ = 113 Pa < $P_{critical,hexadecane}$ = 686 Pa. Further, our dip-coating

based membrane module is easy to scale-up, we have developed an apparatus to separate several liters of hexadecane-in-water emulsions. Figure 4.8c shows the separation of hexadecane-in-water emulsion using scaled-up apparatus.

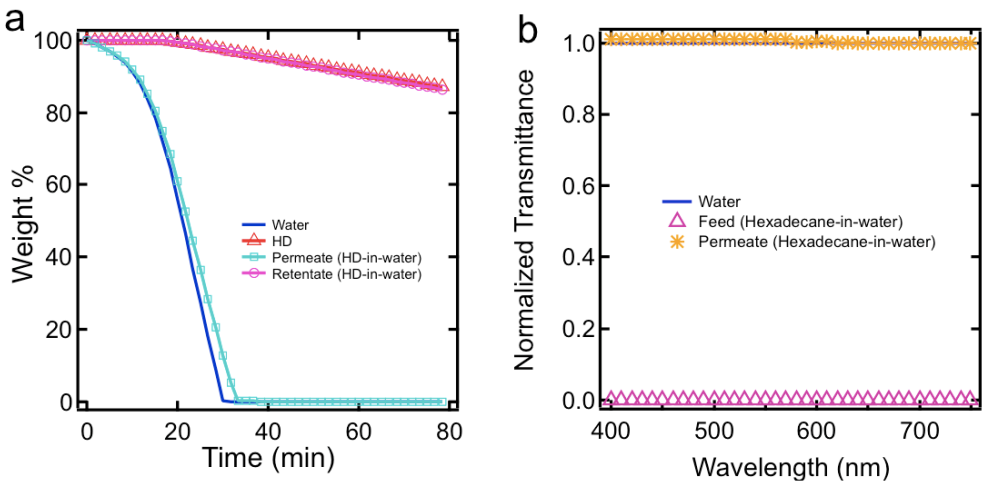

Figure 4.9 TGA and transmittance data. (a) TGA data for the permeate and the retentate obtained from the batch separation of hexadecane-in-water emulsion. (b) Transmittance data for hexadecane-in-water feed emulsion and the permeate after separation.

Figure 4.9a shows the TGA data for the hexadecane-rich retentate and the water-rich permeate obtained from the separation of hexadecane-in-water emulsion. The data for pure water and as-obtained hexadecane (HD) are also shown for comparison. The measurements show that the permeate contains ~ 0.1 wt% of hexadecane while the retentate contains ~ 0.1 wt% of water. We also conducted transmittance measurements to estimate the permeate (water-rich phase) quality relative to the feed emulsion. Figure 4.9b shows the transmittance of hexadecane-in-water feed emulsion (absorbance normalized to 1), the transmittance of the corresponding permeate, as well as, the

transmittance of pure water between 390 nm and 750 nm (visible spectrum). It is evident that the feed emulsion is very turbid, while the corresponding permeate is very clear. This indicates that our separation methodology leads to nearly complete separation.

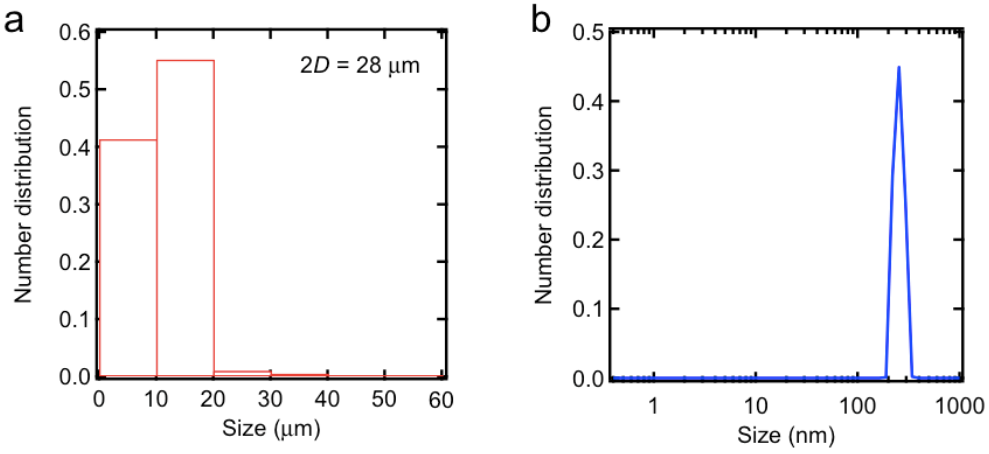

Figure 4.10 Number size distributions of the permeate. (a) and (b) The number size distributions of the permeate from the separation of the hexadecane-in-water emulsion obtained with optical image analysis and DLS, respectively.

Figures 4.10a and 10b show the number size distribution for the permeate obtained the separation of a hexadecane-in-water emulsion determined using image analysis and DLS, respectively. Comparing hexadecane-in-water feed emulsion with the permeate, it is evident that nearly all hexadecane droplets above 30 µm were removed during operation. However, the droplet size distribution below 1 µm remains unchanged during separation.

4.3.4.3.Separation of water-in-oil emulsion

Unlike oil-in-water emulsions, electric field driven separation of water-in-oil emulsions occurs through a combination of two different processes. First, water-in-oil

emulsions demulsify into water-rich and oil-rich phases via electrostatic coalescence[35,36]. Immediately after the onset of demulsification, the electric field driven preferential wettability transition of water over oil (similar to the separation of free oil and water) results in the complete separation of the water-rich and oil-rich phases.

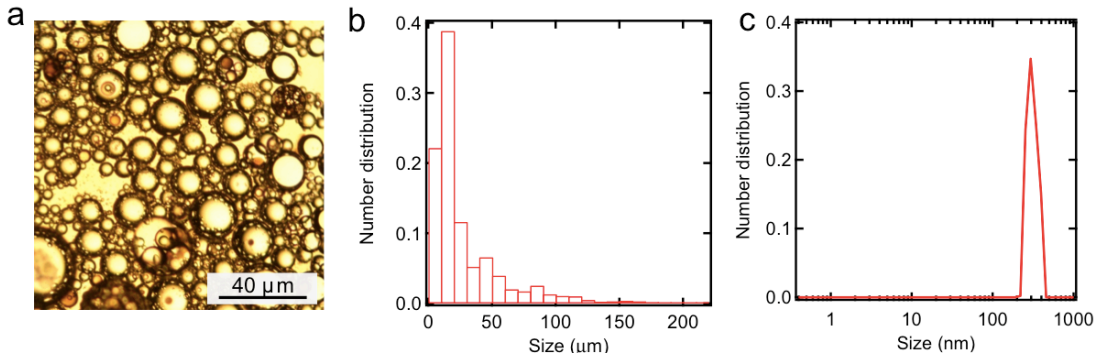

Figure 4.11 Size distributions of water droplets in the feed water-in-hexadecane emulsion. (a) A representative optical microscopy image of the feed emulsion. (b) and (c) The number size distributions for the feed emulsion for droplets > 1 µm and < 1 µm, respectively.

Figure 4.11a shows representative optical microscopy image for the 30:70 vol:vol span80 stabilized water-in-hexadecane emulsion. Figures 4.11b and 11c show the number size distributions of the dispersed phase determined using image analysis and DLS, respectively. The average size of dispersed phase is between 10-20 µm and 200-400 nm, respectively.

Similar to PS80, in the presence of span80, the macroscopic contact angle for hexadecane with 1.4 mg/mL span80 (γ_{lv} = 25.7 mN/m), $\theta^{ew}_{hexadecane}$ = 68°, is independent of V. Since span80 is virtually insoluble in water, the macroscopic contact angles for water

as a function of the voltage V applied across the dielectric layer are the same as those shown in figure 4.2a.

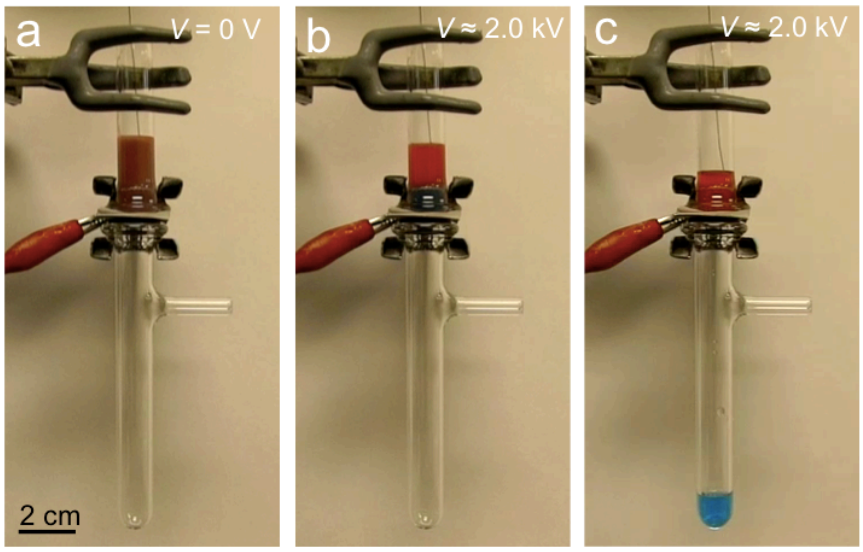

Figure 4.12 Separation of water-in-oil emulsion. (a) An apparatus with a liquid column of water-in-hexadecane emulsion above the membrane before applying an electric field. (b) The water-in-hexadecane emulsion is demulsified into the water-rich and the hexadecane-rich phases upon applying an electric field. (c) After the onset of demulsification, water-rich permeate passes through while hexadecane-rich retentate is retained when a voltage V ~ 2.0 kV is applied. Water is dyed blue and hexadecane is dyed red.

The membrane module and the electrode configuration are the same as those used for free oil and water, and oil-in-water emulsion separations. In the presence of span80, on non-textured 50 wt% fluorodecyl POSS + x-PDMS substrates, at V = 0 V, $\theta_{hexadecane}$ = 68° and θ_{water} = 115° (see Table 4.1). Using these values in equation 4.6, we estimate $P_{critical,hexadecane}$ = 708 Pa for the hexadecane-air interface (γ_{lv} = 25.7 mN/m) and $P_{critical,water}$ = 3540 Pa for the water-air interface (γ_{lv} = 72.1 mN/m). Before applying an

electric field, the dip-coated nylon membranes can support a 3 cm column of 30:70 vol:vol water-in-hexadecane emulsion because $P_{hydrostatic}$ = 247 Pa < $P_{critical,hexadecane}$ = 708 Pa (see figure 4.12a). Upon applying the electric field, water-in-hexadecane emulsion demulsifies into water-rich and hexadecane-rich phases due to electrostatic coalescence (see figure 4.12b). Immediately after the onset of demulsification, $P_{Maxwell}$ increases with increasing voltage, and at V = 2.2 kV, we calculate t_{eff} = 81.1 μm (see section 4.3.2.2), $P_{applied} \approx P_{critical,water}$. This matches well with our experimental observation of the permeation of water-rich phase through the membrane module at an applied voltage V = 2.0 ± 0.3 kV. After separation, the dip-coated nylon membranes can prevent the permeation of the hexadecane-rich phase (column height h = 2.1 cm) because $P_{hydrostatic}$ = 158 Pa < $P_{critical,hexadecane}$ = 708 Pa. TGA (figure 4.13a) and transmittance measurements (figure 4.13b) indicate that the permeate contains ~ 0.1 wt% hexadecane while the retentate contains ~ 0.1 wt% water.

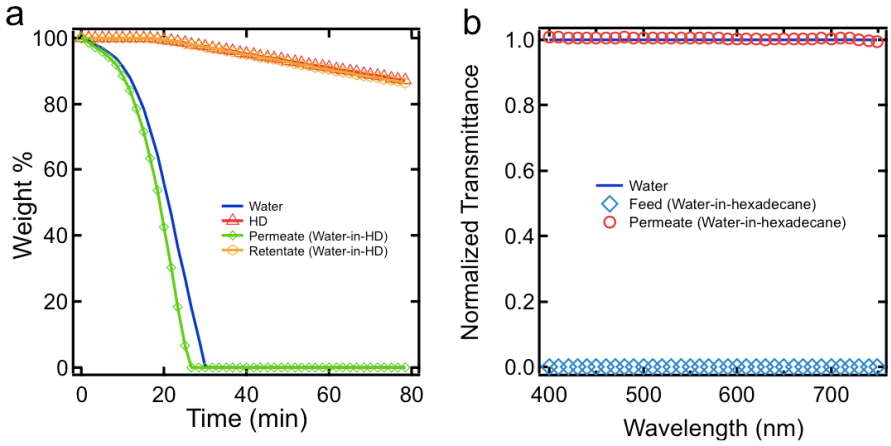

Figure 4.13 TGA and transmittance data. (a) TGA data for the permeate and the retentate obtained from the batch separation of water-in-hexadecane emulsion. (b) Transmittance data for water-in-hexadecane feed emulsion and the permeate after separation.

4.3.5. Continuous separation of water-in-oil emulsions

In the batch separation apparatus discussed above, continuous addition of water-in-oil feed emulsion leads to accumulation of oil above the membrane and oil will eventually permeate through the membrane when $P_{hydrostatic} > P_{critical,hexadecane}$. Therefore, we designed a continuous separation apparatus (see figure 4.14a) with two types of membrane modules operating in parallel – the membrane module shown in the schematic inset of figure 1g at the bottom, and a hydrophobic and oleophilic membrane ($2D$ = 37.5 μm, R = 12.5 μm, γ_{sv} = 35.6 mN/m) on the side-wall. The water-in-hexadecane feed emulsion is continuously fed by a syringe pump. On continuously applying a voltage V = 2.0±0.3 kV, water-rich phase permeates through the membrane module at the bottom. Simultaneously, hexadecane-rich phase accumulates in the apparatus and eventually permeates through the hydrophobic and oleophilic membrane on the sidewall. At steady-state, under an electric field, water-rich phase continuously permeates through the membrane module at the bottom, while the hexadecane-rich phase continuously permeates through the hydrophobic and oleophilic membrane on the sidewall as shown in figure 4.14a. TGA indicates that the water-rich permeate contains ~ 0.1 wt% hexadecane and the hexadecane-rich permeate contains ~ 0.1 wt% water (see figure 4.14b). Karl Fischer analysis[37,38] indicates that the hexadecane-rich permeate contains ~ 88 ppm water. Note that the solubility of water in hexadecane at room temperature is ~ 20-50 ppm[39,40].

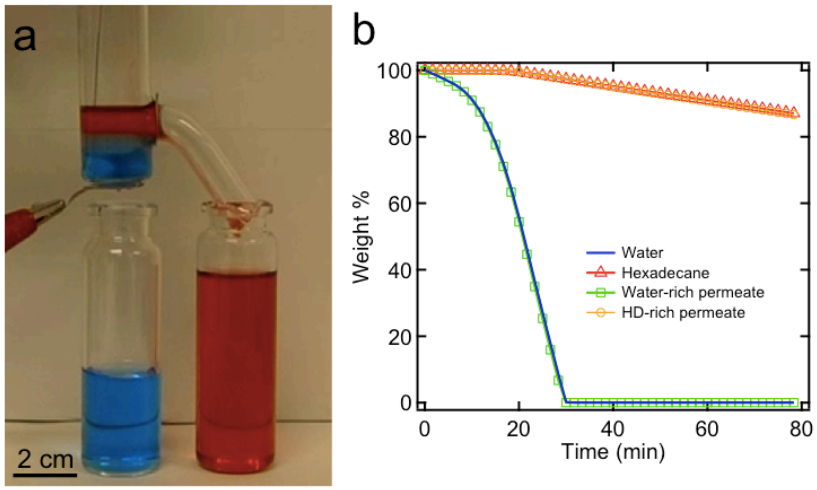

Figure 4.14 Continuous separation of water-in-hexadecane emulsion. (a) An apparatus used for continuous separation of water-in-hexadecane emulsion. Water-rich permeate passes through the membrane module at the bottom, while hexadecane-rich permeate passes through the hydrophobic and oleophilic membrane on the side-wall. (b) TGA data for the water-rich and the hexadecane-rich permeates. Water is dyed blue and hexadecane is dyed red.

We also computed the fraction of emulsified water droplets removed from water-in-hexadecane emulsions during the separation. Consider 100 mL of 30:70 v:v water-in-hexadecane feed emulsion containing 30 ml of water and 70 ml of hexadecane. We determined the volume fraction of emulsified water droplets (< 20 μm) in our feed emulsions to be 0.016 from the volume size distribution (see figure 4.15). Thus, the volume of emulsified water droplets in 100 mL of feed emulsion is 0.48 ml. In continuous separation, 100 ml of feed emulsion results in approximately 30 ml of water-rich permeate and 70 ml of hexadecane-rich permeate. Karl Fischer analysis indicates that the amount of water in the hexadecane-rich permeate is ~ 0.0088 wt%, which is equivalent to ~ 0.0068 vol%. Thus, the volume of water in the hexadecane-rich permeate

is 0.0047 ml. Even if we assume that the size of all the water droplets in the hexadecane-rich permeate is < 20 μm, comparing the volume of the emulsified water droplets in the feed emulsion (0.48 ml) to that in the hexadecane-rich permeate (0.0047 ml), we conclude that the volumetric fraction of emulsified droplets removed during separation is at least 99%. Flux for the water-rich permeate through the membrane was measured to be ≈ 200 L/m^2-h. This value is comparable to those reported in literature for other membranes[41-46].

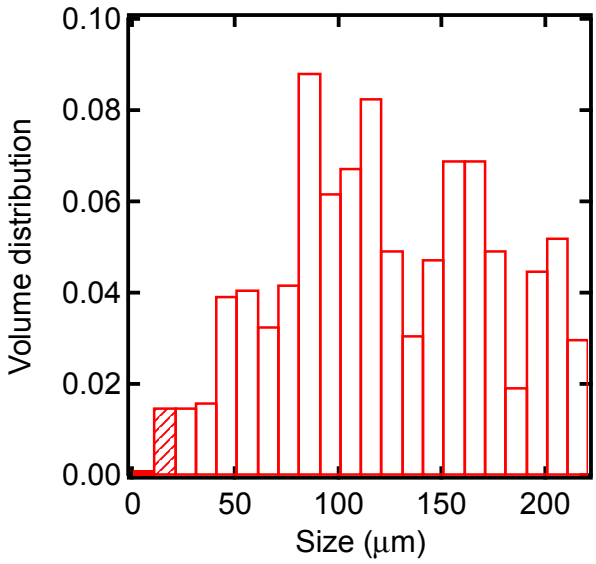

Figure 4.15 Volume size distribution of water droplets for the water-in-hexadecane feed emulsion. The dashed region represents droplets below 20 μm (emulsified droplets).

4.3.6. Location and concentration of the surfactant after oil-water emulsion separation

We estimated the amount of surfactant in the permeate and the retentate after emulsion separation by measuring the permeate and retentate contact angles and

comparing them with calibration curves of contact angles for water and hexadecane as a function of surfactant concentration. The calibration curves were developed by measuring the contact angles on flat surfaces spin-coated with a 50 wt% fluorodecyl POSS + x-PDMS blend. The 50 wt% fluorodecyl POSS + x-PDMS blend was chosen because it is essentially non-polar.

Figures 4.16a and 16b show the advancing and receding contact angles for water and hexadecane, respectively, as a function of PS80 concentration. After the batch separation of PS80 stabilized hexadecane-in-water emulsion, the advancing and receding contact angles for the water-rich permeate are 94º ± 2º and 64º ± 2º while those of hexadecane-rich retentate are 76º ± 2º and 63º ± 2º. By comparing these values with figures 4.16a and 4.16b, it is evident that the concentration of PS80 in the water-rich permeate is between 1.2-1.5 mg/ml and the concentration of PS80 in the hexadecane-rich retentate is 0-0.3 mg/ml. This is because of the higher solubility of PS80 in water when compared to hexadecane. In contrast to PS80, span80 is virtually insoluble in water. The advancing and receding contact angles for the water-rich permeates from the batch separation and the continuous separation of water-in-hexadecane emulsions are 123°±2° and 108°±2°, respectively. By comparing these values with those of water without any surfactant (see Table 4.1), it is evident that there is no span80 in the water-rich phase. Consequently, after separation of the water-in-hexadecane emulsions, we estimate that nearly all the span80 is in the hexadecane-rich phase.

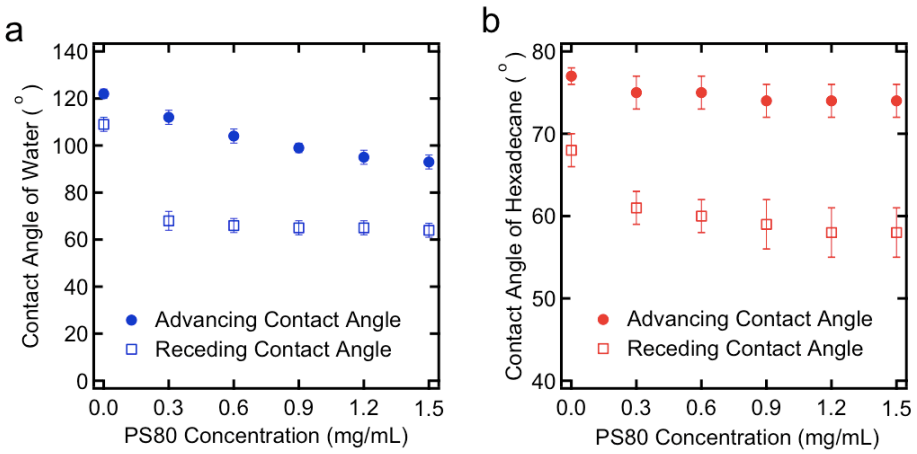

Figure 4.16 Location and concentration of surfactant after emulsion separation. (a) and (b) Advancing and receding contact angles for water and hexadecane, respectively, as a function of PS80 concentration.

4.4. Conclusion

In summary, we have developed the first-ever membrane-based unit operation that allows for electric field driven on-demand separation of various oil-water mixtures. Using our methodology, we demonstrated the on-demand separation of free oil and water, oil-in-water emulsions and water-in-oil emulsions, with ≥ 99.9% separation efficiency using a single membrane. The voltage required to trigger the separation was computed using a breakthrough pressure model that incorporates Maxwell stress and the hydrostatic pressure. The predictions from the model were found to match well with our experiments. The ease of scalability of the developed apparatus allowed us to separate larger quantities of oil-water emulsions. Finally, we have engineered a continuous oil-water emulsion separation apparatus that is triggered on-demand and removes > 99% of the emulsified droplets. We envision that our on-demand separation methodology will be useful for a wide range of applications such as clean up of oil-spills, fuel-purification, separation of a

range of commercial emulsions and waste-water treatment. Besides oil-water separation, it has other potential applications such as designing microfluidic valves that selectively allow one liquid to flow through while retaining the other. An array of such microfluidic valves would allow for the development of programmable liquid paths with precise control over the position or flux of the desired liquid in a lab on a chip device.

4.5. References

1 Kwon, G., Kota, A. K., Li, Y. X., Sohani, A., Mabry, J. M. & Tuteja, A. On-Demand Separation of Oil-Water Mixtures. *Adv Mater* **24**, 3666-3671, (2012).

2 Lippmann, M. G. Relation entre les phénomènes électriques et capillaires. *Ann. Chim. Phys.* **5**, 494-548, (1875).

3 Quilliet, C. & Berge, B. Electrowetting: a recent outbreak. *Curr Opin Colloid In* **6**, 34-39, (2001).

4 Berge, B. Electrocapillarity and Wetting of Insulator Films by Water. *Cr Acad Sci Ii* **317**, 157-163, (1993).

5 Mugele, F. & Baret, J. C. Electrowetting: From basics to applications. *J Phys-Condens Mat* **17**, R705-R774, (2005).

6 Gras, S. L., Mahmud, T., Rosengarten, G., Mitchell, A. & Kalantar-Zadeh, K. Intelligent control of surface hydrophobicity. *Chemphyschem* **8**, 2036-2050, (2007).

7 Shamai, R., Andelman, D., Berge, B. & Hayes, R. Water, electricity, and between ... On electrowetting and its applications. *Soft Matter* **4**, 38-45, (2008).

8 Fair, R. B. Digital microfluidics: is a true lab-on-a-chip possible? *Microfluid Nanofluid* **3**, 245-281, (2007).

9 Moon, H., Wheeler, A. R., Garrell, R. L., Loo, J. A. & Kim, C. J. An integrated digital microfluidic chip for multiplexed proteomic sample preparation and analysis by MALDI-MS. *Lab Chip* **6**, 1213-1219, (2006).

10 Barbulovic-Nad, I., Yang, H., Park, P. S. & Wheeler, A. R. Digital microfluidics for cell-based assays. *Lab Chip* **8**, 519-526, (2008).

11 Berge, B. & Peseux, J. Variable focal lens controlled by an external voltage: An application of electrowetting. *Eur Phys J E* **3**, 159-163, (2000).

12 Kilaru, M. K., Yang, J. & Heikenfeld, J. Advanced characterization of electrowetting retroreflectors. *Opt Express* **17**, 17563-17569, (2009).

13 Hayes, R. A. & Feenstra, B. J. Video-speed electronic paper based on electrowetting. *Nature* **425**, 383-385, (2003).

14 Heikenfeld, J., Zhou, K., Kreit, E., Raj, B., Yang, S., Sun, B., Milarcik, A., Clapp, L. & Schwartz, R. Electrofluidic displays using Young-Laplace transposition of brilliant pigment dispersions. *Nat Photonics* **3**, 292-296, (2009).

15 Manukyan, G., Oh, J. M., van den Ende, D., Lammertink, R. G. H. & Mugele, F. Electrical Switching of Wetting States on Superhydrophobic Surfaces: A Route Towards Reversible Cassie-to-Wenzel Transitions. *Phys Rev Lett* **106**, (2011).

16 Oh, J. M., Manukyan, G., van den Ende, D. & Mugele, F. Electric-field-driven instabilities on superhydrophobic surfaces. *Epl-Europhys Lett* **93**, (2011).

17 Krupenkin, T. N., Taylor, J. A., Wang, E. N., Kolodner, P., Hodes, M. & Salamon, T. R. Reversible wetting-dewetting transitions on electrically tunable superhydrophobic nanostructured surfaces. *Langmuir* **23**, 9128-9133, (2007).

18 Cassie, A. B. D. & Baxter, S. Wettability of porous surfaces. *T Faraday Soc* **40**, 0546-0550, (1944).

19 Wenzel, R. N. Resistance of solid surfaces to wetting by water. *Ind Eng Chem* **28**, 988-994, (1936).
20 Tuteja, A., Choi, W., Ma, M. L., Mabry, J. M., Mazzella, S. A., Rutledge, G. C., McKinley, G. H. & Cohen, R. E. Designing superoleophobic surfaces. *Science* **318**, 1618-1622, (2007).
21 Ahuja, A., Taylor, J. A., Lifton, V., Sidorenko, A. A., Salamon, T. R., Lobaton, E. J., Kolodner, P. & Krupenkin, T. N. Nanonails: A simple geometrical approach to electrically tunable superlyophobic surfaces. *Langmuir* **24**, 9-14, (2008).
22 Choi, W., Tuteja, A., Chhatre, S., Mabry, J. M., Cohen, R. E. & McKinley, G. H. Fabrics with Tunable Oleophobicity. *Adv Mater* **21**, 2190-2195, (2009).
23 Kota, A. K., Kwon, G., Choi, W., Mabry, J. M. & Tuteja, A. Hygro-responsive membranes for effective oil-water separation. *Nat Commun* **3**, (2012).
24 Mabry, J. M., Vij, A., Iacono, S. T. & Viers, B. D. Fluorinated polyhedral oligomeric silsesquioxanes (F-POSS). *Angew Chem Int Edit* **47**, 4137-4140, (2008).
25 Young, T. An essay on the cohesion of fluids. *Philosophical Transactions of the Royal Society of London* **95**, 65, (1805).
26 Buehrle, J., Herminghaus, S. & Mugele, F. Interface profiles near three-phase contact lines in electric fields. *Phys Rev Lett* **91**, (2003).
27 Mugele, F. & Buehrle, J. Equilibrium drop surface profiles in electric fields. *J Phys-Condens Mat* **19**, (2007).
28 Klarman, D., Andelman, D. & Urbakh, M. A Model of Electrowetting, Reversed Electrowetting, and Contact Angle Saturation. *Langmuir* **27**, 6031-6041, (2011).
29 Herminghaus, S. Roughness-induced non-wetting. *Epl-Europhys Lett* **79**, (2007).
30 Marmur, A. Wetting on hydrophobic rough surfaces: To be heterogeneous or not to be? *Langmuir* **19**, 8343-8348, (2003).
31 Tuteja, A., Choi, W., Mabry, J. M., McKinley, G. H. & Cohen, R. E. Robust omniphobic surfaces. *P Natl Acad Sci USA* **105**, 18200-18205, (2008).
32 Batchelor, G. K. *An Introduction in Fluid Dynamics*. (Cambridge University Press, 1970).
33 Tadmor, R. Line energy and the relation between advancing, receding, and young contact angles. *Langmuir* **20**, 7659-7664, (2004).
34 Fowkes, F. M. Attractive Forces at Interfaces. *Ind Eng Chem* **56**, 40-&, (1964).
35 Elektorowicz, M., Habibi, S. & Chifrina, R. Effect of electrical potential on the electro-demulsification of oily sludge. *J Colloid Interf Sci* **295**, 535-541, (2006).
36 Eow, J. S. & Ghadiri, M. Drop-drop coalescence in an electric field: the effects of applied electric field and electrode geometry. *Colloid Surface A* **219**, 253-279, (2003).
37 Garcia-Perez, M., Wang, S., Shen, J., Rhodes, M., Lee, W. J. & Li, C. Z. Effects of temperature on the formation of lignin-derived oligomers during the fast pyrolysis of Mallee woody biomass. *Energ Fuel* **22**, 2022-2032, (2008).
38 Margolis, S. A. Amperometric Measurement of Moisture in Transformer Oil Using Karl-Fischer Reagents. *Anal Chem* **67**, 4239-4246, (1995).
39 Schatzberg, P. Solubilities of Water in Several Normal Alkanes from C7 to C16. *J Phys Chem-Us* **67**, 776-779, (1963).

40 Schatzbe.P. Diffusion of Water through Hydrocarbon Liquids. *J Polym Sci Pol Sym*, 87-92, (1965).
41 Koltuniewicz, A. B., Field, R. W. & Arnot, T. C. Cross-Flow and Dead-End Microfiltration of Oily-Water Emulsion .1. Experimental-Study and Analysis of Flux Decline. *J Membrane Sci* **102**, 193-207, (1995).
42 Hlavacek, M. Break-up of Oil-in-Water Emulsions Induced by Permeation through a Microfiltration Membrane. *J Membrane Sci* **102**, 1-7, (1995).
43 Sun, D. Z., Duan, X. D., Li, W. X. & Zhou, D. Demulsification of water-in-oil emulsion by using porous glass membrane. *J Membrane Sci* **146**, 65-72, (1998).
44 Arnot, T. C., Field, R. W. & Koltuniewicz, A. B. Cross-flow and dead-end microfiltration of oily-water emulsions - Part II. Mechanisms and modelling of flux decline. *J Membrane Sci* **169**, 1-15, (2000).
45 Maartens, A., Jacobs, E. P. & Swart, P. UF of pulp and paper effluent: membrane fouling-prevention and cleaning. *J Membrane Sci* **209**, 81-92, (2002).
46 Hu, B. & Scott, K. Influence of membrane material and corrugation and process conditions on emulsion microfiltration. *J Membrane Sci* **294**, 30-39, (2007).

CHAPTER 5

Energy-efficient separation of miscible components using hygro-responsive membranes

5.1. Introduction

Separation of miscible components from a liquid mixture is crucial in various industries, including the oil refining industry. For example, crude oil processing includes fractionation and the separation of miscible impurities such as sulfur, nitrogen and metal compounds[1]. Similarly, high quality biofuels, such as bioethanol or biodiesel, can be produced by removing methanol and water byproducts, which are completely miscible[2]. In addition, recovery of acids from agroindustrial wastewater is important not only for environmental requirements, but also for economic benefits[3,4].

Distillation is one of the most widely used separation methods for separating miscible components from a liquid mixture[5] by utilizing the differences in boiling points between the various mixture components[6]. However, distillation has a high energy-cost, being a thermally driven process[5]. Further, it is unsuitable for the separation of components with similar boiling points and azeotropes[6].

Liquid-liquid extraction, also known as solvent extraction, is typically used to separate azeotropes or components with overlapping boiling points when simple distillation cannot be used[7,8]. It transfers components from one phase to another based on the solubility differences of the components between the two phases[9]. Typically, two immiscible liquid phases are involved in the liquid-liquid extraction process. The solution whose components are to be separated is the feed, whereas the liquid contacting the feed for the purpose of extraction is termed the extractant[7,9,10]. In the liquid-liquid extraction process, components dissolved in the feed are extracted into the extractant[7-9].

For an efficient extraction of components, maximizing contact between the feed and the extractant is critical. This is typically accomplished by energy-intensive techniques such as ultrasonication[11], or pumping the feed and the extractant through columns with moving internals, or using packed columns with high tortuosity[12] and high resistance to fluid flow. A relatively less energy-intensive technique is emulsification of the feed and the extractant[13,14]. While emulsions, especially those stabilized by surfactants, provide a large interfacial area and greatly enhance the mass transfer in extraction[13-15], the subsequent separation of emulsions can be energy-intensive and less economical[16-22]. Consequently, there is a great need and a significant opportunity to develop a new energy-efficient separation methodology with enhanced mass transfer during extraction and facile separation of the surfactant-stabilized emulsion.

In this work, we have developed a novel energy-efficient separation methodology that combines liquid-liquid extraction using surfactant-stabilized emulsions, and solely-gravity driven (i.e., without any external energy) separation of these emulsions into a single unit operation, using membranes with hygro-responsive surfaces[23]. We also

demonstrate the separation of various miscible liquid mixtures, including the separation of an ethanol-heptane azeotrope, as well as, miscible impurities from oils. We anticipate that our separation methodology has numerous applications, including the production of diesel with ultra-low sulfur content, separation and purification of bio-fuels, removal of dyes from jet fuels and separation of azeotropes.

5.2. Experimental Procedure

5.2.1. Materials

Cellulose-based filter papers (nominal pore size ≈ 25 μm and 2.5 μm) and wipe were obtained from Whatman and Contec, respectively. Heptadecafluoro-1,1,2,2-tetrahydrodecyl triethoxysilane and n-octadecyltrichlorosilane were obtained from Gelest. N,N-dimethyl formamide (DMF), methanol, ethanol and toluene were obtained form Fischer Scientific. Heptane was obtained from J.T.Baker. Hexadecane was obtained from Alfa Aesar. Dodecane, n-butanol, n-hexanol were obtained from Sigma Aldrich. N-octanol was obtained from Acros Organics. Disperse Red 1, Methyl Oleate, Benzothiophene and 2-Methyl-2-propanethiol (t-butyl thiol), poly(methyl methacrylate) (PMMA) were obtained from Sigma Aldrich. Methylene blue (blue dye), oil red-o (red dye), sodium dodecyl sulphate (SDS) were obtained from Fisher Scientific. Asahiklin AK-225 was obtained from Structure Probe, Inc.

5.2.2. Hygro-responsive membrane preparation

Cellulose-based filter papers and wipes were treated using oxygen plasma for 5 min and subsequently exposed to vapor phase heptadecafluoro-1,1,2,2-tetrahydrodecyl triethoxysilane for 20 h at room temperature (~ 22 °C).

5.2.3. Conventional hydrophobic and oleophilic membrane preparation

5.2.3.1. Membranes used for the separation of dye (or sulfur compounds) and for the separation of methanol

A solution (2.5 mg/ml) of n-octadecyltrichlorosilane was prepared in toluene. Cellulose-based filter papers (nominal pore size ≈ 25 μm) were dip-coated in the solution for 30 min and dried with nitrogen gas at room temperature (~ 22 °C) for 5 min. Dip-coated filter papers were then baked at 70 ºC in an oven for 2 h followed by thorough rinsing with ethanol. These filter papers allow dodecane and methyl oleate to permeate through while preventing permeation of DMF and water.

5.2.3.2. Membranes used for the separation of ethanol from ethanol-heptane azeotrope

A solution (10 mg/ml) of poly(methylmethacrylate) (PMMA) was prepared in Asahiklin AK-225. Cellulose-based filter papers (nominal pore size ≈ 25 μm) were dip-coated in the solution for 30 min and dried with nitrogen gas at room temperature (~ 22 °C) for 5 min.

5.2.4. Characterization techniques

5.2.4.1. Contact angle measurements

All measurements of contact angle were conducted using a Ramé–Hart 200-F1 goniometer. All contact angles reported in this work were measured by advancing or receding a small volume of liquid (~2 μl) onto the surface using a 2 ml micrometer syringe (Gilmont). At least three measurements were performed on each substrate. The typical error in measurements was ±2°.

5.2.4.2. Microscopy

The surface morphology of the membranes was characterized using a Hitachi SU8000 scanning electron microscope at 10 kV. Optical microscopy of prepared emulsion was conducted using an Olympus BH-2 optical microscope.

5.2.4.3. Refractive index measurements

Refractive index measurements were conducted using a Reichert r2i300 refractometer. A few drops of liquid sample (~ 300 µl) were applied. At least five measurements were performed to minimize errors. All measurements were performed at room temperature (~ 22 ± 0.1 °C). The typical error in measurements was ± 0.0002.

5.2.4.4. UV-Vis spectroscopy

The dye (Disperse Red 1) or benzothiophene content in the dodecane-rich phases after separation were measured using a Cary 50 Bio UV-Vis spectrophotometer. The UV-Vis absorbance of the dodecane-rich phase was obtained and compared with calibration curves.

5.2.4.5. Separation efficiency

The methanol content in the hexadecane-rich phase and the hexadecane content in the methanol-rich phase after separation were measured using a Perkin Elmer Pyris 1 TGA. Approximately 60 mg of a sample was heated from room temperature to 300 °C at a rate of 10 °C/min, and the temperature was held constant at 300 °C for 40 min. Note that the boiling point of hexadecane is 287 °C. The loss in weight of the hexadecane-rich phase was compared with the loss in weight of the as-obtained hexadecane to estimate the purity of the hexadecane-rich phase. Similarly, the loss in weight of the methanol-rich

phase was compared with the loss in weight of the as-obtained methanol to estimate the purity of the methanol-rich phase.

The t-butyl thiol content in the dodecane-rich phase after separation was measured by injecting samples ranging in volume from 1-10 μL into a Gas Chromatography-Mass Spectroscopy (GC-MS) instrument.

5.3. Results and discussion

5.3.1. Wetting behavior of polar and non-polar liquids

The membranes employed in this work are fabricated by controlled silanization of cellulose-based filter papers or wipes with heptadecafluoro-1,1,2,2-tetrahydrodecyl triethoxysilane (see section 5.2.2.). These membranes possess hygro-responsive surfaces (i.e., surfaces that respond to the contacting liquid) and are systematically designed based on the design parameters discussed in our previous work[24-26]. Controlled silanization of cellulose-based filter papers can create a thin layer of covalently bonded perfluorinated groups on the membrane surface[27,28]. Consequently, it allows for a robust and homogeneous coating on the membrane's surface without clogging the pores[28].

When a non-polar liquid (virtually any oil) droplet contacts our membrane, it cannot permeate through and displays a high apparent contact angle (θ^*). For example, the advancing apparent contact angles for hexadecane and dodecane are $\theta^*_{hexadecane,adv}$ = 104º and $\theta^*_{dodecane,adv}$ = 95º, respectively, on our membrane fabricated using a 2.5 μm pore size cellulose-based filter paper (see figure 5.1a). In addition, those angles on a membrane fabricated using a cellulose-based wipe are $\theta^*_{hexadecane,adv}$ = 132º and $\theta^*_{dodecane,adv}$

= 115º (see figure 5.1b). This is due to a combination of the re-entrant texture of the membranes (see insets in figures 5.1a and 5.1b) and the low surface energy of the perfluorinated groups on the surface[29-31]. In contrast, when a polar liquid (virtually any protic or aprotic solvent that can hydrogen bond) droplet contacts our membrane, it completely wets the surface and permeates through (see figures 5.1a and 5.1b). This is due to the hydrogen bonding and dipole-dipole interactions between the polar liquid and the cellulose-based membrane surface.

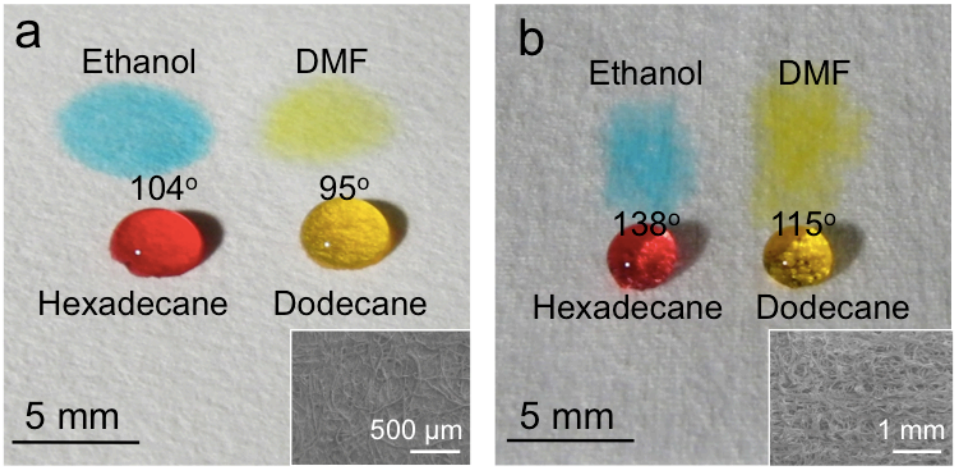

Figure 5.1 Wetting behavior of polar and non-polar liquids. (a) and (b) Droplets of ethanol (dyed blue), DMF (dyed green), hexadecane (dyed red) and dodecane (dyed yellow) on the hygro-responsive membranes fabricated using a cellulose-based filter paper (nominal pore size = 2.5 µm) and a wipe, respectively. Insets, morphologies of the respective filter paper and wipe surfaces.

5.3.2. Time of wetting as a function of Hansen solubility parameters

Hansen solubility parameters have been mainly used in the coatings industry as a practical tool for predicting thermodynamic and transport properties in polymer systems[32-35]. In addition, Hansen solubility parameters have direct application in surface

science where they have been used to characterize surfaces wettability[36-39]. The basis of Hansen solubility parameters is that the total cohesive energy of a liquid arises from three interactions: dispersive, dipole-dipole and hydrogen boding interactions[32]. Consequently there are three components in Hansen solubility parameters. These are δ_d (dispersive), δ_p (polar) and δ_h (hydrogen bonding) components.

We measured the time of wetting for a series of alcohols on our membranes (see figure 5.2). We define the time of wetting as the time required for a polar liquid droplet to imbibe into the membrane. A polar liquid, with higher values for polar and hydrogen bonding components in Hansen solubility parameters, readily wets the surface and permeate through our membranes, as is evident from the decreased time of wetting for a series of alcohols (see figure 5.2). This indicates that wettability of polar liquids on our membrane surface is induced by a combination of hydrogen bonding and polar interactions.

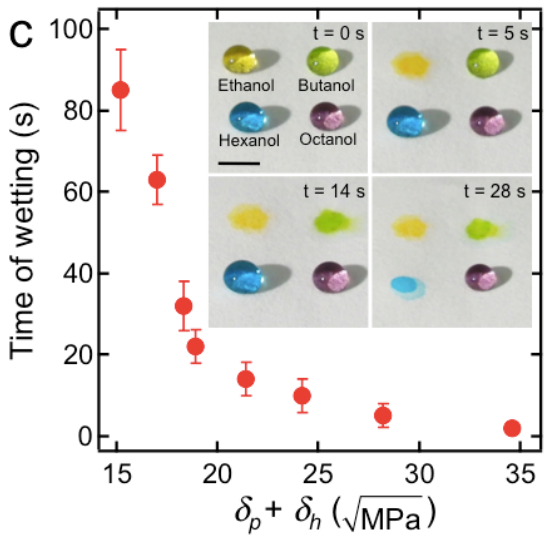

Figure 5.2 Time of wetting. Time of wetting for a series of alcohols on the hygro-responsive membranes shown in figure 5.1a. Insets show sequential wetting of four alcohol droplets in the order of decreasing the sum of polar and hydrogen bonding components of Hansen solubility parameters.

5.3.3. Batch separations of liquid mixtures

5.3.3.1. Batch separation of methanol-hexadecane mixture

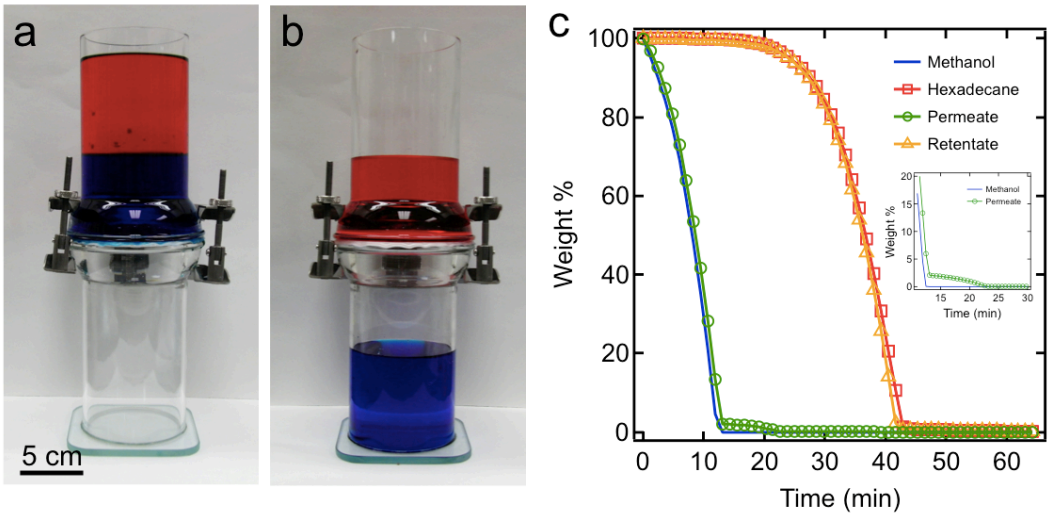

Figure 5.3 Batch separation of methanol and hexadecane mixture. (a) A batch separation apparatus with 50:50 v:v methanol-hexadecane mixture above the membrane. (b) Methanol-rich permeate passes through the membrane while hexadecane-rich phase is retained. Methanol is dyed blue and hexadecane is dyed red. (c) TGA data for the methanol-rich permeate and hexadecane-rich retentate. TGA data for as obtained methanol and hexadecane are also shown for comparison. Inset shows methanol-rich permeate contains ≈ 2 wt% hexadecane.

As might be expected, the preferential wettability of our membranes by polar liquids over non-polar liquids can be used to separate mixtures of immiscible polar and non-polar liquids. Figures 5.3a and 5.3b show the batch separation of a 50:50 v:v methanol (polar liquid) and hexadecane (non-polar liquid) mixture. Our membrane (nominal pore size ≈ 2.5 μm) is sandwiched between the glass tubes (see figure 5.3a), and the liquid mixture is added to the upper glass tube. After a few minutes, the methanol-rich phase permeates through the membrane whereas hexadecane-rich retentate is retained above the membrane (see figure 5.3b). After separation, the compositions of

methanol-rich permeate and hexadecane-rich retentate are measured using thermogravimetric analysis (TGA). TGA indicates that methanol-rich permeate contains ≈ 2 wt% hexadecane, while hexadecane-rich retentate contains ≈ 0.1 wt% methanol (see figure 5.3c). These values are close to the mutual solubilities for methanol and hexadecane reported in literatures[40]. Note that TGA detection limit used in this measurement is 0.1 wt%.

5.3.3.2. Batch separation of oil-soluble dye from dodecane

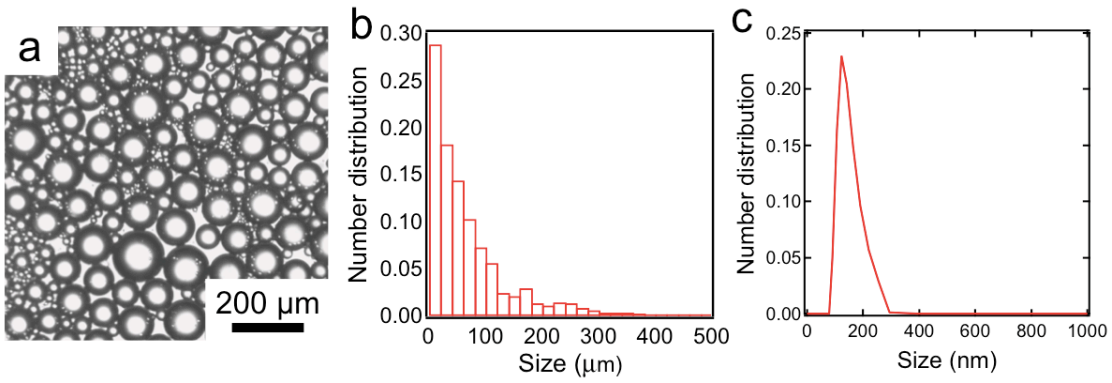

Figure 5.4 Size distribution of dodecane droplets in the 50:50 v:v dodecane-in-DMF feed emulsion. (a) A representative optical microscopy image of feed emulsion. (b) and (c) The number size distributions of the feed emulsion for droplets > 1 µm and < 1 µm, respectively.

Our hygro-responsive membranes are capable of separating immiscible polar and non-polar liquid mixtures, solely under gravity (see section 5.3.3.1.), but the separation of miscible polar and non-polar liquids is not trivial. In order to separate miscible components, we utilized liquid-liquid extraction with surfactant-stabilized emulsions, leading to enhanced mass transfer[13-15]. As an example, we illustrated the batch separation

of an oil-soluble red dye, Disperse Red 1, from dodecane using dimethyl formamide (DMF) as an extractant and sodium dodecyl sulfate (SDS) as the surfactant.

Figure 5.4a shows a representative optical image for the 50:50 vol:vol SDS-stabilized dodecane-in-DMF feed emulsion. We determined the size distributions of the dispersed phase in feed emulsion using two techniques – optical microscopy image analysis for droplets above 1 μm in diameter and dynamic light scattering (DLS) for droplets below 1 μm. Figure 5.4b shows the number size distribution of the dodecane droplets determined using image analysis. The average size of the dispersed phase is between 1–20 μm. Figure 5.4c shows the number size distribution of the dodecane droplets, determined using DLS. The size varies between 100 – 300 nm.

Our batch separation apparatus (see figure 5.5a) is the same as used in the separation of methanol-hexadecane mixtures (see section 5.3.3.1.) with a 2.5 μm nominal pore size membrane. Dodecane containing the dye (20 ppm) is emulsified with DMF using SDS as the surfactant. The emulsion is added to the upper tube (see figure 5.5.a). Within a few minutes, our hygro-responsive membrane allows the dye-enriched DMF phase to permeate through solely under gravity, while preventing the permeation of the dye-depleted dodecane phase (see figure 5.5b). After separation, the dye-depleted dodecane phase retained above the membrane is almost perfectly transparent, indicating effective extraction.

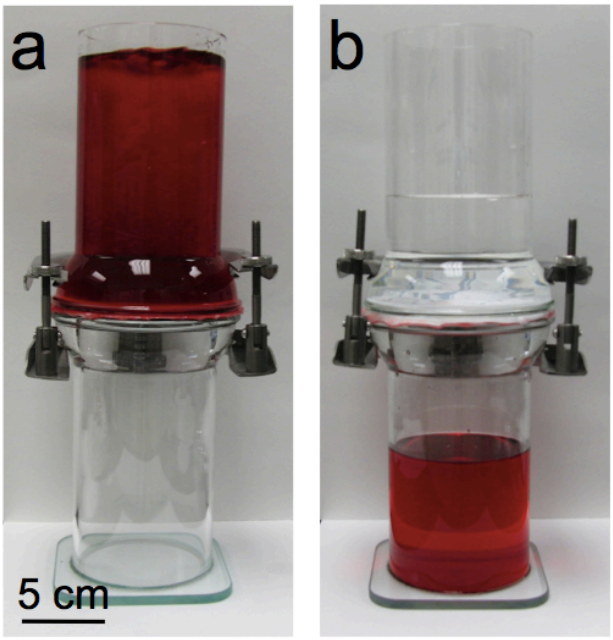

Figure 5.5 Batch separation of the dye (Disperse Red 1). (a) A batch separation apparatus with 50:50 v:v dodecane-in-DMF emulsion above the membrane. (b) Dye-enriched DMF phase permeates through the membrane while dye-depleted dodecane phase is retained.

5.3.4. Continuous separation methodology

In the batch separation operation described in the previous sections, the retentate will continue to accumulate above the membrane, eventually breakthrough the membrane. In order to overcome the shortcomings of batch separation and make our separation methodology practical, we developed a continuous separation methodology that combines emulsification-enhanced extraction and hygro-responsive membrane-based separation into a single unit operation. The continuous separation apparatus (see figure 5.6a) consists of a chamber where the feed and the extractant with dissolved surfactant are continuously fed using syringe pumps. We adopted a gravity-driven countercurrent flow with the lower density liquid fed from the bottom of the chamber and the higher

density liquid fed from the top of the chamber. The feed and the extractant phases are emulsified in-situ in the chamber by a mechanical stirrer. The chamber is also equipped with two membranes operating in parallel – a hygro-responsive membrane and a conventional hydrophobic and oleophilic membrane. While the hygro-responsive membrane allows a polar liquid to pass through and prevents the permeation of a non-polar liquid, the conventional membrane allows a lower surface tension liquid (e,g., dodecane, γ_{lv} = 25.4 mN/m) to pass through and prevents the permeation of a higher surface tension liquid (e.g., DMF, γ_{lv} = 37.1 mN/m). Note that the membrane separation occurs continuously and simultaneously along with emulsification and extraction.

5.3.4.1. Separation of oil-soluble dye (Disperse Red 1) from dodecane

Using our continuous separation methodology, dye (Disperse Red 1) is separated from dodecane (see figure 5.6a). Dodecane containing 30 ppm dye is continuously fed from the bottom of the chamber, while DMF with dissolved SDS is continuously fed from the top of the chamber using syringe pumps. Here, SDS is chosen as the surfactant because it is immiscible with dodecane (the desired phase). During operation, the polar dye-enriched DMF phase continuously permeates through the hygro-responsive membrane at the bottom, while the dye-depleted dodecane phase with lower surface tension continuously permeates through the conventional hydrophobic and oleophilic membrane on the side–wall.

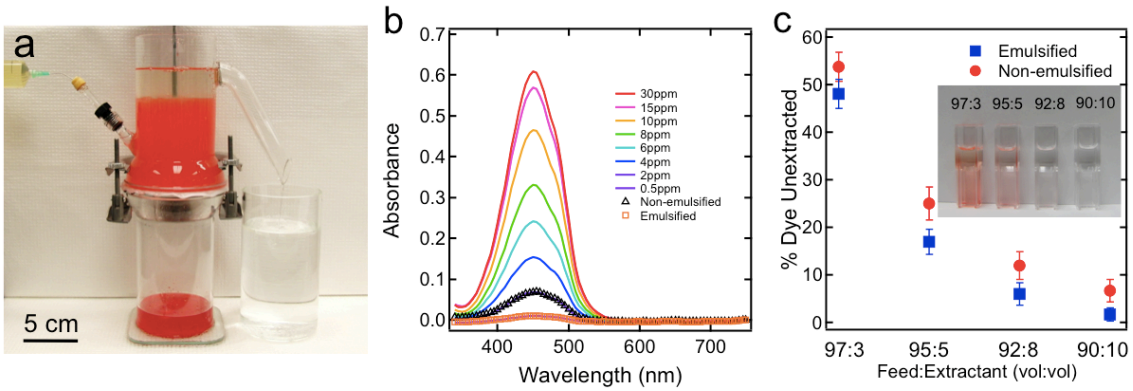

Figure 5.6 Continuous separation of dye (Disperse Red 1). (a) An apparatus used for continuous separation of dye using SDS-stabilized dodecane-in-DMF emulsion. (b) UV-Vis absorbance data for the dodecane phases obtained from continuous separations with and without emulsification, using a 90:10 feed:extractant volumetric flow rates. (c) The % dye unextracted from dodecane after separations using different feed:extractant volumetric flow rates. Inset shows the dodecane phase after separations.

UV-Vis absorbance measurements indicate that the dye-depleted dodecane phase contains ≤ 0.5 ppm of dye (see figure 5.6b). Further, it is also evident that the purity of the permeate after surfactant-enhanced extraction increases 300% compared to that from a separation without the surfactant (see figure 5.6b). This is a direct consequence of enhanced mass transfer of the dye due to the increased interfacial area between the feed (dodecane) and the extractant (DMF) in the emulsion. In order to understand their difference in more detail, we measured and compared percentages of the dye remaining in the emulsified feed with those obtained from separations without surfactant, using various ratios of feed:extractant volumetric flow rates. Figure 5.6c shows % dye unextracted from dodecane as a function of feed:extractant volumetric flow rates. It is

evident that the emulsification of the feed and the extractant leads to a more efficient extraction of the dye for a given feed:extractant volumetric flow rates.

5.3.4.2. Separation of methanol from methyl oleate

Biodiesel, a renewable and biodegradable source of energy, is considered an appropriate alternative to fossil fuels[41]. The most common way to produce biodiesel is through transesterification, where vegetable oils or animal fats are chemically reacted with alcohols[42-44]. The reaction produces a new chemical compound called methyl ester (i.e., biodiesel) and byproducts, including glycerol and excess methanol[42-44]. After the reaction, methyl ester must be purified from glycerol and other by-products[45,46]. Although glycerol can be easily separated from biodiesel through centrifugation or decantation, because of its poor solubility and significant density difference[45,47], the separation of methanol requires energy-intensive operations such as vacuum distillation[45,48].

We demonstrate the separation of methanol from methyl oleate using water as the extractant and SDS as the surfactant. Here we utilize methyl oleate as a representative of biodiesel. Methyl oleate containing 10 vol% of methanol is continuously fed from the bottom of the chamber, while water with dissolved SDS is continuously fed from the top of the chamber to achieve a gravity-driven countercurrent flow. The feed (i.e., methyl oleate containing 10 vol% methanol) and the extractant (water with dissolved SDS) phases are emulsified in-situ in the chamber using a mechanical stirrer. The methanol-enriched aqueous phase continuously permeates through the hygro-responsive membrane at the bottom, while the methanol-depleted methyl oleate phase continuously permeates through the conventional hydrophobic and oleophilic membrane on the side-wall.

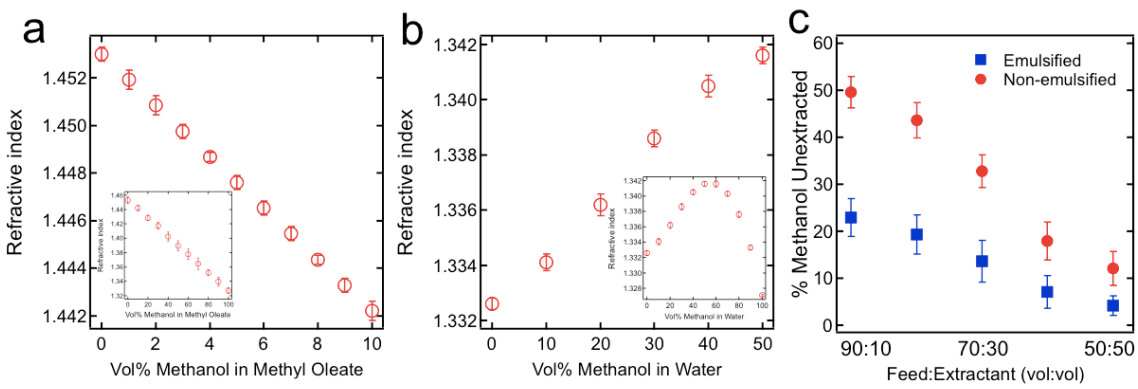

Figure 5.7 Continuous separation of methanol from methyl oleate. (a) Refractive index data for methyl oleate as a function of methanol concentration (0–10 vol%). (b) Refractive index data for water as a function of methanol concentration (0–50 vol%). Insets show calibration curves of refractive index for methyl oleate and water as a function of methanol concentrations (0–100 vol%). (c) The % methanol unextracted from methyl oleate as a function of feed:extractant volumetric flow rates.

The amount of methanol in the dodecane phase was determined by measuring its refractive index and comparing it with calibration curves of refractive index. The calibration curves were developed by measuring refractive index of methyl oleate with different vol % methanol. Figure 5.7a shows the refractive index of methyl oleate as a function of methanol concentration.

First, consider the methanol-depleted methyl oleate phase using a 90:10 feed:extractant volumetric flow rate. The refractive index of the methanol-depleted methyl oleate phase is 1.4503±0.0002. By comparing this with figure 5.7a, it is evident that the concentration of methanol in the methyl oleate phase after separation is ≈ 2.5 vol%. On the other hand, the refractive index of the methanol-depleted methyl oleate phase obtained from the continuous separation without emulsification is 1.4471±0.0003

yielding ≈ 5.5 vol%. This clearly indicates that extraction using surfactant-stabilized emulsion facilitates more efficient removal of methanol from the methyl oleate phase.

The amount of methanol in aqueous phase was also determined by measuring the refractive index and comparing it with calibration curves developed by measuring refractive index of water with different vol % methanol. Figure 5.7b shows the refractive index of water as a function of methanol concentration.

Consider the aqueous phase from continuous separation of SDS-stabilized methyl oleate-in-water emulsion using a 90:10 feed:extractant volumetric flow rate. The refractive index of the methanol-enriched aqueous phase is 1.3406±0.0002. By comparing this with figure 5.7b, the concentration of methanol in the aqueous phase is ≈ 41 vol%. The methanol-enriched aqueous phase obtained from the continuous separation without emulsification. It is found to be 1.3388±0.0001, corresponding to ≈ 31 vol% methanol in water (see figure 5.7b). Again, this indicates that a larger amount of methanol is extracted by using surfactant-stabilized emulsion.

Refractive indices of the methyl oleate-rich and aqueous phases after continuous separations, with emulsification and without emulsification, using various feed:extractant volumetric flow rates are listed in Table 5.1. These values were found to match well with our calculated mass balance.

Figure 5.7c shows % methanol unextracted from continuous separations as a function of feed:extractant volumetric flow rates based on the refractive index measurements. It also supports that emulsification of the feed and the extractant enhances efficient removal of methanol from the feed for a given feed:extractant volumetric flow rate.

The total energy consumption to obtain purified methyl oleate, through the removal of methanol, using our methodology was compared with that of conventional distillation. First, consider continuous separation of methanol from methyl oleate using our methodology. After separation, we obtain the methanol-depleted methyl oleate phase through a conventional hydrophobic and oleophilic membrane, while the methanol-enriched aqueous phase is obtained through a hygro-responsive membrane. Our methodology requires electric energy to pump the feed and the extractant into the chamber using syringe pumps as well as emulsify them using a mechanical stirrer. We calculated the required electric energy to obtain 1 kg of methyl oleate, to be 144 kJ. In addition to the electric energy for pumping and emulsifying the feed and extractant, we need to consider the energy for recycling the extractant (water). In order to address this, we assume that water is recovered by removing methanol through distillation; it being the most commonly used method. Based on previous literature[49], we calculated the energy required, to distill methanol from the aqueous phase, to be 180 kJ. Thus, the total energy required to obtain 1 kg of methyl oleate using our methodology is 324 kJ. This value is lower than that required to obtain the same amount of pure methyl oleate using distillation without liquid-liquid extraction of methanol. In the previous literature[50], it varies between 445 – 6977 kJ. Thus, our methodology can be very useful for energy efficient during biodiesel purification.

Table 5.1. Measured refractive indices for the methanol-depleted dodecane phases and the methanol-enriched aqueous phases during continuous separations using different feed:extractant volumetric flow rates.

Feed:Extractant (vol:vol)	Refractive index			
	Methyl Oleate phase		Aqueous phase	
	Emulsification	Non-emulsification	Emulsification	Non-emulsification
90:10	1.4503	1.4471	1.3407	1.3388
80:20	1.4507	1.4478	1.3374	1.3358
70:30	1.4514	1.4490	1.3355	1.3347
60:40	1.4521	1.4508	1.3345	1.3343
50:50	1.4525	1.4515	1.3339	1.3336

5.3.4.3. Separation of ethanol-heptane azeotrope

Liquid-liquid extraction is a useful alternative for the separation of azeotropes (i.e., constant boiling mixtures), which cannot be separated by simple distillation[7,8,10]. Effective separation of oil and alcohol mixtures, including azeotropes, is necessary in numerous areas including biodiesel production[41,42,47], edible oils refining[51,52] and petrochemical industries[1,53].

Here, we demonstrate the separation of an ethanol-heptane azeotrope (49:51 wt:wt ethanol:hepane)[54] using water as an extractant and SDS as a surfactant. SDS is chosen as the surfactant because it is immiscible with heptane (the desired phase). The

ethanol-heptane azeotrope is continuously fed from the bottom of the chamber, while water with dissolved SDS is continuously fed from the top of the chamber to achieve a gravity-driven countercurrent flow. The feed (i.e., ethanol-heptane azeotrope) and the extractant (water with dissolved SDS) phases are emulsified in-situ using a mechanical stirrer. The ethanol-enriched aqueous phase continuously permeates through the hygro-responsive membrane at the bottom, while the ethanol-depleted, heptane-rich phase continuously permeates through the conventional hydrophobic and oleophilic membrane on the side-wall.

The amount of ethanol remaining in the heptane-rich phase after continuos separations is determined by measuring its refractive index and comparing it with calibration curves developed by measuring refractive index of heptane with different concentrations of ethanol (figure 5.8a). Because water is virtually insoluble in heptane, the refractive index of the ethanol-depleted heptane phase obtained from the separation can be directly compared with that of ethanol-heptane mixture.

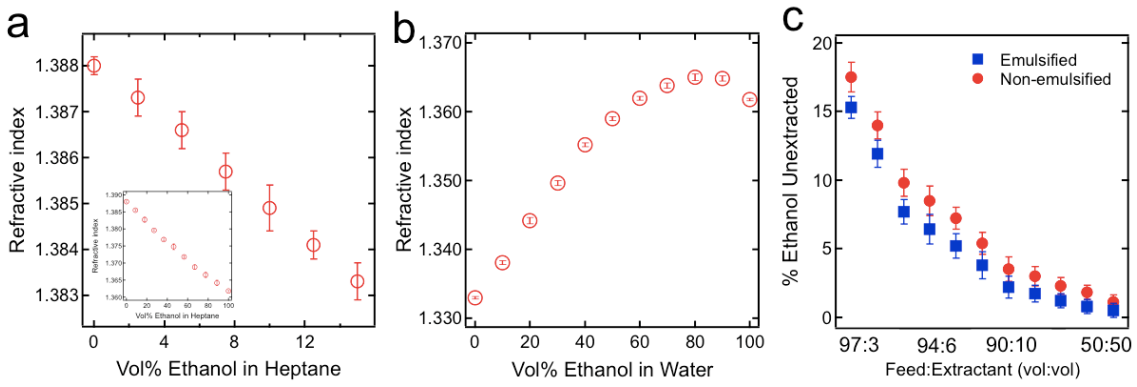

Figure 5.8 Continuous separation of ethanol from the ethanol-heptane azeotrope. (a) Refractive index data for heptane as a function of ethanol concentration (0–16 vol%). Inset shows calibration curves of refractive index for heptane as a function of ethanol concentration (0–100 vol%). (b) Refractive index data for water as a function of ethanol

concentration (0–100 vol%). (c) The % ethanol unextracted from ethanol-heptane azeotrope as a function of feed:extractant volumetric flow rates.

First, consider the ethanol-depleted heptane phase obtained from the continuous separation of SDS-stabilized emulsion using a 50:50 feed:extractant volumetric flow rate. The refractive index of the ethanol-depleted heptane phase is 1.3879±0.0001. By comparing this with figure 5.8a, the concentration of ethanol is ≈ 0.4 vol%. By contrast, the refractive index of the ethanol-depleted heptane phase obtained from the continuous separation without emulsification is 1.3877±0.0001 and corresponds to ≈ 1.0 vol% ethanol in heptane.

Similar to the separation of methanol from methyl oleate (see section 5.3.4.2.), extracted ethanol is transferred into the extractant (i.e., water). We determined the amount of ethanol in the aqueous phase after continuous separation by measuring its refractive index and comparing it with calibration curves developed by measuring refractive index of water with different concentrations of ethanol shown in figure 5.8b.

Consider the aqueous phase from continuous separation of SDS-stabilized emulsion using a 50:50 feed:extractant volumetric flow rate. The refractive index of the ethanol-enriched aqueous phase is 1.3502±0.0002. By comparing this with figure 5.8b, the concentration of ethanol in the aqueous phase is ≈ 31 vol%. We also measured the refractive index of the ethanol-enriched aqueous phase obtained from the continuous separation without emulsification. It was 1.3497±0.0002 yielding ≈ 31 vol% ethanol in heptane. Refractive indices of the ethanol-depleted heptane phase and the aqueous phase after continuous separation, with emulsification and without emulsification, using various

feed:extractant volumetric flow rates are listed in Table 5.2. These values were found to match well with our calculation, based on the overall mass balance for the system.

Figure 5.8c shows % ethanol unextracted from separations as a function of feed:extractant volumetric flow rates. It shows that < 1 % ethanol remains in the ethanol-heptane azeotrope after continuous separation of SDS-stabilized emulsion using a 50:50 feed:extractant volumetric rato. It is evident that emulsification of the feed and the extractant leads to more efficient removal of ethanol from the feed for a given feed:extractant volumetric flow rate.

Table 5.2. Measured refractive indices for the ethanol-depleted heptane phase and the ethanol-enriched aqueous phase during continuous separations using different feed:extractant volumetric flow rates.

Feed:Extractant (vol:vol)	Refractive index			
	Heptane phase		Aqueous phase	
	Emulsification	Non-emulsification	Emulsification	Non-emulsification
97:3	1.3840	1.3835	1.3640	1.3641
96:4	1.3849	1.3844	1.3647	1.3647
95:5	1.3860	1.3854	1.3650	1.3650
94:6	1.3865	1.3858	1.3648	1.3647
92:8	1.3868	1.3862	1.3649	1.3648
91:9	1.3871	1.3868	1.3649	1.3649
90:10	1.3874	1.3871	1.3650	1.3650
80:20	1.3876	1.3873	1.3629	1.3628
70:30	1.3877	1.3875	1.3593	1.3590
60:40	1.3878	1.3876	1.3552	1.3550
50:50	1.3879	1.3877	1.3502	1.3497

5.3.4.4. Separation of sulfur compounds from dodecane

With tighter environmental regulations and government mandates, there is a significant push towards removing sulfur compounds from fuels, including gasoline and diesel[55,56]. Hydrodesulfurization[57,58] is the most widely used technology in petroleum refineries for removing sulfur compounds from oils. However, it is energy-intensive due to operation at elevated temperatures and pressures[57-59].

Here, we demonstrate the separation of two sulfur compounds, benzothiophene and 2-Methyl-2-propanethiol (t-butyl thiol), from dodecane using DMF as an extractant and SDS as a surfactant. We utilize dodecane as a representative oil. Dodecane containing 30 ppm benzothiophene (or 50 ppm t-butyl thiol) is continuously fed from the bottom of the chamber while DMF with dissolved SDS is continuously fed from the top of the chamber using syringe pumps. SDS is chosen as the surfactant because it is immiscible with dodecane (the desired phase). The feed (i.e., dodecane containing benzothiophene or t-butyl thiol) and the extractant (i.e., DMF with dissolved SDS) phases are emulsified in-situ in the chamber using a mechanical stirrer. The polar sulfur compound-enriched DMF phase continuously permeates through the hygro-responsive membrane at the bottom, while the sulfur compound-depleted dodecane phase with lower surface tension, continuously permeates through the conventional hydrophobic and oleophilic membrane on the side-wall.

Benzothiophene in the dodecane phase was quantified after separation by measuring the absorbance and comparing it with calibration curves developed by measuring absorbances of dodecane with different concentrations of benzothiophene.

Figure 5.9a shows the absorbance of dodecane as a function of benzothiophene concentration.

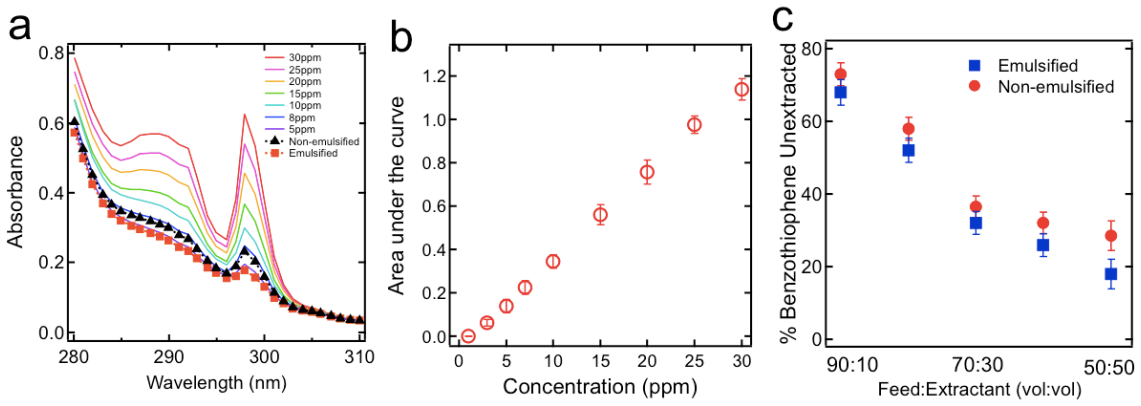

Figure 5.9 Continuous separation of benzothiophene. (a) UV-Vis absorbance data for the benzothiophene-depleted dodecane phases obtained from continuous separations with and without emulsification, using a 50:50 feed:extractant volumetric flow rates. UV-Vis absorbance data for dodecane with different benzothiophene concentration are also shown for comparison. (b) A plot of calculated area under the UV-Vis absorbance curves as a function of benzothiophene concentration. (c) The % benzothiophene unextracted from dodecane as a function of feed:extractant volumetric flow rates.

Consider the benzothiophene-depleted dodecane obtained from continuous separation of SDS-stabilized dodecane-in-DMF emulsion using a 50:50 feed:extractant volumetric flow rate. The absorbance data for the benzothiophene-depleted dodecane is shown in figure 5.9a. By comparing the permeate spectrum with the known concentration curves, the concentration of benzothiophene in the dodecane after separation is found to be ≈ 5 ppm. By contrast, the absorbance data for the benzothiophene-depleted dodecane phase obtained from the continuous separation without emulsification shown in figure 5.9a indicates that ≈ 8 ppm benzothiophene remains in the dodecane phase. Thus, a larger

amount of benzothiophene is extracted from the feed using surfactant-stabilized emulsion, as is clear in figure 5.9a.

For a quantitative study, we developed another calibration curve by calculating the area under the UV-Vis absorbance curves in figure 5.9a. Figure 5.9b shows area under the UV-Vis absorbance curves for dodecane as a function of benzothiophene concentration. The calculated area under the UV-Vis absorbance curves for benzothiophene-depleted dodecane after continuous separation of SDS-stabilized dodecane-in-DMF emulsion using a 50:50 feed:extractant volumetric flow rate is 0.168. By comparing this with figure 5.9b, the concentration of benzothiophene in dodecane is ≈ 5.4 ppm. By contrast, the area under the UV-Vis absorbance curves of the dodecane phase obtained from the continuous separation without emulsification is 0.296 and is equivalent to ≈ 8.6 ppm benzothiophene (see figure 5.9b). Values of area under the UV-Vis absorbance curves for the benzothiophene-depleted dodecane phase after continuous separations, with emulsification and without emulsification, using various feed:extractant volumetric flow rates are listed in Table 5.3. Figure 5.9c shows % benzothiophene unextracted as a function of feed:extractant volumetric flow rate.

Gas Chromatography-Mass Spectroscopy (GC-MS) measurements were used to determine the amount of t-butyl thiol in the dodecane phase after separations. Small sample volumes (ranging from 1-10 μL) are injected into the GC-MS instrument and the peak areas determined the t-butyl thiol concentrations. The concentration of t-butyl thiol in the dodecane phase after continuous separation of SDS-stabilitzed dodecane-in-DMF emulsion using a 50:50 feed:extractant ratio is 21.5 ppm (see Table 5.4), while 23.5 ppm t-butyl thiol remains in the dodecane phase without emulsification. Concentration values

of t-butyl thol in the dodecane-rich phases after continuous separations, with emulsification and without emulsification, using various feed:extractant volumetric flow rates are listed in Table 5.4.

Table 5.3. Calculated the area under the UV-Vis absorbance curves for benzothiphene-depleted dodecane phases obtained from continuous separations with and without emulsification using different feed:extractant volumetric flow rates.

Feed:Extractant (vol:vol)	Area under the curves	
	Emulsification	Non-emulsification
90:10	0.767	0.827
80:20	0.575	0.647
70:30	0.336	0.388
60:40	0.264	0.336
50:50	0.168	0.296

Table 5.4. The concentrations of t-butyl thiol in the dodecane phases obtained from continuous separations with and without emulsification using different feed:extractant volumetric flow rates.

Feed:Extractant (vol:vol)	Concentration of t-butyl thiol (ppm)	
	Emulsification	Non-emulsification
90:10	44.0	45.0
80:20	37.5	39.0
70:30	30.5	32.3
60:40	25.3	27.0
50:50	21.5	23.5

5.4. Conclusion

We have developed an extremely energy-efficient, single unit operation that combines (a) liquid-liquid extraction using surfactant-stabilized emulsions, and (b) solely-gravity driven (i.e., without any external energy) separation of these emulsions using hygro-responsive membranes to separate miscible components from liquid mixtures. We have demonstrated that our methodology is applicable to a wide range of separations, including separation of miscible dye, alcohol and sulfur compounds from oils and separation of an ethanol-heptane azeotrope. We anticipate that our technology is readily scalable and can be directly incorporated into many mainstream commercial operations such as the production of diesel with ultra-low sulfur content, separation and recovery of bio-fuels, removal of dyes from jet fuels and separation of azeotropes.

5.5. Reference

1 Meyers, R. A. *Handbook of Petroleum Refining Processes*. (McGraw-Hill, 2004).

2 Birgit Kamm, P. R. G., Michael Kamm. *Biorefineries - industrial processes and products*. (Wiley-VCH, 2006).

3 Yu, L. X., Guo, Q. F., Hao, J. H. & Jiang, W. J. Recovery of acetic acid from dilute wastewater by means of bipolar membrane electrodialysis. *Desalination* **129**, 283-288, (2000).

4 Hong, Y. K. & Hong, W. H. Removal of acetic acid from aqueous solutions containing succinic acid and acetic acid by tri-n-octylamine. *Sep Purif Technol* **42**, 151-157, (2005).

5 Oak Ridge National Laboratory & BCS, I. *Materials Research for Separations Technologies: Energy and Emission Reduction Opportunities*. (2005).

6 Kister, H. *Distillation Operation*. 1 edn, (McGraw-Hill Professional, 1990).

7 Shri Ramaswamy, H.-J. H., Bandaru V. Ramarao. *Separation and Purification Technologies in Biorefineries*. (Wiley, 2013).

8 Treybal, R. E. *Mass-Transfer Operations*. (McGraw-Hill Book Company, 1980).

9 Louis Theodore, F. R. *Mass Transfer Operations for the Practicing Engineer*. (Wiley-AIChE, 2011).

10 Treybal, R. E. *Liquid Extraction*. (Nabu Press, 2011).

11 Delgado-Povedano, M. M. & de Castro, L. Ultrasound-assisted analytical emulsification-extraction. *Trac-Trend Anal Chem* **45**, 1-13, (2013).

12 Gabelman, A. & Hwang, S. T. Hollow fiber membrane contactors. *J Membrane Sci* **159**, 61-106, (1999).

13 Kralj, J. G., Schmidt, M. A. & Jensen, K. F. Surfactant-enhanced liquid-liquid extraction in microfluidic channels with inline electric-field enhanced coalescence. *Lab Chip* **5**, 531-535, (2005).

14 Huebner, A., Sharma, S., Srisa-Art, M., Hollfelder, F., Edel, J. B. & Demello, A. J. Microdroplets: A sea of applications? *Lab Chip* **8**, 1244-1254, (2008).

15 Jablonski, E. L. in *2013 AlChe Annual Meeting.*

16 Lennie, S., Halling, P. J. & Bell, G. Causes of Emulsion Formation during Solvent-Extraction of Fermentation Broths and Its Reduction by Surfactants. *Biotechnol Bioeng* **35**, 948-950, (1990).

17 Chabrand, R. M., Kim, H. J., Zhang, C., Glatz, C. E. & Jung, S. Destabilization of the emulsion formed during aqueous extraction of soybean oil. *J Am Oil Chem Soc* **85**, 383-390, (2008).

18 Kundu, P. & Mishra, I. M. Removal of emulsified oil from oily wastewater (oil-in-water emulsion) using packed bed of polymeric resin beads. *Sep Purif Technol* **118**, 519-529, (2013).

19 Maartens, A., Jacobs, E. P. & Swart, P. UF of pulp and paper effluent: membrane fouling-prevention and cleaning. *J Membrane Sci* **209**, 81-92, (2002).

20 Feng, L., Zhang, Z. Y., Mai, Z. H., Ma, Y. M., Liu, B. Q., Jiang, L. & Zhu, D. B. A super-hydrophobic and super-oleophilic coating mesh film for the separation of oil and water. *Angew Chem Int Edit* **43**, 2012-2014, (2004).

21 Yuan, J. K., Liu, X. G., Akbulut, O., Hu, J. Q., Suib, S. L., Kong, J. & Stellacci, F. Superwetting nanowire membranes for selective absorption. *Nat Nanotechnol* **3**, 332-336, (2008).
22 Hu, B. & Scott, K. Influence of membrane material and corrugation and process conditions on emulsion microfiltration. *J Membrane Sci* **294**, 30-39, (2007).
23 Marmur, A. From hygrophilic to superhygrophobic: Theoretical conditions for making high-contact-angle surfaces from low-contact-angle materials. *Langmuir* **24**, 7573-7579, (2008).
24 Kota, A. K., Kwon, G., Choi, W., Mabry, J. M. & Tuteja, A. Hygro-responsive membranes for effective oil-water separation. *Nat Commun* **3**, (2012).
25 Choi, W., Tuteja, A., Chhatre, S., Mabry, J. M., Cohen, R. E. & McKinley, G. H. Fabrics with Tunable Oleophobicity. *Adv Mater* **21**, 2190-2195, (2009).
26 Tuteja, A., Choi, W., Mabry, J. M., McKinley, G. H. & Cohen, R. E. Robust omniphobic surfaces. *P Natl Acad Sci USA* **105**, 18200-18205, (2008).
27 Wang, M. J., Liechti, K. M., Wang, Q. & White, J. M. Self-assembled silane monolayers: Fabrication with nanoscale uniformity. *Langmuir* **21**, 1848-1857, (2005).
28 Ulman, A. Formation and structure of self-assembled monolayers. *Chem Rev* **96**, 1533-1554, (1996).
29 Chhatre, S. S., Guardado, J. O., Moore, B. M., Haddad, T. S., Mabry, J. M., McKinley, G. H. & Cohen, R. E. Fluoroalkylated Silicon-Containing Surfaces-Estimation of Solid-Surface Energy. *Acs Appl Mater Inter* **2**, 3544-3554, (2010).
30 Meuler, A. J., Chhatre, S. S., Nieves, A. R., Mabry, J. M., Cohen, R. E. & McKinley, G. H. Examination of wettability and surface energy in fluorodecyl POSS/polymer blends. *Soft Matter* **7**, 10122-10134, (2011).
31 Liu, K. S., Tian, Y. & Jiang, L. Bio-inspired superoleophobic and smart materials: Design, fabrication, and application. *Prog Mater Sci* **58**, 503-564, (2013).
32 Hansen, C. M. *Hansen Solubility Parameters: A User's Handbook*. (CRC Press, 2007).
33 Hansen, C. M. 50 Years with solubility parameters - past and future. *Prog Org Coat* **51**, 77-84, (2004).
34 Hansen, C. M. Cohesion parameters for surfaces, pigments, and fillers. *Jocca-Surf Coat Int* **80**, 386-391, (1997).
35 Vink, P. & Bots, T. L. Formulation parameters influencing self-stratification of coatings. *Prog Org Coat* **28**, 173-181, (1996).
36 Hansen, C. M. & Wallstrom, E. On the Use of Cohesion Parameters to Characterize Surfaces. *J Adhesion* **15**, 275-286, (1983).
37 Hansen, C. M. & Pierce, P. E. Surface Effects in Coatings Processes. *Ind Eng Chem Prod Rd* **13**, 218-225, (1974).
38 Hansen, C. M. Surface Dewetting and Coatings Performance. *J Paint Technol* **44**, 57-60, (1972).
39 Hansen, C. M. Characterization of Surfaces by Spreading Liquids. *J Paint Technol* **42**, 660-664, (1970).
40 Won, D. B., Park, S. J., Han, K. J. & Kim, C. J. Liquid-liquid equilibria for methanol plus hexadecane plus heterocyclic nitrogen-containing compounds at 298.15 K. *Fluid Phase Equilibr* **193**, 217-227, (2002).

41 Gerhard Knothe, J. V. G. *The Biodiesel Handbook*. (AOCS Publishing, 2010).
42 Ma, F. R. & Hanna, M. A. Biodiesel production: a review. *Bioresource Technol* **70**, 1-15, (1999).
43 Meher, L. C., Sagar, D. V. & Naik, S. N. Technical aspects of biodiesel production by transesterification - a review. *Renew Sust Energ Rev* **10**, 248-268, (2006).
44 Kiss, A. A. & Bildea, C. S. A review of biodiesel production by integrated reactive separation technologies. *J Chem Technol Biot* **87**, 861-879, (2012).
45 Atadashi, I. M., Aroua, M. K. & Aziz, A. A. Biodiesel separation and purification: A review. *Renew Energ* **36**, 437-443, (2011).
46 Berrios, M. & Skelton, R. L. Comparison of purification methods for biodiesel. *Chem Eng J* **144**, 459-465, (2008).
47 Van Gerpen, J. Biodiesel processing and production. *Fuel Process Technol* **86**, 1097-1107, (2005).
48 Kiss, A. A. & Ignat, R. M. Enhanced methanol recovery and glycerol separation in biodiesel production - DWC makes it happen. *Appl Energ* **99**, 146-153, (2012).
49 Abolpour, B., Abolpour, R., Shamseddini, A., Kamyabi, S. & Hamzehee, F. Optimization of the reflux ratio for methanol-water stage distillation column. *Res Chem Intermediat* **39**, 681-692, (2013).
50 Bipro Ranjan Dhar, K. K. Excess methanol recovery in biodiesel production process using a distillation column: A simulation study. *Chemical Engineering Research Bulletin* **13**, 55-60, (2000).
51 Wolf Hamm, R. J. H., Gijs Calliauw. *Edible Oil Processing*. (Wiley-Blackwell, 2013).
52 Gupta, M. K. *Practical Guide to Vegetable Oil Processing*. (AOCS Publishing, 2010).
53 Meyers, R. *Handbook of Petrochemicals Production Processes*. (McGraw-Hill 2004).
54 Barbara Kanegsberg, E. K. *Handbook for Critical Cleaning: Cleaning Agents and Systems*. (CRC Press, 2011).
55 Song, C. S. An overview of new approaches to deep desulfurization for ultra-clean gasoline, diesel fuel and jet fuel. *Catal Today* **86**, 211-263, (2003).
56 Babich, I. V. & Moulijn, J. A. Science and technology of novel processes for deep desulfurization of oil refinery streams: A review. *Fuel* **82**, 607-631, (2003).
57 Vasudevan, P. T. & Fierro, J. L. G. A review of deep hydrodesulfurization catalysis. *Catal Rev* **38**, 161-188, (1996).
58 Schuit, G. C. A. & Gates, B. C. Chemistry and Engineering of Catalytic Hydrodesulfurization. *Aiche J* **19**, 417-438, (1973).
59 Toshiaki Kabe, W. Q., Atsushi Ishihara. *Hydrodesulfurization and Hydrodenintrogenation: Chemistry and Engineering*. (Wiley-VCH, 1999).

CHAPTER 6

Summary and Future Outlook

6.1. Thesis Summary

The main objective of my thesis was to develop smart separation methodologies for separating a wide variety of both immiscible and miscible liquid mixtures. Numerous technologies have been widely used in separation operations. Membrane-based separation technologies are extremely promising because they are energy-efficient, cost-effective and applicable to a wide range of industrial effluents. My thesis work focuses primarily on the membrane-based separation technologies, and it explores the systematic design of membranes as well as the development of smart separation methodologies for separating both immiscible and miscible liquid mixtures.

The development of membranes that can separate oil-water mixtures, solely under gravity, is the first topic of my thesis. The separation of oil-water mixtures is crucial in various fields for: wastewater treatment, fuel purification and the production of freshwater. Although membrane-based technologies have been used in these applications, their broad application remains limited. In the first part of my thesis, we developed novel membranes with hygro-responsive surfaces, which are both superhydrophilic and

superoleophobic. These membranes are oleophobic both in air and when submerged underwater. Utilizing these membranes, we developed capillary force-based separation (CFS) methodology that can separate a range of different oil-water mixtures, solely under gravity (i.e., without consuming external energy), with > 99% efficiency. Our separation methodology is solely gravity-driven and consequently is expected to be highly energy-efficient. We also engineered an apparatus using two simultaneous CFS-based operations in parallel, to achieve continuous, solely gravity-driven separation of oil-water emulsions, with a separation efficiency > 99.9%.

In the following part, we demonstrated that controlled silanization of cellulose-based filter papers can create a robust and homogeneous, hygro-responsive coating on the filter surface. This hygro-responsive coating can be applied to filters having pore sizes as small as 10 nm. These membranes were found to have unique "self-cleaning" ability as water displaces oil from the membrane surface. This allows the membranes to be extremely fouling resistant. We also demonstrated that our membranes can separate surfactant-stabilized oil-in-water emulsions with oil droplets as small as 10 nm in diameter.

In the CFS methodology, the onset of water permeation takes place as soon as water contacts the membrane. Therefore, the third part of my thesis focuses on developing a separation methodology where the separation is triggered on-demand, i.e., upon applying an electric field. For effective on-demand separation of oil-water mixtures with an electrical stimulus, both water and oil must be retained above the membrane before an electric field is applied. We have developed hydrophobic and oleophobic membranes that support both oil and water above the membrane. Utilizing these

membranes, we developed a separation methodology that allows for gravity-driven, on-demand separation of various oil-water mixtures, including those stabilized by surfactant. The voltage required to trigger the separation was computed using a breakthrough pressure model incorporating the Maxwell stress and hydrostatic pressure. The predictions from the model were found to match well with our experiments. We also engineered a continuous oil-water emulsion separation apparatus that removes > 99% of the emulsified drops.

In the final part of my thesis, we developed a new separation methodology combining liquid-liquid extraction, using surfactant-stabilized emulsions, with solely gravity-driven separation of these emulsions into a single unit operation. We demonstrated that our methodology is applicable to a wide range of separations, including separation of miscible dye, alcohols and sulfur compounds from oils as well as separation of an alcohol-hydrocarbon azeotrope.

6.2. Future Outlook

Commercializing smart methodologies: In this thesis work, we developed several methodologies for efficient separation of liquid mixtures. We believe that our smart separation methodologies have immediate applications including biofuel purification and wastewater treatment. For example, biodiesel is an important and environmentally sustainable alternative to crude oil with an annual production of 1,359 million gallons in the United States in 2013[1]. As described in Chapter 5, we estimated that our smart methodology saves ~ 120 kJ per 1 kg of biodiesel in the purification process. Thus, by replacing conventional purification processes with our smart methodology, we expect

that about ~ 170,000 MWh of energy can be saved. This energy savings is equivalent to ~ $17 million USD, provided that $100 /MWh is the utility rate[2].

Another application is for wastewater treatment. About 40 billion gallons of wastewater is treated per day in the United States[3]. According to the Environmental Protection Agency, an estimated $200 billion is invested in publicly owned treatment works, of which at least 10% is for wastewater treatment[4]. Our hygro-responsive membranes can be directly used in wastewater treatment. In chapter 3, we estimated that our hygro-responsive membrane-based methodology can separate oil-water emulsions using about 30 % less energy than the conventional wastewater treatment process. Replacing them with our solely gravity-driven, hygro-responsive membrane-based separation methodology can virtually eliminate many costs and may lead to savings on the order of millions of dollars. Due to such economic merit and environmental impact, as well as ease of scalability, we envision that our smart separation methodologies can be commercialized.

Separation of water-in-oil microemulsion: The difficulties in separating the oil-water mixtures rely heavily on the dispersed phase size. Typically, microemulsions have less than 200 nm diameter droplets[5]. The stability of the mixtures is greatly enhanced by the addition of surfactants, which decreases interfacial tension and hinders the collisions necessary for droplet coalescence and gravity separation. As described in Chapter 2., the flux of water-rich permeate is impractically low for fine emulsions with water droplets smaller than 5 μm in diameter. In such cases, another technique, such as electrostatic coalescence is useful[6]. However, for complete oil–water separation, it is typically

followed by either skimming or gravity based separation. Hydrophilic and oleophobic sponge consisting of x-PEGDA and fluorodecyl POSS, considered in my thesis work, can overcome this limitation. This sponge is expected to absorb fine water droplets while repelling oil. Consequently, it leads to effective removal of water from oil with minimal oil loss.

Development of flux enhanced membranes: For an effective separation, the pore size is typically comparable to smaller than the dispersed phase diameter[7]. However, as the pore diameter decreases, viscous resistance to fluid flow through a membrane's pores increases and consequently, the flux decreases. It is evident from the Hagen-Poiseuille relation that the flux decrease is inversely proportional to the thickness of the membrane, all other parameters being held constant. Consequently, an ideal membrane is expected to have a separation layer as thin as possible to maintain both high flux and selectivity. Thickness of the x-PEGDA and fluorodecyl POSS film can be readily controlled by changing the coating conditions. Such a film can be incorporated onto backing membranes, with larger pores, to enhance mechanical durability.

6.3. References

1 Monthly Biodiesel Production Report. *U.S. Energy Information Administration* U.S. Department of Energy, (2014).

2 Annual Energy Outlook 2012. *Energy Information Administration* DOE/EIA-0383, (2012).

3 Willis, J. L. ENERGY and INFRASTRUCTURE. *National Institute of Standards and Technology*, (2010).

4 Commission, U. S. I. T. *Global Competitiveness of U. S. Environmental Technology Industries: Municipal and Industrial Water and Wastewater*. (1995).

5 McClements, D. J. Nanoemulsions versus microemulsions: terminology, differences, and similarities. *Soft Matter* 8, 1719-1729, (2012).

6 Ichikawa, T., Itoh, K., Yamamoto, S. & Sumita, M. Rapid demulsification of dense oil-in-water emulsion by low external electric field - I. Experimental evidence. *Colloid Surface A* 242, 21-26, (2004).

7 Belfer, S., Fainshtain, R., Purinson, Y., Gilron, J., Nystrom, M. & Manttari, M. Modification of NF membrane properties by in situ redox initiated graft polymerization with hydrophilic monomers. *J Membrane Sci* 239, 55-64, (2004).